# Selected problems of laser ablation theory

S I Anisimov, B S Luk'yanchuk

## Contents

**Abstract. Physical mechanisms and theoretical models of laser ablation are discussed. For various mechanisms, typical associated phenomena are qualitatively regarded and methods for studying them quantitatively are considered. Calculated results relevant to ablation kinetics for a number of substances are presented and compared with experimental data.**

## 1. Introduction

Several thousand journal publications are devoted to laser ablation, and it has been the topic of many international conferences (see, for instance, Refs [1 – 7]). In the physical literature the term 'ablation' (which has its origin in the Latin *ablatio* — taking away, removal) denotes the aggregate of complex physicochemical processes responsible for removing (carrying away) material from the surface or bulk of a solid. Following the meaning of the Latin root, any loss[1] may be

---

[1] Interestingly, the Russian thesaurus of the notion 'loss' comprises the words 'evaporate' and 'volatize', which bear a direct relation to ablation.

---

**S I Anisimov** L D Landau Institute for Theoretical Physics,
Russian Academy of Sciences,
Institutskiĭ prosp. 12, 142432 Chernogolovka, Moscow Region,
Russian Federation
Tel. (7-095) 702 93 17. Fax (7-095) 938 20 77
E-mail: anisimov@itp.ac.ru
**B S Luk'yanchuk** Research Center of Wave Studies,
General Physics Institute, Russian Academy of Sciences
ul. Vavilova 38, 117492 Moscow, Russian Federation
Tel. (7-095) 132 83 42. Fax (7-095) 135 82 34
E-mail: lukyanch@kapella.gpi.ru
Data Storage Institute at the National University of Singapore,
117608 Singapore

referred to as ablation. That is why the term 'laser ablation' is sometimes interpreted in the broad sense to denote any laser-induced material removal, including the removal of volatile products of chemical etching and even the electron emission (see editor's foreword to book [4]).

An excessively narrow interpretation of the term can also be encountered in the scientific literature, when the term 'ablation' is used in reference to the material removal caused by the direct chemical bond breaking under the action of light [8]. As a matter of fact, the term 'ablation' is interdisciplinary and has been used in physics for denoting the removal of material in an electric discharge, in the flow of a hot gas, plasma, etc. long before the advent of lasers. In geology this term is used to denote the reduction of the mass of a glacier or a blanket of snow due to melting and evaporation (see, for instance, Ref. [9]).

The overwhelming majority of researchers (see, for instance, Refs [3, 5, 6, 10]) utilize the term laser ablation in reference to the damage of a solid material, similar to evaporation or sublimation, which is usually complicated by the occurrence of a condensed phase in the disintegration products. An analysis of the extensive literature on laser ablation allows us to recognize three distinguishing (restrictive) features of this process: (i) ablation is directly related to the absorption of laser energy in the material; (ii) in principle, ablation can proceed in vacuum or an inert medium, and (iii) laser ablation results in the production of a vapor – gas (vapor – plasma) plume of ablation products. These characteristic features are discussed in detail, for example, in the monograph [10].

On the strength of the first restriction, the processes associated, for instance, with mechanical material failure under the action of a shock generated by a laser in the external medium, be it gas or liquid, do not fall into the category of laser ablation. This restriction also applies to the plasma etching of a material in the optical breakdown of the

ambient medium. The second limitation excludes laser-induced chemical etching [10].

Lastly, the third restriction does not allow the term laser ablation to be applied to the mechanical failure occurring in the direct absorption of energy in the disintegrating material if the disintegration products do not make up a plume (an example of such a process is the 'crumbling' of a material through the formation of microcracks [11]). Many authors also emphasize that laser ablation is of threshold character with respect to the fluence [2] $\Phi$, i.e. an appreciable removal of the material takes place only provided $\Phi > \Phi_{th}$ (see, for instance, Refs [10, 12–14]).

The pioneering investigations of laser ablation were performed more than 30 years ago [15] (see also the monographs [16, 17], the articles [183, 184] and references cited therein). Familiarizing oneself with the extensive scientific literature shows, however, that more recent investigations, including many of the latest papers, replicate (sometimes not without errors) the well-known results of the 1960s and 1970s. Moreover, papers significant for understanding the physics of the phenomenon often pass unnoticed against a background of the applied papers.

The aim of this review is to endeavor to systematically outline the basic results of investigations into the physics of laser ablation and to highlight, in particular, the advances made in recent years. Because of the breadth of the problem, the enormous number of publications and the diversity in their scientific level, we are forced to restrict the review to the consideration of two issues: the mechanisms of laser ablation (with regard to the restrictions in apprehension of the term) and the physical processes within the plume of ablation products. Both these issues are important to different practical applications. Our principal concern will be with the quantitative methods for investigating ablation, which make it possible to obtain results allowing a direct comparison with experiments.

## 2. Thermal model

### 2.1 Qualitative results

The first investigations of laser ablation [15–17] primarily concerned the response of absorbing media to the radiation of cw lasers and lasers with a millisecond output pulse operating in the free running mode, with quasi-stationary ablation regimes receiving the bulk of attention. Relying on the results of these investigations, the so-called thermal model of laser evaporation [15, 18, 19] was formulated in the 1960s, which has not undergone substantial changes. The papers on laser evaporation were reviewed on the basis of the thermal model in Refs [12, 20, 21].

The rapid progress in experimental techniques had the effect that even from the early 1980s ablation research was pursued primarily with laser pulses of the nanosecond range [10]. During the last decade, increasingly more attention has been paid to the ablation produced by ultrashort laser pulses of the picosecond and femtosecond ranges (see Refs [23–25]); the quasi-stationary mode is not attained for such pulses.

One of the first questions that an experimenter has to answer in the course of investigations is the question of the laser ablation mechanism [26]. In particular, it is vital to

understand whether experimental data can be interpreted in the context of the thermal model or other mechanisms (the photochemical bond breaking, nonequilibrium molecular excitation, etc.) play an important part in the process considered. To do this requires verification in some way if the laser ablation rate obeys conventional 'thermal' behavior.

The kinetics of thermal evaporation of condensed bodies is described by the relationship

$$v = v_0 \exp\left(-\frac{T_a}{T}\right). \tag{2.1}$$

The constants $v_0$ and $T_a$ in formula (2.1) are borrowed from reference data (see, for instance, handbook [27]), whose accuracy is not high. (The derivation and a comprehensive discussion of formula (2.1) may be found in Ref. [12].)

Under laser pulse irradiation, the temperature $T$ and the laser ablation rate $v$ vary with time. Should the dependences $T(t)$ and $v(t)$ be determined in experiments with a sufficiently high accuracy, the answer to the question of the laser ablation mechanism can be provided by analyzing these dependences in Arrhenius coordinates:

$$\ln v = f\left(\frac{1}{T}\right),$$

in which a straight line corresponds to the thermal process.

However, the difficulty is that direct measurements of $T(t)$ and $v(t)$ are extremely hard to accomplish in experiments with short laser pulses. As a rule, experimenters determine another dependence with a high enough accuracy, namely, the layer thickness $h$ of the material removed per pulse as a function of fluence $\Phi$ [10]:

$$h = h(\Phi), \qquad h = \int_0^\infty v(t)\,dt, \qquad \Phi = \int_0^\infty I(t)\,dt, \tag{2.2}$$

where $I(t)$ is the intensity of incident laser radiation. The integral curve $h = h(\Phi)$ depends only slightly on the change in the ablation mechanism. That is why the experimental data can be satisfactorily described employing conservation laws which take essentially no account of the kinetics of the process investigated.

The qualitative behavior of the $h = h(\Phi)$ dependences is easy to analyze. For materials strongly absorbing the laser radiation, these dependences contain, as a rule, three characteristic regions, which are specific of the subthreshold process ($\Phi < \Phi_{th}$), the ablation in the immediate vicinity of the threshold ($\Phi \sim \Phi_{th}$), and the mode of developed ablation ($2.5\Phi_{th} < \Phi < 5\Phi_{th}$).

In typical cases, the surface temperature $T$ peaks at some point in time $t_{max}$ (of the order of the pulse length $\tau_l$) and varies smoothly in the vicinity of the peak. One can therefore write out

$$T \approx T_{max} - \frac{1}{2}\,T''(t_{max})(t - t_{max})^2.$$

Furthermore, in the cases of practical interest one can recognize that $T_a \gg T$ in formula (2.1). [This inequality determines in fact the range of applicability for formula (2.1).] That is why the integral of the laser ablation rate, which appears in expression (2.2), can be calculated by the saddle-point method. As a result we obtain the layer thickness

---

[2] We take advantage of the term 'fluence' in lieu of the equivalent term 'irradiation dose' [J cm$^{-2}$] adopted in the Russian scientific literature.

of the material removed in one pulse:

$$h = A \exp\left(-\frac{T_a}{T_{max}}\right), \qquad A \approx \sqrt{2\pi}\, v_0 \tau_l \left(\frac{T_{max}}{T_a}\right)^{1/2}. \quad (2.3)$$

In the range of temperatures typical of laser ablation, the weak temperature dependence of the parameter $A$ can be neglected.

In the majority of experiments on laser ablation, the fluence $\Phi = I_0 \tau_l$ is varied through the variation of the intensity (neutral density filters, focusing), while the pulse is fixed. In this case, for subthreshold fluences ($\Phi < \Phi_{th}$) we can assume with a good accuracy that $T_{max} \propto \Phi$ and transform relationship (2.3) to the Arrhenius form

$$h = A \exp\left(-\frac{B}{\Phi}\right), \qquad (2.4)$$

where $A$ and $B$ are the constants. The presence of 'Arrhenius tails' is quite often regarded as a forcible argument in favor of the thermal mechanism of laser ablation (see, for instance, Ref. [28]), despite the fact that such tails may occur in other models, too [29].

Above the threshold of laser ablation ($\Phi > \Phi_{th}$), for relatively short laser pulses and high radiation absorption coefficients there occurs an intermediate linear dependence of the evaporated layer thickness on the fluence, which follows from the energy balance [10]:

$$h = \beta(\Phi - \Phi_{th}), \qquad \beta \approx \frac{1-R}{L}, \qquad (2.5)$$

where $R$ is the radiation reflection coefficient, and $L$ is the latent heat of vaporization per unit volume of a solid.

Lastly, the screening of the evaporable surface by the plume of ablation products exerts a significant influence on the ablation process for high laser fluences ($2.5\Phi_{th} < \Phi < 5\Phi_{th}$). Assuming the optical thickness of the screening plume to be proportional to the mass evaporated, it is easy to show that the fluence that finds its way to the solid surface, taking into account the radiation absorption in the plume, is given by

$$\Phi_a = \Phi \exp\left(-\alpha_g h\right),$$

where $\alpha_g$ is the effective radiation absorption coefficient of the vapor normalized to the density of the solid [3]. We substitute $\Phi_a$ for $\Phi$ in formula (2.4) and solve the resultant equation for $\Phi$ to obtain

$$\Phi = B \exp\left(\alpha_g h\right) \ln^{-1} \frac{A}{h}. \qquad (2.6)$$

Equation (2.6) was proposed in Ref. [29] as an interpolation formula for describing the dependence of the ablated thickness on the laser fluence over a wide range of variation of the latter quantity. One can see from Fig. 1 that this equation agrees well with available experimental data. For small fluences, Eqn (2.6) passes into Eqn (2.4). For high fluences, when the screening plays a significant role, it leads to a logarithmic dependence

$$h = \frac{1}{\alpha_g} \ln \frac{\Phi}{\Phi_g}, \qquad \Phi_g = \frac{B}{\ln\left(\alpha_g A\right)}. \qquad (2.7)$$

[3] Other screening models were considered in Refs [183, 16].

Although all three characteristic dependences — the Arrhenius dependence (2.4) in the subthreshold range, the linear one (2.5) in the vicinity of the threshold, and the logarithmic one (2.7) in the screening region — were derived in the foregoing from qualitative considerations, these dependences also follow from an extended consideration of the dynamics of the process in the framework of the thermal model [30]. These three ranges are conveniently analyzed more closely by going over to the corresponding coordinates in which the $h(\Phi)$ dependences are represented by straight lines (Figs 1d–f).

The weak dependence of the integral curves on the detailed kinetics of laser ablation has the effect that the plots $h = h(\Phi)$ depicted in hundreds of papers prove to bear little information when it comes to determining the physical mechanism responsible for the ablation of one or other specific material. Reaching a conclusion of this kind always requires additional information, which may be extracted, for instance, from the data on the composition and expansion velocities of laser ablation products. In this case, the evidence on the time variation of the surface temperature of the material experiencing ablation would be most informative. These data, however, are hard to obtain. Paper [31] is likely an exceptional example where the surface temperature of polyimide was measured with its ablation produced by the nanosecond pulse of an excimer laser.

## 2.2 Dynamics of laser ablation. Calculations assisted by the moments method

Since the temperature of laser ablation is hard to measure with a high accuracy, the task of its exact calculation takes on great significance. This problem is rather complicated. Calculations based on the solution of the linear heat conduction equation are oversimplified and sometimes inappropriate even for qualitative estimates. By contrast, numerical calculations involving the difference methods for partial differential equations are too cumbersome and unsuitable for a rapid analysis of the experimental data. The moments method proves to be best suited to quantitative calculations of laser ablation temperature. This method permits the complex nonlinear problem of solving partial differential equations to be reduced to the integration of a system of ordinary differential equations. With this method it is easy to take into account the temperature dependences of optical and thermal properties of the material, the effects caused by radiation absorption in the vapor, the phase transitions (evaporation, melting, structural transitions), and also the arbitrary laser pulse shape [30, 32, 33].

Let us consider the transient laser ablation in the one-dimensional case. This case is realized when a target is irradiated by a sufficiently short laser pulse. Let the plane ablation front travel in the $z$-direction with a velocity $v = v(t)$ which changes rapidly during the laser irradiation.

The heat conduction equation is conveniently written in the ablation-front frame of reference:

$$\frac{\partial H}{\partial t} = v \frac{\partial H}{\partial z} + \frac{\partial}{\partial z}\left(\varkappa \frac{\partial T}{\partial z}\right) - \frac{\partial I}{\partial z} \equiv B[T], \qquad (2.8)$$

where

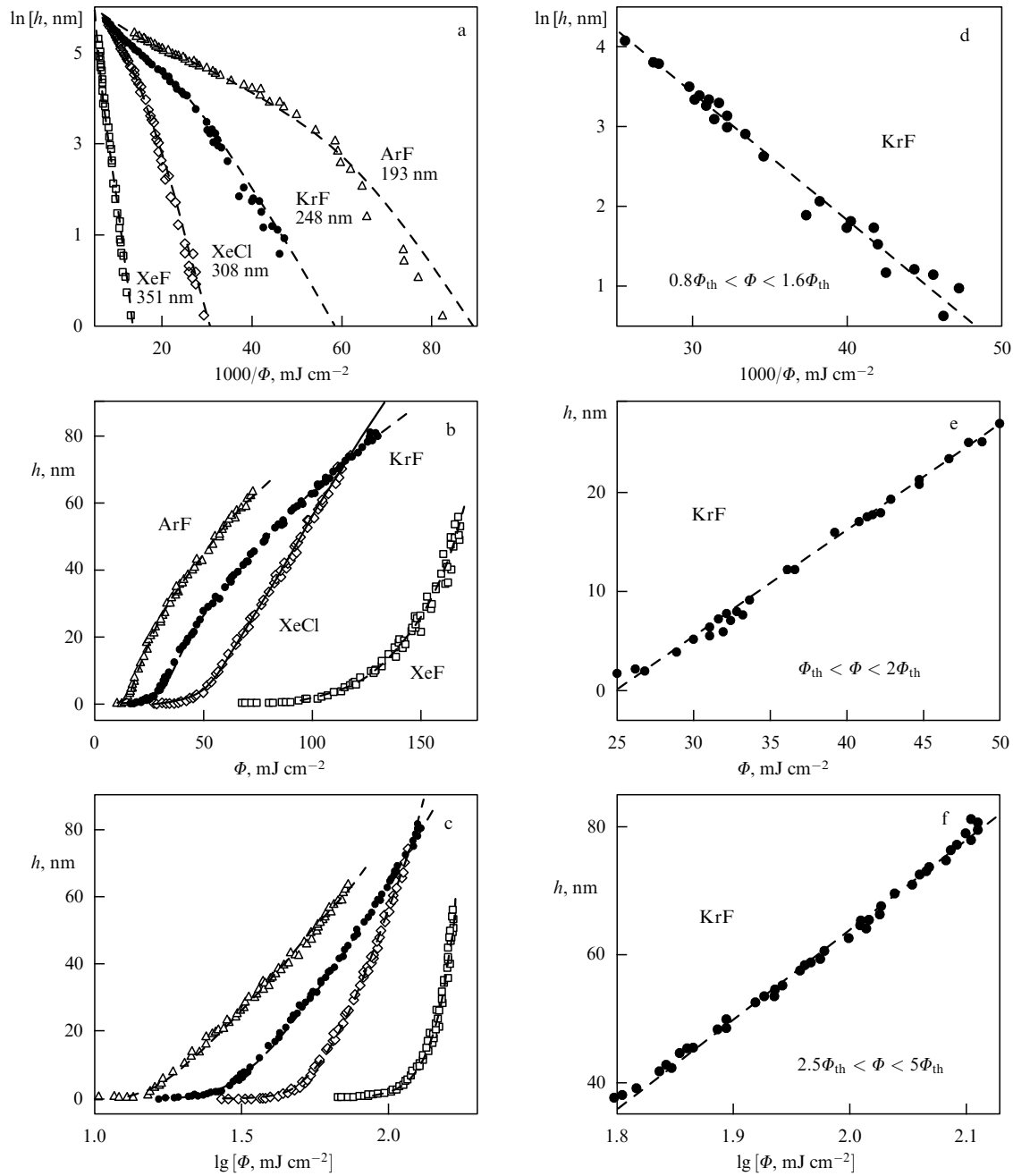$$H(T) = \rho \int_{T_\infty}^{T} c(T_1)\, \mathrm{d}T_1 \qquad (2.9)$$

**Figure 1.** Thickness of the material (polyimide) ablated under excimer ArF-, KrF-, XeCl-, and XeF-laser irradiation, reproduced from the data of Ref. [26], in Arrhenius (a), linear (b), and logarithmic (c) coordinates. The dashed lines represent the best approximation by interpolation formula (2.6). The parameters of calculations for wavelengths of 193, 248, 308, and 351 nm, obtained by least-square fit, are as follows: $A = 883\,547$, $29\,716$, $87\,097$, and $32\,562$; $B = 152.56$, $176.13$, $370.03$, and $760.92$ mJ cm$^{-2}$; $\alpha_g = 2 \times 10^5$, $1.22 \times 10^5$, $5.5 \times 10^4$, and $-1.9 \times 10^4$ cm$^{-1}$. (d–f) Enlarged view of the regions wherein experimental points follow the Arrhenius (2.4), linear (2.5), and logarithmic (2.7) dependences (straight dashed lines).

is the enthalpy of a unit volume of the solid, $c(T)$ is the specific heat capacity of the solid, $\varkappa(T)$ is the thermal conduction coefficient, and $T_\infty$ is the initial temperature. The density $\rho$ of the solid is assumed to be constant, and $B[T]$ denotes the right-hand side of Eqn (2.8).

The absorbed laser radiation intensity distribution in the bulk of a solid is defined by the equation

$$\frac{\partial I}{\partial z} = -\alpha I, \qquad I\Big|_{z=0} = I_s. \tag{2.10}$$

Here, $\alpha$ is the absorption coefficient, and $I_s$ is the absorbed laser radiation intensity at the ablation front ($z = 0$).

The intensity $I_s$ at the ablation front depends on the temporal form of the laser pulse $I = I(t)$, the surface temperature $T_s = T(z = 0, t)$, and the layer thickness of an evaporated material:

$$h(t) = \int_0^t v(t_1)\,\mathrm{d}t_1\,,$$

which screens the ablation front:

$$I_s = I(t)\,A(T_s)\exp\left(-\alpha_g h\right), \tag{2.11}$$

where $A(T_s) = 1 - R(T_s)$ is the absorptivity, $R$ is the reflectivity, and $\alpha_g$ is the absorption coefficient of the vapor

(ablation products) normalized to the solid density. The velocity of the ablation front is defined by formula (2.1) in which $T = T_s(t)$ should be substituted.

All optical and thermal parameters in equations (2.8)–(2.11) and also the preexponential factor in formula (2.1) may arbitrarily depend on the temperature.

The heat conduction equation (2.8) should be complemented with initial and boundary conditions. The boundary condition at the ablation front relates the heat flux $J_s$ at the phase interface to the expenditure of energy for evaporation [16]:

$$\varkappa \frac{\partial T}{\partial z}\bigg|_{z=0} = v(L - H_s + H_s^{(v)}) \equiv -J_s. \qquad (2.12)$$

Here, $L$ is the latent heat of evaporation per unit volume of the solid, $H_s = H(T_s)$ is the enthalpy of a unit volume of the solid at the phase interface, and also

$$H_s^{(v)} = \rho \int_{T_\infty}^{T_s} c^{(v)}(T_1)\,\mathrm{d}T_1$$

is the vapor formation enthalpy referred to a unit volume of the solid, and $c^{(v)}(T)$ is the heat capacity of the vapor at constant pressure. The second boundary condition $T|_{z\to\infty} = T_\infty$ and the initial condition $T|_{t=0} = T_\infty$ are obvious.

In view of the relationship (2.9) among $T$ and $H$, the boundary condition (2.12) can be rewritten as

$$\frac{\partial H}{\partial z}\bigg|_{z=0} = -\frac{J_s}{\chi_s}, \qquad (2.13)$$

where $\chi = \varkappa/c\rho$ is the thermal diffusivity, and $\chi_s = \chi(T_s)$. The model described by Eqns (2.8)–(2.13) does not take into account some effects, for instance, the density variation $\rho = \rho(T)$ caused by the thermal expansion of the solid. However, the discarded effects are, as a rule, small, and therefore the model outlined in the foregoing is appropriate for the *quantitative* investigation of transient ablation.

The basic idea of the moments method was outlined in detail in the monographs [34–36]. The exact solution of the boundary-value problem (2.8)–(2.13) turns Eqn (2.8) into an identity. If some trial function $H = H_p(z, t)$ is substituted in lieu of the exact solution, the identity is violated with the consequential formation of a residual function Res $[H_p]$:

$$\frac{\partial H_p}{\partial t} - B[T_p] \equiv \text{Res}\,[H_p]. \qquad (2.14)$$

The trial function $H_p(z, t)$ may be employed as an approximate solution if it is selected in such a way that the integral relations (conservation laws) for momenta $M_n$ are exactly fulfilled:

$$\frac{\mathrm{d}M_n}{\mathrm{d}t} - \int_0^\infty z^n B\left[T(H_p(z, t))\right]\mathrm{d}z = 0, \qquad (2.15)$$

$$M_n = \int_0^\infty z^n H_p(z, t)\,\mathrm{d}z.$$

The total number of Eqns (2.15) should be equal to the number of unknown functions employed to construct the trial function $H_p(z, t)$. Equations (2.15) minimize the residual function Res $[H_p]$ along the $z^n$-directions in the functional space. The moments method has much in common with the well-known Galerkin method. Both of them are the special cases of the weighted residues method. An important point is that the moments method ensures the fulfillment of some integral relations which have a clear physical meaning and constitute the system of conservation laws. For instance, Eqn (2.15) for the $M_0$ moment is the total energy conservation law, and the equation for the $M_1$ moment characterizes the local energy balance.

In papers [30, 32, 33], advantage was taken of the system of equations for the first two moments of the enthalpy distribution. The surface temperature $T_s(t)$ (or the related enthalpy $H_s \equiv H[T_s(t)]$ of the solid at the boundary $z = 0$) and the spatial scale $l(t)$ of the enthalpy distribution were selected as two time-dependent functions. These two quantities yield the main body of information on the enthalpy distribution in the surface layer of the solid, which in turn governs the dynamics of thermal ablation.

In accordance with relations (2.15) we introduce two moments of the enthalpy distribution:

$$M_0(t) = \int_0^\infty H(z, t)\,\mathrm{d}z, \qquad M_1(t) = \int_0^\infty z\,H(z, t)\,\mathrm{d}z. \qquad (2.16)$$

We multiply relations (2.8) by $z^n$ (where $n = 0, 1$) and integrate them term by term taking into account boundary conditions to obtain the following system of equations:

$$\frac{\mathrm{d}M_0}{\mathrm{d}t} = -vH_s + J_s + I_s = -v(L + H_s^{(v)}) + I_s,$$
$$\frac{\mathrm{d}M_1}{\mathrm{d}t} = -vM_0 + \int_{T_\infty}^{T_s} \varkappa(T)\,\mathrm{d}T + \alpha^{-1}I_s. \qquad (2.17)$$

It should be emphasized that on the right-hand side of the second of Eqns (2.17) there is an integral typical for the Kirchhoff transformation [37].

The proper choice of the trial function is of crucial importance in the moments method. In works [30, 32, 33], this function was adopted as

$$H_p(z, t) = \frac{1}{1 - \alpha l}\left[\left(H_s - \frac{J_s l}{\chi_s}\right)\exp(-\alpha z)\right.$$
$$\left. - \left(\alpha l H_s - \frac{J_s l}{\chi_s}\right)\exp\left(-\frac{z}{l}\right)\right]. \qquad (2.18)$$

A trial function of the form (2.18) satisfies the boundary conditions for $z = 0$, $z = \infty$ and ensures the fulfillment of the obvious condition $H_p(z = 0, t) \equiv H_s(t)$. The first term in expression (2.18) describes the variation of the enthalpy distribution related to the radiation penetration depth, while the second term describes the effects related to thermal conduction. The function $l(t)$ is the enthalpy distribution spatial scale (the heated layer thickness or the characteristic thermal length).

Substituting expression (2.18) into Eqn (2.16) we arrive at the following expressions for the moments:

$$M_0 = (l + \alpha^{-1})H_s - \alpha^{-1}l\frac{J_s}{\chi_s},$$
$$M_1 = (l^2 + \alpha^{-1}l + \alpha^{-2})H_s - (l + \alpha^{-1})\alpha^{-1}l\frac{J_s}{\chi_s}. \qquad (2.19)$$

Let us introduce expressions (2.19) into Eqns (2.17) to obtain the differential equations for the functions $T_s(t)$ and $l(t)$. Recall that the $J_s$ and $H_s$ quantities are related to $T_s$ by equations (2.9) and (2.12). It is worth noting that we need not solve these equations for the derivatives $\mathrm{d}l/\mathrm{d}t$ and $\mathrm{d}T_s/\mathrm{d}t$ and write them out explicitly when advantage is taken of a high-level software, for instance, of the 'Mathematica' package [38], to numerically solve the resultant equations.

The system of equations for the surface temperature and the heated layer thickness should be complemented with the equation describing the variation of the ablation layer thickness:

$$\frac{\mathrm{d}h}{\mathrm{d}t} = v = v_0 \exp\left(-\frac{T_a}{T_s}\right), \qquad (2.20)$$

which is required for describing the screening effect.

Therefore, the problem reduces to a system of three ordinary differential equations for the functions $T_s(t)$, $l(t)$, and $h(t)$, which should be numerically integrated with the corresponding initial conditions. This approach proves to be more flexible and convenient for the analysis of experimental data than the direct numerical solution of the boundary-value problem employing finite difference or finite element methods. An investigation of different problems on laser ablation, performed in Refs [30, 32, 33], reveals that the moments method maintains an accuracy of about $20-30\,\%$ and allows easy inclusion of the temperature variations of $c(T)$, $\varkappa(T)$, and $A(T)$.

Figure 2 gives an example of the computational investigation into the ablation kinetics of polyimide exposed to the radiation of excimer lasers with different wavelengths. The temperature dependences of the thermal parameters of the material were taken into account in the computations. The laser pulse shape was modeled by the function

$$I(t) = I_0 \frac{t}{t_1} \exp\left(-\frac{t}{t_1}\right) \qquad (2.21)$$

with the fluence and the characteristic time related by the formula $\Phi = I_0 t_1$. We note that the FWHM (full width at half maximum) of the laser pulse is $t_{\mathrm{FWHM}} \approx 2.445 t_1$. For brevity the pulse of the form (2.21) will be referred to as the 'excimer' pulse.

One can see from Fig. 2 that the dependences of the removed layer thickness $h$ on the fluence $\Phi$ for the 350-, 308-, and 248-nm wavelengths are adequately described in the context of the thermal model with surface evaporation. Notice that the temperature at the ablation front, found from the calculations [30], agrees well with that measured in Ref. [31]. For the 193-nm radiation, computations and experimental data diverge significantly. It would appear reasonable that the ablation mechanism does not reduce to the purely thermal one in this case.

Similar calculations employing the moments method were done for the laser ablation of metals. In Ref. [32], for instance, a study was made of the ablation of indium exposed to a laser pulse with a duration $t_{\mathrm{FWHM}} = 15$ ns. It turned out that the calculated results involving the thermal model agree nicely with experimental data over the nanosecond range [22, 39]. At the same time, the ablation mechanism proves to be more complicated for subpicosecond pulses ($t_{\mathrm{FWHM}} = 0.5$ ps). Some of the calculated results
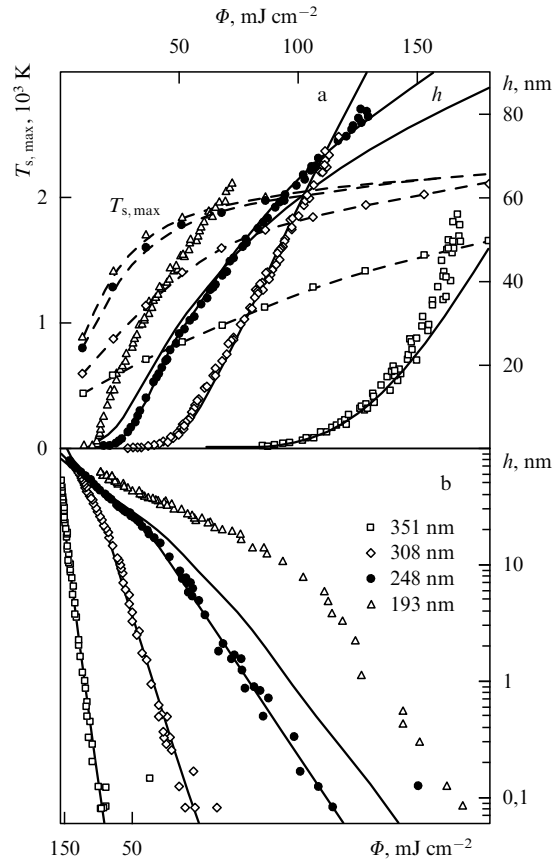


**Figure 2.** Laser ablation of polyimide [29]. Calculation by the moments method (solid curves) and from experimental data [26] in conventional (a) and Arrhenius (b) coordinates. Parameters of calculations: $t_1 = 6.13$ ns (the FWHM of the laser pulse is 15 ns); $v_0 = 3 \times 10^6$ cm s$^{-1}$; $T_a = 15.7 \times 10^3$ K $= 1.51$ eV; $T_\infty = 300$ K; $c = 2.55 - 1.59 \exp\left[(300 - T)/460\right]$ J g$^{-1}$ K$^{-1}$; $\varkappa = 1.55 \times 10^{-3} \times (T/300)^{0.28}$ W cm$^{-1}$ K$^{-1}$; $\rho = 1.42$ g cm$^{-3}$; $L/\rho = 500$ J g$^{-1}$; $\alpha_g = 0.45\alpha$; $\lambda = 193$ nm (triangles), $A = 0.93$, $\alpha = 4.25 \times 10^5$ cm$^{-1}$; $\lambda = 248$ nm (circles), $A = 0.88$, $\alpha = 3.1 \times 10^5$ cm$^{-1}$; $\lambda = 308$ nm (diamonds), $A = 0.89$, $\alpha = 10^5$ cm$^{-1}$, and $\lambda = 351$ nm (squares), $A = 0.9$, $\alpha = 0.32 \times 10^5$ cm$^{-1}$. The dashed lines represent the calculated peak surface temperature.

on the laser heating dynamics and indium ablation are given in Fig. 3.

## 2.3 Stationary evaporation wave

We will enlarge on some qualitative features of the thermal mechanism of surface evaporation. These features may be explained by the simplest example of a model with constant thermal and optical characteristics. Simplifying the problem, in the boundary condition (2.12) we neglect the effects related to the discrepancy between the gas phase and condensed phase enthalpies. The vapor will be considered transparent for the radiation, i.e. let $\alpha_g = 0$. Furthermore, we assume the absorbed radiation intensity to be constant: $I_s = \mathrm{const}$ (a rather long laser pulse).

Under the above-listed simplifications, the problem reduces to the system of two ordinary differential equations for the surface temperature $T_s$ and the heated layer thickness $l$. This system can be written out in the explicit form

$$\frac{\mathrm{d}T_s}{\mathrm{d}t} = F(T_s, l), \qquad \frac{\mathrm{d}l}{\mathrm{d}t} = \Psi(T_s, l). \qquad (2.22)$$
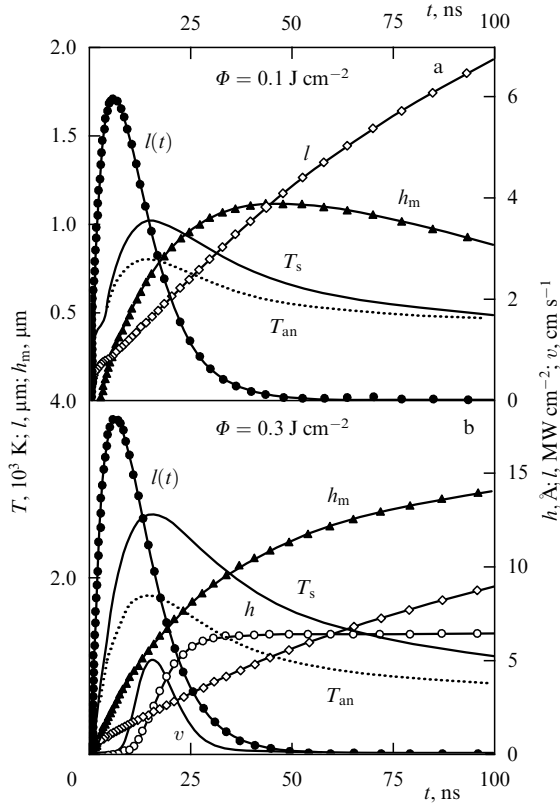
**Figure 3.** Calculated results on the laser heating and ablation of an indium target in the subthreshold mode (the FWHM of the laser pulse is 15 ns) [30]. Shown are the laser pulse profile $I(t)$, the surface temperature $T_s$, the heated layer thickness $l$, the location of the melting front $h_m$, the ablation rate $v$, and the ablation layer thickness $h$ of the material. The dotted line represents the temperature determined through the solution of the linear heat conduction equation

$$T_{an}(t) = T_\infty + \frac{\alpha A}{\rho c} \int_0^t I(t-t_1) \exp\left[\alpha^2 D t_1\right] \mathrm{erfc}\, \sqrt{\alpha^2 D t_1}\ \mathrm{d}t_1\,.$$

The thermal parameters in the equation are constant and equal to the corresponding values at room temperature $T_\infty$. The temperature dependences of the parameters $c$, $\varkappa$, $\alpha$, and $A$ employed in the calculations were reported in Ref. [30].

The functions $F$ and $\Psi$ in the above equations are defined by the formulas

$$F = \alpha v T_L \left[ (2q+1)\frac{1}{\xi} - \left(1 + \frac{\xi}{\alpha l}\right)\theta_s - 2 \right] \left[ 2 + \alpha l + \Pi \right]^{-1},$$

$$\Psi = \frac{\chi}{l} + \left\{ \alpha l \left[ q - \theta_s(1-\xi) + (1+\alpha l + \Pi)\left(1 - q - \frac{1}{\xi}\right) \right] \right.$$

$$\left. + (1+\theta_s\xi)(1+\Pi) \right\} \left[ (1+\theta_s\xi)(2+\alpha l + \Pi) \right]^{-1}, \quad (2.23)$$

where

$$T_L = \frac{L}{c}, \qquad \Pi = \frac{T_a T_L}{(T_s + T_\infty)^2}\frac{vl}{\chi},$$

$$\theta_s = \frac{T_s}{T_L}, \qquad \xi = \frac{\alpha\chi}{v}, \qquad q = \frac{I_s}{c\rho v T_s}$$

$$(2.24)$$

are dimensionless parameters. To avoid misunderstanding, we note that in Eqns (2.22)–(2.24) and from then on $T_s$

denotes the increase in temperature, i.e. the surface temperature is now defined as $T_s + T_\infty$.

The investigation of the system of equations (2.22) is a conventional problem of the nonlinear theory of oscillations [40]. This system of equations has a single singular point ($T_s = T_{s0}$, $l = l_s$) which corresponds to the so-called stationary evaporation wave [15, 16, 18], where $F = \Psi = 0$. The parameters of the stationary wave are conveniently written in the implicit form

$$v_s = v_0 \exp\left(-\frac{T_a}{T_{s0} + T_\infty}\right), \quad I_s = c\rho v_s(T_{s0} + T_L), \quad l_s = \frac{\chi}{v_s}\,.$$

$$(2.25)$$

Notice that the temperature $T_{s0}$ and the heated layer thickness $l_s$ are independent of the absorption coefficient $\alpha$.

The temperature distribution in the stationary evaporation wave is of the form

$$T(z) = T_{s0} \exp\left(-\alpha z\right)$$

$$+ \frac{\alpha l_s T_{s0} + T_L}{1 - \alpha l_s}\left[\exp\left(-\alpha z\right) - \exp\left(-\frac{z}{l_s}\right)\right]. \quad (2.26)$$

It is well known [16] that the temperature distribution (2.26) has a peak located at a distance

$$z_{max} = \frac{l_s}{1-\alpha l_s} \ln \frac{\alpha l_s T_{s0} + T_L}{\alpha l_s (T_{s0} + T_L)} \quad (2.27)$$

beneath the surface. The peak temperature is given by the formula

$$T_{max} = (T_{s0} + T_L)\left(\frac{\alpha l_s T_{s0} + T_L}{\alpha l_s (T_{s0} + T_L)}\right)^{\alpha l_s/(\alpha l_s - 1)}. \quad (2.28)$$

Some of the parameters of the stationary evaporation wave are shown in Fig. 4. One can see from the plots that the lengths $l$ and $z_{max}$ decrease while the temperatures $T_{s0}$, $T_{max}$ and the subsurface superheating $\Delta T = T_{max} - T_{s0}$ grow with increasing radiation intensity. The lengths $l$ and $z_{max}$ differ greatly in scale (the point $z_{max}$ is located near the evaporable surface), and these lengths are therefore plotted on different scales in Fig. 4c. It must be remembered that the surface evaporation model is applicable only in the temperature range $T < T_c$, where $T_c$ is the critical temperature. As the critical temperature is approached, the enthalpy of the phase transition decreases and then vanishes at the critical point. To investigate the laser ablation at temperatures close to the critical one (and higher), advantage should be taken of gas dynamics equations.

The moments method and the fortunate choice of the trial function (2.18) lead to results which coincide with the exact solution not only for short, but for long ($t \to \infty$) times as well. Therein presumably lies the cause of the good accuracy of the method: 20–30% [30, 32, 33].

### 2.4 Oscillations, jumps, and other qualitative effects
We now turn to the dynamics of temperature variation. The stability investigation of the singular point (2.25) is performed by conventional techniques [40]. Calculating the derivatives

$$F_T = \frac{\partial F}{\partial T}, \qquad F_l = \frac{\partial F}{\partial l}, \qquad \Psi_T = \frac{\partial \Psi}{\partial T}, \qquad \Psi_l = \frac{\partial \Psi}{\partial l}$$
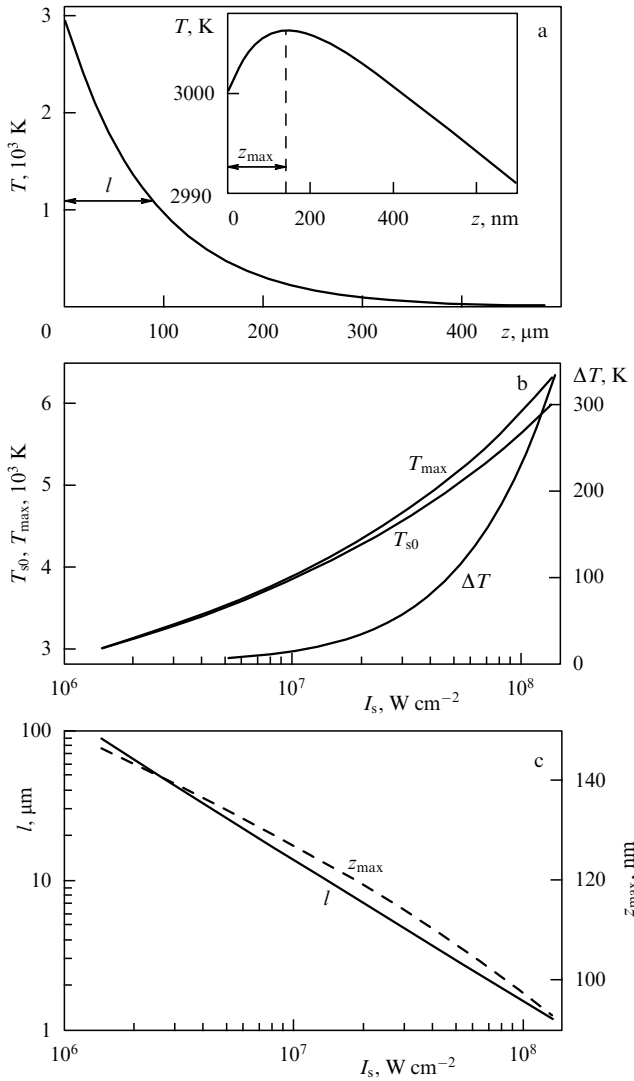
**Figure 4.** Parameters of the stationary evaporation wave calculated for $v_0 = 10^6$ cm s$^{-1}$, $T_a = 3 \times 10^4$ K, $T_\infty = 300$ K, $c = 1$ J g$^{-1}$ K$^{-1}$, $\varkappa = 1$ W cm$^{-1}$ K$^{-1}$, $\rho = 1$ g cm$^{-3}$, $L/\rho = 10^4$ J g$^{-1}$, and $\alpha = 10^5$ cm$^{-1}$: (a) temperature distribution in the wave for $T_{s0} = 3000$ K (the inset shows an enlarged view of the temperature peak neighborhood); (b) surface temperature $T_{s0}$, peak temperature $T_{max}$, and the superheating $\Delta T = T_{max} - T_{s0}$ as the functions of intensity $I_s$; (c) characteristic thermal length $l$ and location of the temperature peak $z_{max}$ as the functions of intensity $I_s$.

at a point $(T_s = T_{s0}, l = l_s)$, it is easy to verify that

$$p = F_T \Psi_l - F_l \Psi_T = \frac{\alpha v^3}{\chi} \left[ 1 + \frac{T_a (T_{s0} + T_L)}{(T_{s0} + T_\infty)^2} \right]$$

$$\times \left[ 2 + \xi + \frac{T_a T_L}{(T_{s0} + T_\infty)^2} \right]^{-1} > 0 ,$$

$$\sigma = -F_T - \Psi_l = \frac{v^2}{\chi} \left[ 1 + \xi \left( 3 + \frac{T_a (T_{s0} + 2T_L)}{(T_{s0} + T_\infty)^2} \right) \right]$$

$$\times \left[ 2 + \xi + \frac{T_a T_L}{(T_{s0} + T_\infty)^2} \right]^{-1} > 0 .$$

(2.29)

As relations (2.29) indicate, the singular point (a node or a focus) is stable, and *the stationary evaporation wave is therefore an attractor to which the solution is attracted from*

*any initial conditions*. The bifurcation boundary which separates the nodes and the foci is defined by the condition $\sigma^2 = 4p$. This boundary is shown in Fig. 5a in the $(\alpha, I_s)$-parameter plane. In the case when the state is a focus, the transient oscillations occur in the initial stage of the process. The phase portrait and the oscillation dynamics of the ablation rate and heated layer thickness for this system are shown in Figs 5b–d, respectively. These oscillations may be of importance for several practical problems [12].

When pulsed laser ablation is under investigation, the intensity of incident radiation depends on time [an example of such a dependence is relation (2.21)]. In this case, Eqns (2.22) should be solved simultaneously with Eqn (2.20) and the intensity $I_s$ at the ablation front is given by formula (2.11). The layer thickness of the material removed during a laser pulse is defined by the integral

$$h = v_0 \int_0^{t \gg t_l} \exp\left( -\frac{T_a}{T_\infty + T_s(t)} \right) dt .$$

(2.30)

The quantity (2.30) is an *intermediate asymptotics*. Should the integration in expression (2.30) be extended to infinity, the integral diverges. This is so because when $t \to \infty$ the temperature $T_s \to 0$, and the ablation rate $v = v_0 \exp(-T_a/T_\infty) > 0$ is a finite, even if very small, quantity. Intermediate asymptotics are widely used in the problems facing the physics of combustion and chemical kinetics [41–43].

Calculations carried out with the employment of the above technique confirm the qualitative analysis of the $h(\Phi)$ dependence performed in Section 2.3. It is easy to verify that the dependence $h(\Phi)$ shows three characteristic ranges in the case when the optical and thermal parameters are constant, namely, the subthreshold (for $\Phi < \Phi_{th}$), near-threshold ($\Phi > \Phi_{th}$, $\Phi \approx \Phi_{th}$), and screening ($2.5\Phi_{th} < \Phi < 5\Phi_{th}$) ranges. The asymptotic behavior of the $h(\Phi)$ curves in these ranges is adequately described by formulas (2.4), (2.5), and (2.7), and the general run of the dependence follows the interpolation formula (2.6), which may be considered typical for the thermal mechanism of laser ablation.

The lowering of the threshold $\Phi_{th}$ on shortening the laser pulse can also be considered as a characteristic feature of thermal ablation (Fig. 6a). The ablation threshold may also vary significantly with the form of the laser pulse [32]. The peak surface temperature grows with shortening the laser pulse, while the point in time at which this temperature is attained and the heated layer thickness $l$ at that very moment decrease (Fig. 6b).

Some special cases when the integral kinetics of laser ablation departs from the typical are noteworthy. These departures may be caused by the temperature dependences of the optical and thermal parameters of the material. We shall highlight here the departures of two types: (i) the slope of the $h(\Phi)$ dependence becomes more flatten, and (ii) the $h(\Phi)$ dependence steepens ('jumps' appear). Responsible for the special features of the first type is, for instance, the lowering of the heating rate in the vicinity of the melting point [32] and also the growth of the heat capacity with temperature [33]. The jumps in ablation rate may arise, in particular, due to the temperature dependence of the absorptivity $A(T)$.

As an example we refer to Fig. 7a which shows the $h(\Phi)$ curves obtained for a jump-like variation of absorptivity. The
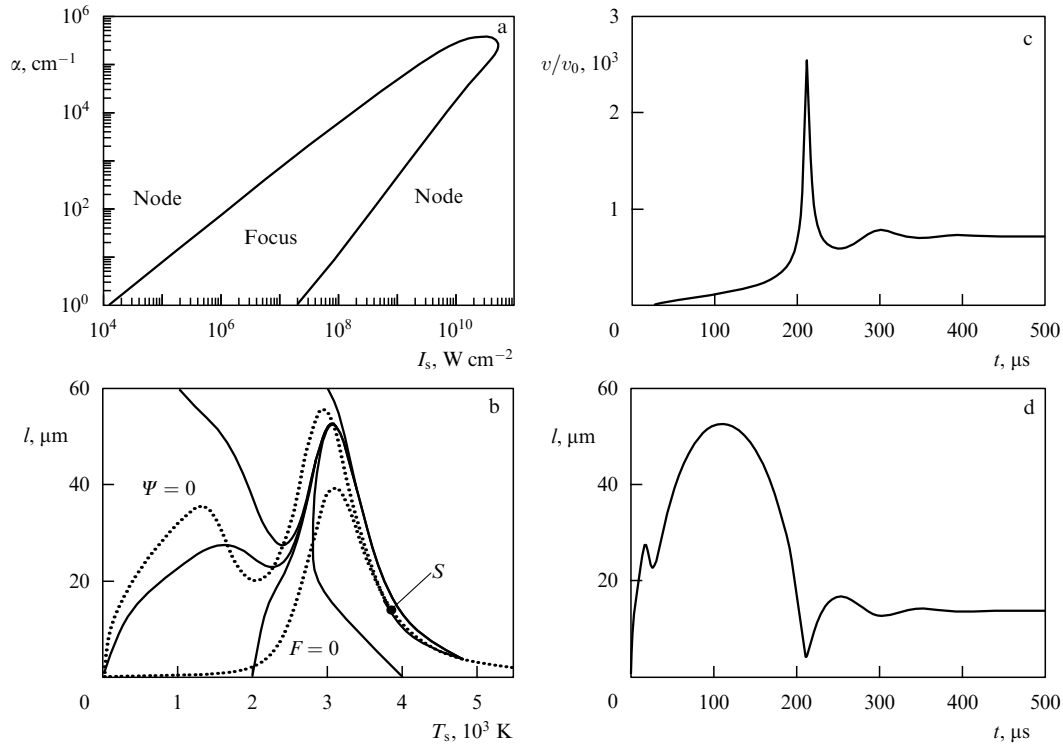
**Figure 5.** (a) Bifurcation boundary in the plane of parameters $(\alpha, I_s)$, which separates stationary states of the node and focus type; the thermal parameters are the same as in Fig. 4. (b) Phase portrait of the system for $\alpha = 10$ cm$^{-1}$, $I_s = 10^7$ W cm$^{-2}$, and stationary wave parameters $T_{s0} = 3848$ K, $l_s = 13.8$ μm. (c) Temporal variation of the laser ablation rate. (d) Temporal variation of the heated layer thickness $l$.

smoothed jump was modeled by the function

$$A(T) = A_1 + (A_2 - A_1)\left(\frac{1}{2} + \frac{1}{\pi}\arctan\frac{T - T_j}{\Delta T}\right). \quad (2.31)$$

The absorptivity varied from a value $A_1$ (for $T < T_j$) to a value $A_2$ (for $T > T_j$); the temperature interval in which the transition occurred had a width $\Delta T$.

An interesting feature of laser ablation in the case under consideration is the occurrence of an 'intermediate threshold' on reaching which the laser ablation rate experiences a rapid change. When the switching temperature $T_j$ is relatively low, the jumps in absorption have a minor effect on the shape of $h(\Phi)$ curves. But as $T_j$ increases, the changes in ablation rate become almost jump-like (Fig. 7b). Jumps of this type are frequently observed in experiments (see, for instance, Ref. [10]), but have not yet received a satisfactory explanation. In paper [13], attention was drawn to the fact that the intermediate jumps can be attributed to ablation upon cessation of the laser pulse, provided the ablation front catches up with the temperature peak in the layer beneath the surface. In real experiments, ablation is observed, as a rule, in the transient regime, which smears, as shown in Refs [30, 33], the jumps in the $h(\Phi)$ curves.

The moments method allows an easy analysis of the effect of temperature variations in the absorption coefficient $\alpha_g(T_s)$ on the ablation kinetics. The temperature of the plume is actually determined by its expansion dynamics and is different from the temperature at the ablation front. Nevertheless, the $\alpha_g(T_s)$ dependence can model the effect of screening on the ablation kinetics for several special cases of the plume expansion. The pattern of this influence is evident enough. If the absorption coefficient $\alpha_g(T_s)$ lowers with

temperature, the vapor at the laser pulse tail becomes more transparent, resulting in self-adjustment of the heating.

The calculated results which serve to illustrate the heating self-adjustment effect are presented in Figs 7b and 7c where the $\alpha_g(T_s)$ dependence was modeled by a jump function of the same form as that given by expression (2.31). With reference to these figures it is seen that the bleaching of vapor due to its cooling does not result in qualitative changes in the form of the $h(\Phi)$ curve, but it is amply manifested in the dynamics of temperature variation at the ablation front. The heating self-adjustment is responsible for the effect of 'thermal memory', when the surface temperature close to the switching temperature $T_j$ is retained for a long time during the passage of a laser pulse tail (Fig. 7c). If $\alpha_g = $ const, the temperature decreases monotonically over a length of the laser pulse tail (see, for instance, Fig. 3b).

Among the qualitative features of laser ablation, which are caused by the thermal dependences of optical and thermal parameters of a material, mention should be made of the possibility that a self-oscillation mode becomes settled in the laser evaporation of transparent dielectric materials [12, 14]. For these materials, the electron component $\varkappa_e$ of the thermal conduction coefficient and the static electrical conduction $\sigma_0$ which determines the absorption coefficient $\alpha(T)$ are the Arrhenius functions of the temperature [i.e. they are proportional to $\exp(-E_g/T)$]. In this case, the solution corresponding to the stationary evaporation wave proves to be unstable in some domain of parameter values, and an oscillatory evaporation mode sets in. The self-oscillations are caused by the mismatch between the two characteristic velocities of the problem: the velocity of motion of the ablation front and that of the thermal front (the heated layer thickness).
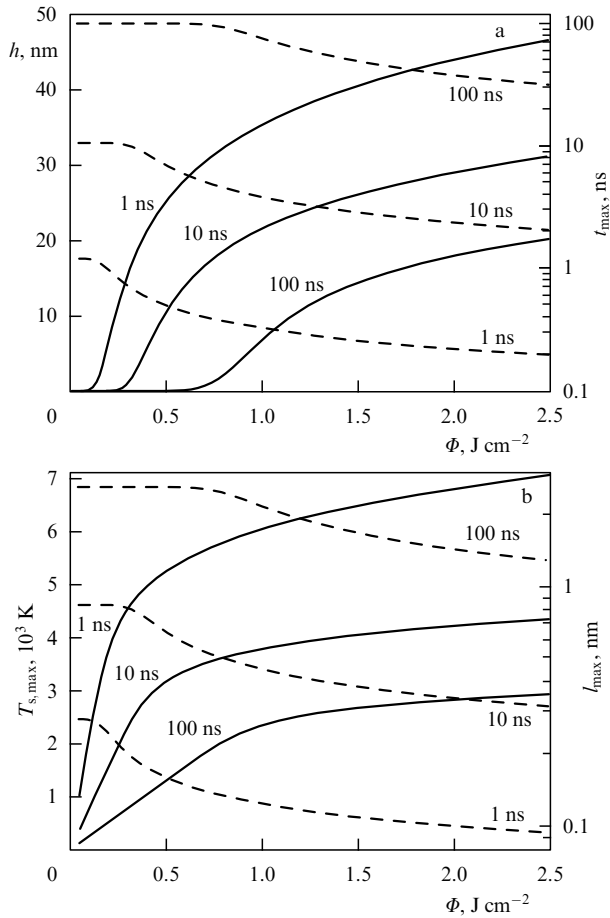
**Figure 6.** Parameters of laser ablation as the functions of fluence for laser pulses of various durations: (a) ablation layer thickness (solid lines) and the point in time at which the temperature attains its peak value (dashed lines); (b) peak surface temperature (solid lines) and the characteristic thermal length at the same point in time (dashed lines). Parameters of the calculations: $\alpha = 10^5$ cm$^{-1}$, $\alpha_g = 10\alpha$; the remaining parameters are the same as in Fig. 4.

# 3. Subpicosecond laser ablation. Two-temperature model

When employing shorter (subpicosecond) laser pulses, in ablation kinetics the features appear which can no longer be described in the context of the conventional thermal model. Meanwhile, the ablation of materials with the aid of ultrashort (subpicosecond) laser pulses is applied in 'high technologies' for micromechanical processing [6, 10]. Research in this field is also of purely scientific interest, because the mechanisms responsible for the material removal by ultrashort laser pulses are still the subject of debate. The ablation problem has several features relating to the energy absorption, the electron–phonon interaction, the mechanism of transferring material to the vapor–gas state, and vapor expansion [4]. In the case of metal ablation, we can point out the effects related to the electron–phonon interaction and those caused by the hot electron gas in the material.

A two-temperature model for the description of transition phenomena in a nonequilibrium electron gas and a lattice under subpicosecond laser irradiation was proposed more
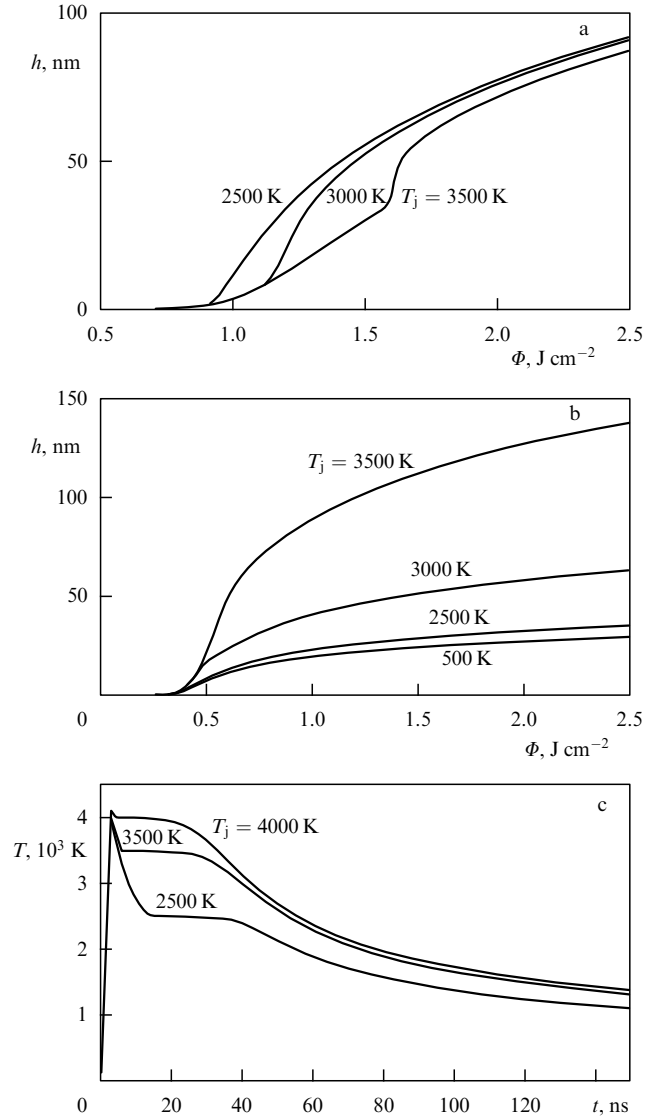
[4] Different aspects of subpicosecond laser ablation are the concern of Refs [185–188].



**Figure 7.** (a) Jumps in laser ablation, which are caused by the temperature variation of the absorptivity (2.31), for different switching temperatures $T_j$. The absorptivity changed from $A_1 = 0.4$ to $A_2 = 0.6$; the switching temperature interval was $\Delta T = 10$ K; the FWHM of the laser pulse was 15 ns; $\alpha = 10^5$ cm$^{-1}$, $\alpha_g = 2\alpha$; the remaining parameters are the same as in Fig. 4. (b) Effect of the temperature jumps in the absorption by ablation products for

$$\alpha_g(T) = 10\alpha \left( \frac{1}{2} + \frac{1}{\pi} \arctan \frac{T - T_j}{\Delta T} \right), \quad \alpha = 10^5 \text{ cm}^{-1}, \quad \Delta T = 10 \text{ K}.$$

(c) Effect of thermal memory for a fluence $\Phi = 2.5$ J cm$^{-2}$ and different switching temperatures; the FWHM of the laser pulse was 15 ns.

than 30 years ago [16, 18, 46]. For a detailed comparison of this model with experiment, different characteristics should be measured with a subpicosecond temporal resolution, which is by itself an intricate task [47–51]. Some characteristics are hard to measure directly at all. That is why the analysis of physical mechanisms involved in the ablation process by ultrashort laser pulses has to be performed on the basis of a theoretical consideration of 'indirect' experimental data.

The electron–phonon interaction dynamics was investigated with the aid of a kinetic equation by Fal'kovskiĭ et al. [52]. This research lends support to the validity of the basic ideas underlying the two-temperature model, enables one to

determine the electron–phonon interaction constant, and permits several kinetic coefficients to be expressed in terms of microscopic metal characteristics. However, more detailed models call for more complex numerical calculations, which is associated with the use of high-performance computers and modern numerical techniques.

The two-temperature model describes the energy transfer inside a metal by application of the coupled heat conduction equations for the temperatures of electrons $T_e$ and the lattice (phonons) $T_i$:

$$c_e \frac{\partial T_e}{\partial t} = c_e v \frac{\partial T_e}{\partial z} + \frac{\partial}{\partial z}\left(\varkappa_e \frac{\partial T_e}{\partial z}\right) + Q - \mu(T_e - T_i), \quad (3.1)$$

$$c_i \frac{\partial T_i}{\partial t} = c_i v \frac{\partial T_i}{\partial z} + \frac{\partial}{\partial z}\left(\varkappa_i \frac{\partial T_i}{\partial z}\right) + \mu(T_e - T_i). \quad (3.2)$$

Here, $c_e$ and $c_i$ are the specific heat capacities [J cm$^{-3}$ K$^{-1}$] of the electrons and the lattice, respectively, $\varkappa_e$ and $\varkappa_i$ are the corresponding thermal conductivity coefficients, and the parameter $\mu = c_e/\tau$ characterizes the rate of energy exchange [W cm$^{-3}$ K$^{-1}$] between the electron and lattice subsystems ($\tau$ is the characteristic exchange time for the electron subsystem).

The absorption of the laser energy by electrons is described employing the source [see Eqn (2.10)]

$$Q = -\frac{\partial I}{\partial z} = \alpha I, \qquad I(0,t) = I_s(t), \quad (3.3)$$

where $\alpha$ is the absorption coefficient, and $I_s$ is the radiation intensity at the metal surface ($z = 0$). The quantity $I_s(t) = AI(t)$ in expression (3.3) depends on the laser pulse shape $I(t)$, for instance, of the form (2.21), and the absorptivity $A = 1 - R$ of the material ($R$ is the radiation reflection coefficient). In the case of an ultrashort laser pulse, the plume is produced upon cessation of the pulse and has no effect on the ablation process.

The heat conduction equations (3.1) and (3.2) are written in the ablation-front frame of reference; the ablation front travels with a velocity $v = v(t)$ relative to the immobile material. This formulation is slightly different from the conventional two-temperature model [44, 53], from which several small parameters were omitted. However, we will take advantage of this form, because it is convenient for the analysis of a stationary evaporation wave.

The boundary conditions specify the energy fluxes at the surface $z = 0$:

$$-\varkappa_e \frac{\partial T_e}{\partial z}\bigg|_{z=0} = J_e, \quad (3.4)$$

$$J_e = -k_0 b_0 (T_{e,s} + T_\infty)^2$$
$$\times \exp\left(-\frac{T_u}{T_{e,s} + T_\infty}\right) \quad \text{(the Richardson law)}, \quad (3.5)$$

where $b_0$ is the Richardson constant, and $T_u$ is the work function. The factor $k_0 = k_B(T_{e,s} + T_\infty)/e$ in expression (3.5) is used to convert the energy flux density $J_e$ into energy units [W cm$^{-2}$].

Similarly, the thermal flux related to energy losses due to material removal (ablation) is given by a formula similar to expression (2.12):

$$-\varkappa_i \frac{\partial T_i}{\partial z}\bigg|_{z=0} = J_i = -\rho v L. \quad (3.6)$$

The two other boundary conditions (for $z = \infty$) and the initial conditions (for $t = 0$) are evident:

$$T_e\big|_{z=\infty} = T_i\big|_{z=\infty} = T_e\big|_{t=0} = T_i\big|_{t=0} = 0. \quad (3.7)$$

As in Section 2, the subscript 's' is used for denoting the temperature at the surface $z = 0$, i.e. $T_e\big|_{z=0} = T_{e,s}$ and $T_i\big|_{z=0} = T_{i,s}$. The quantity $T_{e,s}$ enters the Richardson law, and the quantity $T_{i,s}$ determines the laser ablation rate which is written down like formula (2.1):

$$v = v_0 \exp\left(-\frac{T_a}{T_{i,s} + T_\infty}\right). \quad (3.8)$$

For the model to be suitable for the analysis of experimental data, account must be taken of the temperature dependences of the coefficients $c_e$, $c_i$, $\varkappa_e$, $\varkappa_i$, $A$, $\alpha$, and $\mu$. For instance, the electron heat capacity is linear with respect to the electron temperature: $c_e = \beta T_e$. The lattice heat capacity $c_i$ is practically constant for temperatures higher than the Debye temperature $T_D$. However, if calculations are performed with the inclusion of melting process and other structural phase transitions, the effective lattice heat capacity $c_i$ depends on the lattice temperature $T_i$. The electron heat conductivity $\varkappa_e$ depends on the temperatures $T_e$ and $T_i$ [51, 53]. The reflection coefficient $R$ and the absorption coefficient $\alpha$ also depend on the temperatures $T_e$ and $T_i$ in the general case. In semiconductors, the reflection coefficient $R$ varies linearly with the electron temperature $T_e$ [51].

The majority of the above-given temperature dependences may be taken into account in the calculations in the same manner as for the one-temperature thermal model employing the moments method [30]. To illustrate the main features of the two-temperature model, we consider a simplified problem in which all the coefficients are assumed constant.

One more circumstance is worthy of mention. The two-temperature model (3.1) and (3.2) applies when advantage can be taken of the classical Fourier laws to describe the electron and phonon thermal energy transfer. This implies that the model is appropriate for times much longer than the characteristic settling time $\tau_e$ for equilibrium distribution in the electron gas. The time $\tau_e$ depends on the electron temperature (on the energy density in a laser pulse); in typical cases it amounts to several hundred femtoseconds [51].

The assumption of diffusive electron energy transfer (3.1) implies in its turn that the characteristic variations in electron temperature distribution occur on spatial scales greater than the electron mean free path $l_e$. Over shorter lengths, the electron transport is primarily ballistic. For various metals, the quantity $l_e \approx v_F \tau_e$ (where $v_F$ is the Fermi electron velocity) differs by more than an order of magnitude. For nickel, for instance, the electron mean free path $l_e$ is several tens of nanometers, whereas for gold it is equal to hundreds of nanometers [54, 55].

When the relaxation time $\tau \to 0$ ($\mu \to \infty$), the two-temperature model goes over into the thermal model with a single temperature $T = T_i \equiv T_e$ of the solid; in this case, the quantities $c = c_e + c_i$ and $\varkappa = \varkappa_e + \varkappa_i$ are the total heat capacity and the thermal conductivity coefficient of the solid.

For a constant radiation intensity ($I_s = \text{const}$), the solution of the problem (3.1)–(3.8) asymptotically approaches the solution which describes the stationary evaporation wave. This solution is an attractor and is important for understanding the general features of the

problem. It is rather simple in form:

$$T_e = T_{e1} \exp(-p_1 z)$$

$$- \frac{\alpha T_{e,s} + (p_1 - \alpha) T_{e1} - J_e/\varkappa_e}{p_2 - \alpha} \exp(-p_2 z)$$

$$+ \frac{p_2 T_{e,s} - (p_2 - p_1) T_{e1} - J_e/\varkappa_e}{p_2 - \alpha} \exp(-\alpha z), \quad (3.9)$$

$$T_i = T_{i1} \exp(-p_1 z)$$

$$- \frac{\alpha T_{i,s} + (p_1 - \alpha) T_{i1} - J_i/\varkappa_i}{p_2 - \alpha} \exp(-p_2 z)$$

$$+ \frac{p_2 T_{i,s} - (p_2 - p_1) T_{i1} - J_i/\varkappa_i}{p_2 - \alpha} \exp(-\alpha z), \quad (3.10)$$

where $T_{e,s} = T_e\big|_{z=0}$ and $T_{i,s} = T_i\big|_{z=0}$ are the corresponding temperatures at the surface, and $T_{e1}$ and $T_{i1}$ are determined from the boundary conditions.

The characteristic exponents $p_1 = 1/l_1$ and $p_2 = 1/l_2$ are the roots of the dispersion equation [56]

$$\Pi(p) \equiv a_3 p^3 - a_2 p^2 + a_1 p + a_0 = 0, \quad p = \frac{1}{l}, \quad (3.11)$$

$$a_3 = \varkappa_e \varkappa_i, \quad a_2 = (c_i \varkappa_e + c_e \varkappa_i) v,$$

$$a_1 = c_e c_i v^2 - \mu(\varkappa_e + \varkappa_i), \quad a_0 = (c_e + c_i) v \mu$$

($p_1$ and $p_2$ correspond to the roots with a positive real part).

The greater root $p_1 = 1/l_1$ of the dispersion equation (3.11) is real and positive. It is given by the Cardano formula

$$p_1 = \frac{1}{3a_3} \left[ a_2 + \left( \frac{g + \sqrt{g^2 + 4b^3}}{2} \right)^{1/3} \right.$$

$$\left. - b \left( \frac{2}{g + \sqrt{g^2 + 4b^3}} \right)^{1/3} \right], \quad (3.12)$$

$$g = 2a_2^3 - 9a_1 a_2 a_3 - 27 a_0 a_3^2, \quad b = 3a_1 a_3 - a_2^2.$$

The two other roots of the dispersion equation (3.11) contain the factors $1 \pm i\sqrt{3}$. The positive root $p_2 = 1/l_2$ is defined as

$$p_2 = \frac{1}{3a_3} \left[ a_2 - \frac{1 + \sqrt{3}\,i}{2} \left( \frac{g + \sqrt{g^2 + 4b^3}}{2} \right)^{1/3} \right.$$

$$\left. + \frac{1 - \sqrt{3}\,i}{2} b \left( \frac{2}{g + \sqrt{g^2 + 4b^3}} \right)^{1/3} \right]. \quad (3.13)$$

For $\tau \to 0$ ($\mu \to \infty$), the root $l_1 \to 0$ and the magnitude of $l_2$ tends to the characteristic thermal length appeared in the surface evaporation model:

$$l_1\big|_{\mu \to \infty} \approx \frac{1}{\sqrt{\mu}} \sqrt{\frac{\varkappa_e + \varkappa_i}{\varkappa_e \varkappa_i}} \to 0, \quad l_2\big|_{\mu \to \infty} = \frac{\chi}{v}, \quad (3.14)$$

where $\chi = (\varkappa_e + \varkappa_i)/(c_e + c_i)$ is the thermal diffusivity of the solid. It is valid to say that $l_2$ is the characteristic length of a thermal wave in the lattice, and $l_1$ is the characteristic length related to the electron temperature distribution.

In paper [53], the dispersion equation equivalent to Eqn (3.11) was given in a somewhat different form (several small terms were omitted from it). For subsequent calculations we shall employ the parameter values typical of metals, for instance, of Al [57].

The terms proportional to $\exp(-z/l_1)$ in the quantities (3.9) and (3.10) do not affect the temperatures themselves, because the $T_{e1}$ and $T_{i1}$ amplitudes are small in comparison with $T_{e,s}$ and $T_{i,s}$. The corresponding terms are nevertheless responsible for the temperature gradients near the surface. An accurate investigation of the temperature distribution on spatial scales $z < l_1 \ll \alpha^{-1}$ (typically, $z \approx 10 - 30$ nm) calls for the inclusion of the ballistic electron transport; in the subsequent discussion we will therefore neglect the effects related to 'fast exponents' in the temperature distributions.

For ultrashort laser pulses, the electron and lattice characteristic heating times differ greatly, whereas the ablation process usually commences after the laser pulse.

Calculations in the framework of a simplified two-temperature model [47, 48, 53, 58], from which the convective terms $v\nabla T_{e,i}$ were omitted, do not allow one to calculate the layer thickness of the material removed by laser pulse irradiation. To do this requires one to take advantage of the complete model (3.1), (3.2) and, what is more, to extend the calculations to times long enough (to times of the order of $10^3$ laser pulse lengths). The late stage of the process was investigated in Ref. [56] employing the moments method.

The trial functions for the temperatures $T_e(z,t)$ and $T_i(z,t)$ were selected in the following form

$$T_e = \frac{1}{1 - \alpha l_e} \left[ \left( T_{e,s} - \frac{l_e}{\varkappa_e} J_e \right) \exp(-\alpha z) \right.$$

$$\left. - \left( T_{e,s} \alpha l_e - \frac{l_e}{\varkappa_e} J_e \right) \exp\left( -\frac{z}{l_e} \right) \right], \quad (3.15)$$

$$T_i = \frac{1}{1 - \alpha l_i} \left[ \left( T_{i,s} - \frac{l_i}{\varkappa_i} J_i \right) \exp(-\alpha z) \right.$$

$$\left. - \left( T_{i,s} \alpha l_i - \frac{l_i}{\varkappa_i} J_i \right) \exp\left( -\frac{z}{l_i} \right) \right]. \quad (3.16)$$

This form of the functions automatically satisfies the boundary conditions for $z = 0$ and $z = \infty$. The trial solutions contain four unknown functions: the characteristic surface temperatures $T_{e,s}(t)$, $T_{i,s}(t)$ and the characteristic scales of lengths $l_e(t)$, $l_i(t)$. A more detailed description may include additional 'fast' exponents and the corresponding preexponential factors.

In accordance with the idea of the method we introduce four moments for electron and lattice temperatures:

$$M_0 = \int_0^\infty T_e \, dz, \quad M_1 = \int_0^\infty T_e z \, dz,$$

$$N_0 = \int_0^\infty T_i \, dz, \quad N_1 = \int_0^\infty T_i z \, dz. \quad (3.17)$$

The differential equations for the moments (3.17) are easy to obtain by integrating the input equations (3.1) and (3.2):

$$c_e \frac{dM_0}{dt} = -c_e v T_{e,s} + J_e + I_s - \mu(M_0 - N_0),$$

$$c_e \frac{dM_1}{dt} = -c_e v M_0 + \varkappa_e T_{e,s} + \frac{I_s}{\alpha} - \mu(M_1 - N_1),$$

$$(3.18)$$

$$c_i \frac{dN_0}{dt} = -c_i v T_{i,s} + J_i + \mu(M_0 - N_0),$$

$$c_i \frac{dN_1}{dt} = -c_i v N_0 + \varkappa_i T_{i,s} + \mu(M_1 - N_1).$$
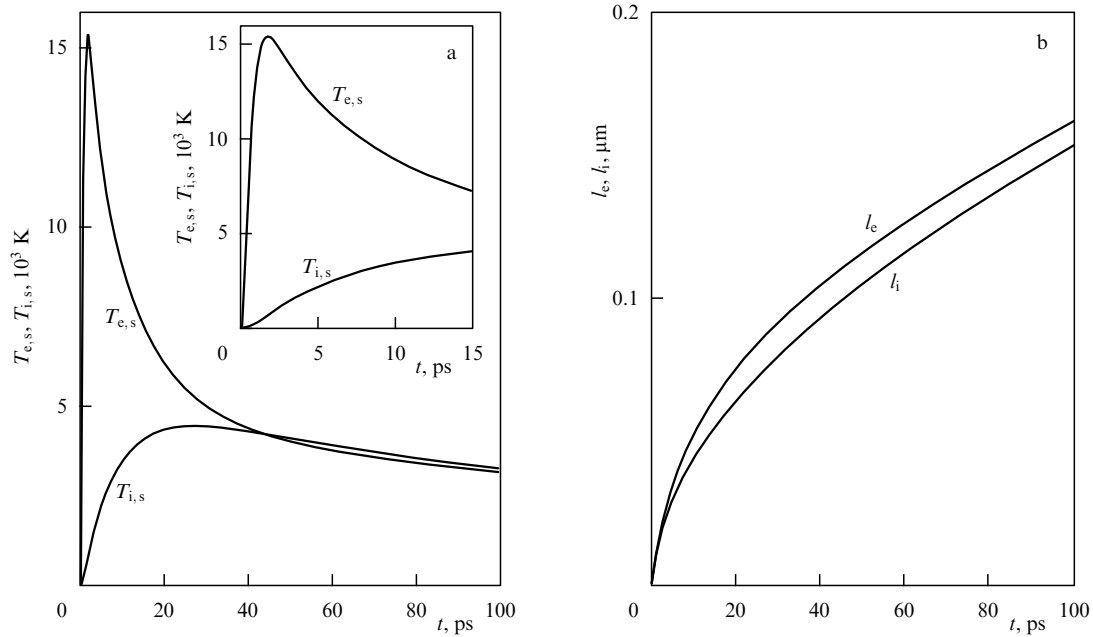
**Figure 8.** Dynamics of metal heating by a laser pulse with a length $t_p = 1$ ps and a pulse energy density $\Phi = 0.15$ J cm$^{-2}$. (a) Electron and lattice temperatures $T_{e,s}$ and $T_{i,s}$ (the inset shows an enlarged view of the initial stage of the process). (b) Characteristic spatial scales $l_e(t)$ and $l_i(t)$ of electron and lattice temperature distributions. Parameters of the calculations: $c_e = 0.04035$ J cm$^{-3}$ K$^{-1}$, $c_i = 2.43$ J cm$^{-3}$ K$^{-1}$, $\varkappa_e = 2.37$ W cm$^{-1}$ K$^{-1}$, $\varkappa_i = 1$ W cm$^{-1}$ K$^{-1}$, relaxation time $\tau = 1$ ps ($\mu = c_e/\tau$), density $\rho = 2.688$ g cm$^{-3}$, latent heat of evaporation $L = 10\,860$ J g$^{-1}$, the factor in formula (3.8) is $v_0 = 414\,000$ cm s$^{-1}$, activation energy $T_a = 35\,240$ K, the work function in expression (3.5) $T_u = 49\,300$ K, the Richardson constant $b_0 = 120.4$ A cm$^{-2}$ K$^{-2}$, initial temperature $T_\infty = 300$ K, absorption coefficient $\alpha = 1.516 \times 10^5$ cm$^{-1}$, and absorptivity $A = 1$.

The subsequent calculation involves substitution of the trial functions (3.15) and (3.16) into expressions (3.17) and equations (3.18). As a result we arrive at a system of four ordinary differential equations for $T_{e,s}(t)$, $T_{i,s}(t)$ and $l_e(t)$, $l_i(t)$. These equations are rather cumbersome (we do not write them down here), but the resultant system of equations is integrated rather fast. Suffice it to say that all the calculations presented below were performed employing a 300-MHz Pentium II PC in several minutes.

Figure 8 shows the dynamics of metal heating by a laser pulse with a duration $t_p = 1$ ps and a pulse energy density $\Phi = 0.15$ J cm$^{-2}$ [the pulse form was modeled by Eqn (2.21)]. Referring to Fig. 8a, it is seen that the electron temperature $T_e$ 'detaches' from the lattice temperature $T_i$ during the laser pulse and peaks at the point in time $t \approx 1.8$ ps. The characteristic lattice heating time is sufficiently longer (this follows from the relation $c_i/\mu \gg c_e/\mu = \tau$); the phonon temperature peaks at $t \approx 27.2$ ps. In this case, the characteristic scales of lengths $l_e$ and $l_i$ (Fig. 8b) increase with time approximately according to the thermal conduction law, i.e. proportionally to $\sqrt{t}$. For long times, the distinction between $l_e$ and $l_i$ becomes insignificant, but even for times $t \approx 100$ ps the difference in their scales is still appreciable: $l_e > l_i$ (since $\varkappa_e > \varkappa_i$).

The results presented in Fig. 8 show that the method involved adequately depicts the qualitative features of the problem revealed, for instance, in Ref. [53]. However, there is also a significant advantage: the moments method allows a fast computation of the late stage of the process, which is significant for the description of ablation. One can see from Fig. 9a that the ablation is completed in a time of the order of 1 ns (this is approximately $10^3$ times longer than the laser pulse). In the traditional experiments, the layer thickness of the material ablated in one laser pulse is measured as a

function of the energy density in the pulse. It is precisely this dependence that is hard to calculate using conventional numerical techniques.

The typical effect of dependence of ablation kinetics on the laser pulse duration is illustrated in Fig. 9b. For a long (nanosecond) laser pulse, the ablation is insensitive to the lattice–electrons energy exchange rate. With $\tau \leqslant 1$ ps, the curves coincide with the results following from the purely thermal ablation model with a single temperature of the lattice and electrons. For short (picosecond) laser pulses, the corresponding curves are sensitive to the characteristic relaxation time $\tau$. When $\tau \to 0$ (the case of a purely thermal model), the curves show too fast a growth of the ablation layer thickness in comparison with experimental dependences (see the discussion of this issue in Ref. [32]).

Another well-known effect is also evident from Fig. 9b: the lowering of the ablation threshold with shortening laser pulse [10]. Therefore, the moments method adequately depicts all qualitative aspects of the problem. The calculations are fast to perform in the context of this method, allowing its use for the analysis of experimental data.

## 4. Hydrodynamic model

### 4.1 Ablation at high irradiation intensities
As previously noted, the simple evaporation model outlined above is valid for temperatures substantially lower than the critical one, when there exists a sharp (of the order of interatomic distance) vapor–condensed phase boundary and the vapor density is many times lower than the condensed material density. As the temperature increases, the sharp interphase boundary fuzzifies into a macroscopic transition layer whose structure and dynamics can be
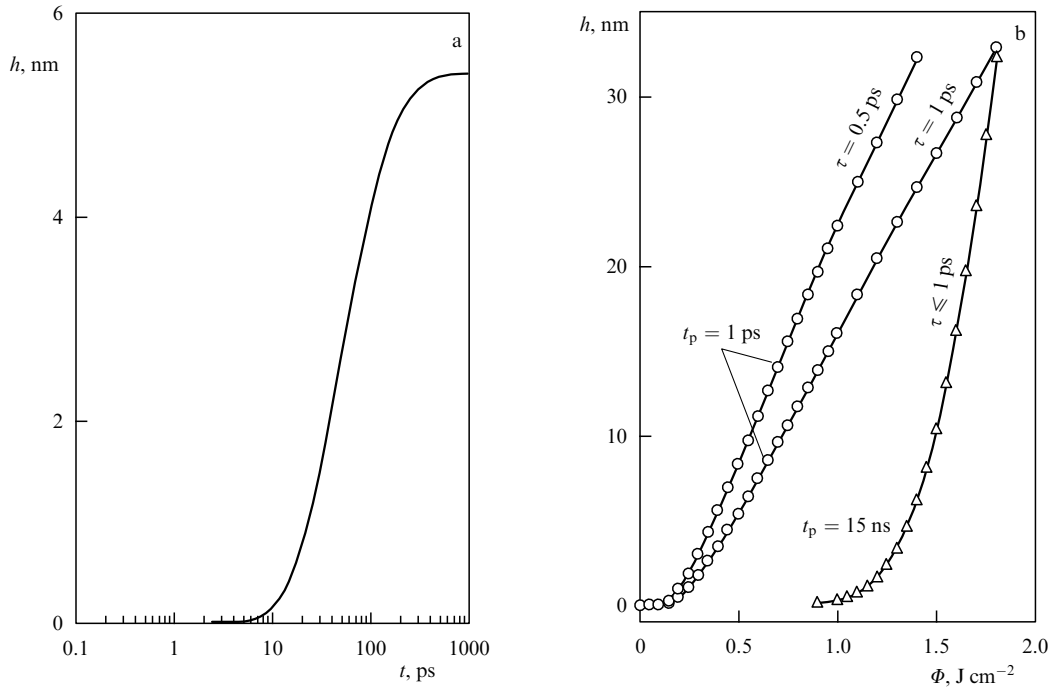
**Figure 9.** (a) Removed material thickness as a function of time. Pulse duration $t_p = 1$ ps, pulse energy density $\Phi = 500$ mJ cm$^{-2}$. (b) Layer thickness of the material removed in one pulse as a function of pulse energy density for one long and two short laser pulses. The parameters of the calculation are indicated in the plots; the remaining parameters are the same as in Fig. 8.

described by the complete system of hydrodynamic equations. This system should be complemented with the equation of state and the data on heat capacity, heat conduction, and electrical conduction of the material in a wide domain of the phase diagram, including the critical point and the two-phase domain.

As of now, a consistent theory of these properties has not been elaborated. In papers [59, 60], the use of experimental data was proposed to obtain the requisite information. Rather complete direct measurements of the equation of state and the conductivity in the circumcritical domain in static experimental conditions were performed for mercury and alkali metals, which have low critical temperatures [61–67]. For the majority of metals we are led to resort to indirect information, which has been successfully extracted from the experiments on dynamic compression in strong shock waves [68–71]. To perform gas dynamics calculations, conventionally advantage is taken of semiempirical equations of state, similar to those proposed in Refs [71–74] and constructed on the basis of experimental data.

A one-dimensional hydrodynamic model for the 'through' numerical computation of laser ablation was constructed in Ref. [75]. Experimental data on the equation of state and the conductivity were employed for the description of material properties in the circumcritical domain. In the range of high temperatures and low densities, recourse was made to the equation of state of an ideal plasma with an equilibrium ionization calculated applying an approximate method [76]. For above-normal densities ($\rho \geqslant \rho_0$) corresponding to the solid metallic state, the pressure was prescribed by a binomial interpolation equation of state [76].

The most complete experimental data on the equation of state in the circumcritical domain are available for mercury [61], and therefore elaborate ablation calculations were

performed for this metal. For other materials, the authors of Ref. [75] invoked the law of corresponding states [77]. According to this law, the parameters which characterize a specific material fall out of any equation of state, containing two of these parameters, on going over to reduced (divided by the corresponding critical values) variables. As noted in Ref. [78], this law holds good for metals; its accuracy rises when the metals refer to the same group of the Periodic Table.

Performing a 'through' computation necessitates prescribing the thermal conductivity and absorption coefficients. The main contribution to the heat conduction in a dense plasma is made by the electron component. The corresponding thermal conductivity coefficient $\varkappa_e$ is related to the static conductivity $\sigma(0)$ by the Wiedemann–Franz law

$$\varkappa_e = \frac{\pi^2}{3} \left(\frac{k}{e}\right)^2 T \sigma(0), \tag{4.1}$$

and it was calculated from the experimentally determined [61–67] static conductivity.

The absorption coefficient for monochromatic radiation is related to the high-frequency conductivity $\sigma(\omega)$ by the expression

$$\alpha_\omega = \frac{4\pi \sigma(\omega)}{c\left[1 - 4\pi \sigma(\omega)/v\right]^{1/2}}, \tag{4.2}$$

where $v$ is the effective collision frequency, and $\omega$ is the laser radiation frequency. Therefore, to determine the absorption coefficient $\alpha_\omega$ we must know the high-frequency conductivity $\sigma(\omega)$, for which experimental data are scarce.

In work [75], the high-frequency conductivity $\sigma(\omega)$ was calculated from the experimentally determined static conductivity $\sigma(0)$. The $\sigma(\omega)$ and $\sigma(0)$ conductivities were assumed to be related by the same expression as in the case

of a rarefied plasma:

$$\sigma(\omega) = \frac{v^2}{v^2 + \omega^2}\, \sigma(0)\,. \qquad (4.3)$$

The static conductivity measurement data were approximated by the formula [63, 79]

$$\sigma(0) = \frac{e^2 n_e}{mv} \exp\left(-\frac{U(\rho)}{T}\right). \qquad (4.4)$$

Here, $n_e$ is a quantity of the order of the electron density in a metal at normal conditions, and $U(\rho)$ has the meaning of the energy gap width in the electronic spectrum. Like in normal metals, the effective collision frequency was assumed to be density- and temperature-dependent: $v \sim v_F l^{-1} \sim Tn^{1/3}$.

The problem of the one-dimensional expansion of a dense metallic plasma under neodymium-laser pulse irradiation with an intensity of $1-10$ GW cm$^{-2}$ and a duration of $10-100$ ns was solved numerically in Ref. [75]. Under these conditions, the degree of metal compression behind the shock front is approximately $1.1-1.2$. The shock-compressed layer width increases with time, because the shock wave is ahead of the thermal wave which acts as a piston. The light is absorbed primarily in a narrow layer near the surface, where $\mathrm{Re}\,\varepsilon(\omega) = 0$. Calculations suggest that the dielectric constant and the hydrodynamic parameters exhibit very strong gradients in this layer. The pressure is constant in front of the absorbing layer. The structure of the latter becomes stationary (in the co-moving frame of reference) from the moment the shock wave detaches from the thermal one.

Interestingly, for a radiation intensity of the order of $5q_0 = 5\rho_c(RT_c)^{3/2}$ (where $R$ is the molar gas constant, and the subscript 'c' indicates the values of the quantities at the critical point), to which there corresponds a temperature in the absorbing layer slightly higher than the critical temperature, a thin layer of condensed dielectric borders on the metallic phase. The dielectric layer thickness is of the order of $10^{-3}$ cm at this intensity. With increasing the latter, the dielectric layer thickness lowers and for $q \approx 50q_0$ it vanishes completely. The disappearance of the dielectric layer is due to the high temperature of the adjacent plasma layer. The same properties are revealed by calculations performed with other radiation frequencies and laser pulse lengths.

With increasing intensity and pulse length, the optical thickness of the absorbing layer increases and amounts to as much as several units. This corresponds to a low (several percent) target reflectivity. Calculations suggest that the absorption region structure and the target surface screening are settled very fast, which justifies the quasi-stationary approach to the problem of high-temperature laser ablation.

## 4.2 Ablation under the action of ultrashort laser pulses

Let us consider in greater detail the ablation of a metal exposed to a laser pulse in the femtosecond range. This problem has acquired special importance in the last few years in connection with the extensive application of femtosecond laser pulses in technology and medicine (see, for instance, Refs [4−7, 10, 80, 81]).

In metals, laser radiation is absorbed primarily by conduction electrons. The radiation energy absorbed in the skin layer propagates deep into the inward regions of the sample by way of electron heat conductivity. Simultaneously there occurs an energy transfer from electrons to the crystal lattice. This process goes slowly on account of the large difference between the electron and ion masses or, which is the same [82], on account of the large difference between the Fermi electron velocity and the sound velocity. Since the electrons in a metal are degenerate and their heat capacity is low, the electron temperature during laser pulse irradiation may far exceed the equilibrium metal temperature. The overheating of electrons relative to the lattice leads to several interesting features in electron emission [83−85] and thermal emission [86−88] of metals absorbing ultrashort laser pulses.

During the course of an ultrashort laser pulse, the heating of the crystal lattice is relatively small. The motion of the material can be neglected at this stage. As noted in Ref. [85], the material motion begins to play a part in a time of the order of the characteristic electron−ion energy exchange time, when the rarefaction wave catches up with the electron thermal wave. Indeed, the electron thermal wave in the metal travels inwards according to the law $X_T \sim \sqrt{\chi_e t} \sim v_e\sqrt{\tau_e t}$, where $\chi_e \sim v_e^2 \tau_e$ is the electron thermal diffusivity, and $\tau_e$ is the electron mean free time.

The hydrodynamic perturbation, which propagates according to the law $X_h \sim ct$, catches up with the thermal wave at the point in time $t^* \sim \tau_e M/m \sim \tau_{e,i}$, where $M$ and $m$ are the respective masses of ions and electrons, and $\tau_{e,i}$ is the electron−ion energy exchange time. In metals having a normal density this time is $1-10$ ps. As a result, by the time of onset of the hydrodynamic motion the target surface layer with a thickness $l_0 \sim \max(\delta, \sqrt{\chi\tau_{e,i}})$ is found to be heated to a temperature $T_0 \sim Q/l_0 c_v$, where $\delta$ is the skin layer depth, $\chi$ is the electron thermal diffusivity, $Q$ is the energy absorbed per unit surface area, and $c_v$ is the heat capacity of a unit volume. In typical experiments involving high-power subpicosecond pulses (see, for instance, Refs [90−92]), the heated layer thickness is of the order of 100 nm, and the temperature is of the order of several thousand degrees.

Therefore, in the conditions of instantaneous heating, in lieu of the conventional problem of ablation front propagation, we need to solve the simpler problem of the adiabatic expansion of a preheated material layer. We note that the detachment of the electron temperature from the lattice temperature, which is significant during the heating stage, is of no importance at the expansion stage. The motion of material can therefore be described by the one-temperature system of gas dynamics equations. As will be seen from the subsequent discussion, the solution to this system of equations depends essentially on the equation of state of the material and the initial entropy of the hot layer. When the entropy is such that the adiabat of the expanding material falls into the two-phase domain in the phase diagram, the flow becomes qualitatively different from the conventional rarefaction wave in an ideal gas. In particular, in the expanding material a liquid layer forms with very sharp boundaries.

The simplest expansion model of an instantaneously heated surface layer was considered in Refs [93−95]. It was assumed that a uniform layer with a thickness $l_0$, heated to a temperature $T_0$, was deposited on an incompressible solid substrate. The initial material density was equal to the normal solid density $\rho_0$ and the initial pressure was defined by the equation of state. The heated layer expanded in vacuum. In this case it was supposed that the local thermodynamic equilibrium in the material was not disturbed during expansion (some remarks on the possible effect of departure from equilibrium will be made below). Wide-range equations of state in tabular form [71, 72] were employed for the numerical calculations in Refs [93−95].
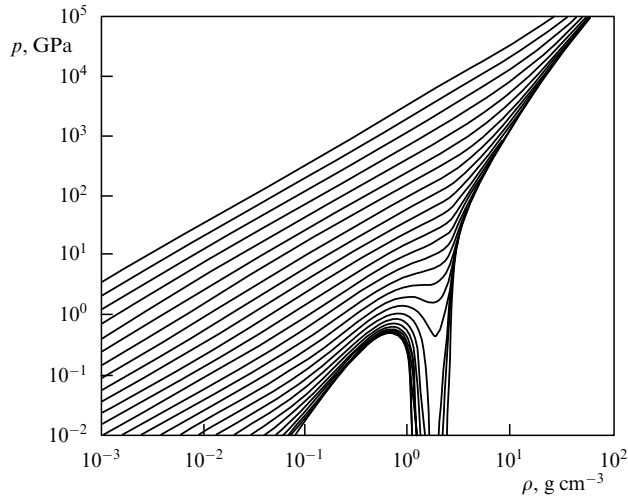
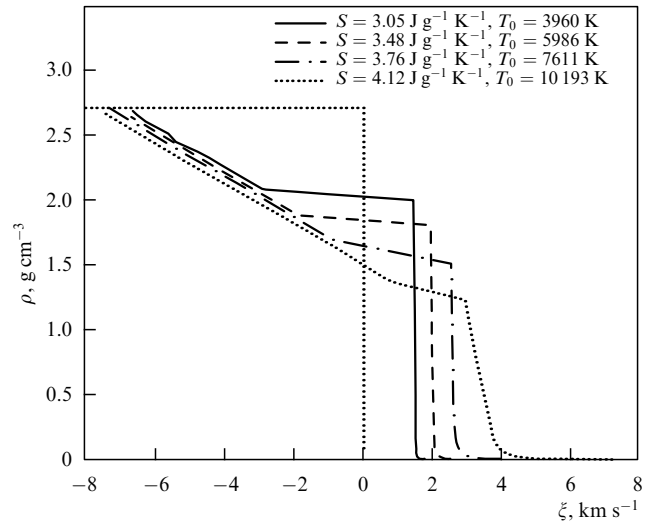**Figure 10.** Phase diagram of aluminium in the variables $(p, \rho)$.



**Figure 11.** Density profiles in the rarefaction wave for different initial temperatures (the values of entropy and initial temperature are indicated at the top of the figure).

Figure 10 depicts the phase diagram of aluminium in the variables $(p, \rho)$. The variation of the material state during expansion follows the adiabat passing through the initial point $(p_a, \rho_a)$. Our interest is in the case when the expansion adiabat intersects the binodal at some point $(p_e, \rho_e)$ in the $(p, \rho)$-plane and enters the two-phase domain. The most important feature of this case is the jumpwise decrease of the velocity of sound at the point where the adiabat intersects the binodal. By calculating the derivative $\gamma(\rho) = (\mathrm{d}\ln p/\mathrm{d}\ln\rho)_S$ with the aid of the tabulated equation of state, it is easy to see that $\gamma(\rho) \gg 1$ in the neighborhood of the $(p_e, \rho_e)$ point in the one-phase domain, whereas in the two-phase domain $\gamma(\rho) \ll 1$. The drastic change in the velocity of sound results in a radical structural rearrangement of the flow.

Let us consider the initial stage of the expansion: $t < l_0/c_0$, where $c_0$ is the velocity of sound in the material with a density $\rho_0$ and a temperature $T_0$. The existence of a substrate in no way affects the flow structure at this stage, and the expansion is described by a centered rarefaction wave [96, 76]. The flow is self-similar and depends on the variable $\xi = z/t$. The time $t$ is counted from the beginning of expansion, and the $z$-coordinate from the outer edge of the heated layer. The $z$-axis points toward the vacuum space. With this choice of the $z$-axis direction, nontrivial solutions of the gas dynamics equations exist if the relation $\xi = u - c$ is fulfilled [96, 76], where $u$ is the flow velocity, and $c$ is the velocity of sound. This solution can be represented by the equation

$$u(\xi) = -I(\xi) = \int_{\rho}^{\rho_0} \frac{c(\rho)}{\rho}\,\mathrm{d}\rho\,. \qquad (4.5)$$

Here $c(\rho)$ denotes the velocity of sound in the adiabat $p = p(\rho)$.

Equation (4.5) implicitly governs the self-similar profiles of thermodynamic variables and velocity in the centered rarefaction wave. Figure 11 shows the density profiles in the rarefaction wave for different initial temperatures. A characteristic feature of the profiles presented is the existence of a plateau which terminates with an abrupt density jump on the vacuum side. This feature is easy to understand by considering the following simplified model in lieu of the real isentrope [94, 95].

Let us assume that the isentrope can be approximated by the power formula $p = C\rho^{\gamma_1}$ with an index $\gamma_1 \gg 1$ in the condensed phase [to the left of the $(p_e, \rho_e)$ point], and in the

two-phase domain by a similar formula with an index $\gamma_2 \ll 1$. When the isentrope is given by a power function, the gas dynamics equations take on a simple form

$$Nc_t + cu_z + Nc_z u = 0\,, \qquad u_t + uu_z + Ncc_z = 0\,, \qquad (4.6)$$

where $N = 2/(\gamma - 1)$, and the subscripts $t$ and $z$ denote partial derivatives with respect to the corresponding variables. In the self-similar case, the system of equations (4.6) is written as

$$cu' + N(u - \xi)c' = 0\,, \qquad (u - \xi)u' + Ncc' = 0 \qquad (4.7)$$

(the prime denotes the derivatives with respect to the self-similar variable $\xi$).

The nontrivial solutions of Eqns (4.7) are obtained when the determinant of the system is zero. This condition assumes the form

$$(u - \xi)^2 = c^2 \qquad \text{or} \qquad \xi = u \pm c\,.$$

As noted above, in our case $\xi = u - c$. We substitute this relation in the system of equations (4.7) to obtain the general solution [96, 76]

$$u = \frac{N\xi}{N+1} + A\,, \qquad c = -\frac{\xi}{N+1} + A \qquad (4.8)$$

in which $A$ is an arbitrary constant determined from the boundary conditions.

We consider portion 1 of the isentrope, corresponding to the condensed phase, in which $\gamma = \gamma_1$. This portion corresponds to a centered rarefaction wave which propagates through the unperturbed homogeneous material. From this condition we determine the constant $A$ to obtain

$$u_1(\xi) = \frac{N_1(\xi + c_0)}{N_1 + 1}\,, \qquad c_1(\xi) = \frac{N_1 c_0 - \xi}{N_1 + 1}\,. \qquad (4.9)$$

Portion 1 of the centered rarefaction wave is located in the segment $-c_0 < \xi < \xi_{1e}$ and borders on the unperturbed heated material along the characteristic $\xi = -c_0$. Another boundary of portion 1 is located at the point $\xi_{1e}$, to which there corresponds the $(p_e, \rho_e)$ point in the $(p, \rho)$-plane. At this point, portion 1 is matched with portion 2, which

corresponds to the two-phase medium with an adiabatic index $\gamma_2$. In going through the $(p_e, \rho_e)$ point from the one-phase domain to the two-phase one, the velocity of sound undergoes a stepwise drop from a value $c_{1e}$ to a value $c_{2e}$.

As noted in the foregoing, the equality $\xi = u - c$ is fulfilled in the rarefaction wave under consideration, and therefore one finds

$$\xi_{1e} = u_{1e} - c_{1e}, \qquad \xi_{2e} = u_{2e} - c_{2e}. \qquad (4.10)$$

Since the flow velocity is continuous at the matching point $(u_{1e} = u_{2e} = u_e)$, from equalities (4.10) it follows that $\xi_{2e} > \xi_{1e}$, i.e. portions 1 and 2 of the centered rarefaction wave cannot be matched directly. A domain of uniform flow should reside in between.

Therefore, the $(p_e, \rho_e)$ point in the $(p, \rho)$-plane corresponds to a finite segment — the plateau region — in the $(\xi, \rho)$-plane. One can see from expressions (4.10) that the plateau width is given by

$$\xi_{2e} - \xi_{1e} = c_{1e} - c_{2e} \approx c_{1e}.$$

From the matching conditions we determine the constant $A$ appearing in expressions (4.8) for portion 2 of the rarefaction wave and put $c_{2e} \approx 0$ and $N_2 = -2$ to obtain

$$u_2(\xi) \approx 2\xi - N_1(c_0 - c_{1e}), \qquad c_2(\xi) \approx \xi - N_1(c_0 - c_{1e}). \qquad (4.11)$$

From relations (4.11) and the isentrope equation follows the expression for $\rho$:

$$\rho_2(\xi) \approx \rho_e \left[ 1 + \frac{\xi - \xi_{2e}}{c_{2e}} \right]^{-2}, \qquad (4.12)$$

where $\rho_e$ is the material density in the plateau region. Owing to the smallness of the velocity of sound in the two-phase domain $c_{2e}$, the material density in portion 2 decreases rapidly for $\xi > \xi_{2e}$.

So far we have been dealing with the expansion of a semi-infinite uniformly heated layer. When the layer has a finite thickness $l_0$ and is deposited on an incompressible substrate, the rarefaction wave reaches the substrate at the point in time $t_r = l_0/c_0$ and is reflected. The reflected wave with a current coordinate $z_r(t)$ reaches the plateau region at the point in time $t_f$ which can be determined by integrating the equation for the reflected characteristic $dz_r/dt = u + c$. In the case of the isentrope power series approximation, a simple calculation yields

$$\frac{t_f}{t_r} = \left( \frac{Nc_0 + l_0/t_r}{Nc_0 - \xi_{1e}} \right)^{(N+1)/2}.$$

For $t > t_f$, the material density behind the reflected wave falls off with time, whereas in the plateau it remains constant and equal to $\rho_e$. By the point in time $t \approx t_f$ the phase transition is completed in the material behind the reflected wave and the material resides in the two-phase state. In this case, the pressure gradient weakens sharply and the motion 'freezes up': the inertial expansion mode sets in. At the moment of 'freezing-up', the motion of the boundary between the plateau and the two-phase domain comes to a halt in the Lagrangian coordinate, i.e. the accumulation of material by the plateau domain terminates. The material density in the two-phase domain falls monotonically to become lower than the density in the plateau domain.

Therefore, the subsequent flow structure becomes asymptotically settled. The plateau domain turns into a thin shell with a density $\rho_e$, moving with a constant velocity. The shell is followed by the two-phase domain in which the velocity depends linearly on the $z$-coordinate (a flow with a uniform deformation) and the material density falls off with time.

The pattern outlined above is illustrated by the direct numerical solution of the one-dimensional system of gas dynamics equations. The material density and flow velocity profiles resulting from the calculations are given in Figs 12 and 13. The computation was performed for an aluminium layer with an initial thickness of 100 nm and an initial temperature of 4000 K, deposited on a cold undistorted substrate. The equation of state of aluminium was calculated using the technique described in Ref. [71]. The liquid shell density was equal to about 2 g cm$^{-3}$ and remained invariable for several nanoseconds. The shell thickness was also constant and equal to about 70 nm. The two-phase domain was a vapor with liquid droplets.

The calculation performed is a crude expansion model of aluminium film heated by an ultrashort laser pulse, which was experimentally studied in Refs [90–92]. An instructive result of these works was the observation of Newton rings, when the expanding film was illuminated with a probing laser beam.
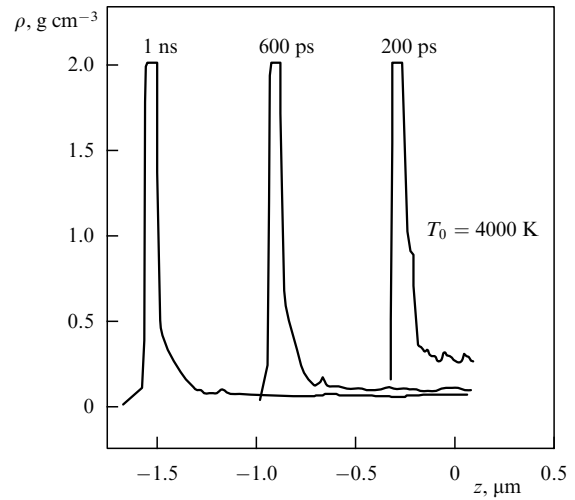
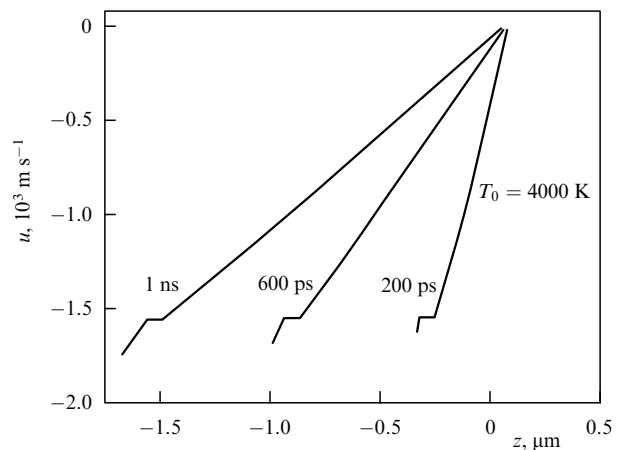**Figure 12.** Material density profile.

**Figure 13.** Flow velocity profile.

Two reflecting surfaces are required for the emergence of the Newton rings in the expanding plume. Proceeding from the above expansion pattern, it may be assumed that one of these surfaces may be the external boundary of the liquid shell, and the other the cold internal target layer. In this case it should be tolerated that the probing radiation is only weakly absorbed by the shell. This admission seems to be plausible because of the smallness of the shell thickness and the decrease of the electron density in the melt metal during expansion [93].

# 5. Photophysical ablation

The above mechanisms of laser ablation may be classified as the mechanisms of surface and volume material removal. These mechanisms may be complicated by one or another of the physicochemical processes in the bulk or at the surface of a solid. In this connection it would be of interest to investigate the mechanism of so-called photophysical laser ablation [29, 97 – 101] caused by the electronic excitation of the material.

The idea which underlies the photophysical ablation mechanism is related to the modification of activation energy for the removal of an electronically excited particle. Although the phenomena of this kind have been much studied in the dissociation of complex organic molecules (see, for instance, Ref. [102]), they are hard to realize in the ablation of solid materials because of the fast relaxation of the electronic excitation.

A rather simple model of photophysical ablation follows from a consideration of a four-level model [99]. It is assumed that on absorption of a photon with an energy $\hbar\omega$ the system experiences a transition from the ground state $N_0$ to the excited state $N_1$ from which it rapidly (the corresponding relaxation time $\tau_1 \to 0$) experiences a transition to the state $N^*$ corresponding to a 'long-lived' singlet or triplet state. This transition scheme allows elimination of the effects of stimulated emission, which are not observed in the ablation of numerous wide-gap materials and organic compounds. It is also assumed that the system in the $N^*$ state can absorb a second photon $\hbar\omega$ [the absorption cross sections $\sigma_{01}(N_0 \to N_1)$ and $\sigma_{12}(N^* \to N_2)$ are different]. The relaxation time $\tau_2(N_2 \to N^*)$ is regarded as being short in comparison with the thermal relaxation time $\tau_T$. The parameter $s = \sigma_{12}/\sigma_{01}$ describes the effects of induced absorption (or bleaching). Schemes of this kind are used, for instance, in the analysis of excitation – relaxation processes in complex organic materials [103].

The system of equations governing ablation now comprises three equations — those for the excited-particle number density $N^*$, the radiation intensity $I$, and the temperature $T$, viz.

$$\frac{\partial N^*}{\partial t} = v \frac{\partial N^*}{\partial z} + (N - N^*) \frac{I\sigma_{01}}{\hbar\omega} - \frac{N^*}{\tau_T} , \qquad (5.1)$$

$$\frac{\partial I}{\partial z} = -I\sigma_{01} \left[ N + (s-1)N^* \right] , \qquad (5.2)$$

$$\frac{\partial T}{\partial t} = v \frac{\partial T}{\partial z} + \chi \frac{\partial^2 T}{\partial z^2} + \left( I\sigma_{01}s + \frac{\hbar\omega}{\tau_T} \right) \frac{N^*}{c\rho} . \qquad (5.3)$$

The velocity $v = v(t)$ of ablation front propagation, which enters Eqns (5.1) – (5.3), is defined as

$$v = \left( 1 - \frac{N_s^*}{N} \right) v_0 \exp \left( -\frac{E}{T_s} \right) + \frac{N_s^*}{N} v_0^* \exp \left( -\frac{E^*}{T_s} \right) , \quad (5.4)$$

where $E$ and $E^*$ are the activation energies required for the removal of unexcited and excited particles from the material, $N$ is the number density of absorbing particles, and the subscript 's' is employed as previously to denote the quantities at the ablation front ($z = 0$).

The boundary conditions assume the form

$$\varkappa \frac{\partial T}{\partial z}\bigg|_{z=0} = H \left( 1 - \frac{N_s^*}{N} \right) v_0 \exp \left( -\frac{E}{T_s} \right)$$
$$+ H^* \frac{N_s^*}{N} v_0^* \exp \left( -\frac{E^*}{T_s} \right) , \qquad (5.5)$$

$$I\bigg|_{z=0} = I(t) \exp \left[ -\alpha_g \int_0^t v(t_1)\, dt_1 \right] , \qquad (5.6)$$

$$N^*\bigg|_{z=\infty} = 0 . \qquad (5.7)$$

Boundary condition (5.6) takes into account the screening of radiation by the vapor of the ablated material.

It is easy to recognize that the main effect of photophysical ablation sets in when $E^* \ll E$, when the second term in expression (5.4) is substantially greater than the first one. The case of high activation energies is particularly attractive, when $E = 3 - 6$ eV and conventional thermal ablation necessitates very high temperatures. The effect is strongly reliant on the laser pulse intensity and the thermal relaxation time $\tau_T$. Examples of practical computations can be found in Refs [97 – 101].

For a laser pulse approximately 10 ns long (a typical value for excimer lasers), photophysical ablation occurs, for instance, when $E^* = 1 - 1.5$ eV and $E = 3 - 6$ eV. In this case, however, the relaxation time $\tau_T$ should range into the hundreds of picoseconds. If the relaxation time $\tau_T$ amounts to tens of picoseconds, only a thin surface layer is photophysically removed at the beginning of the pulse, whereas the subsequent ablation takes place in a purely thermal way [101]. In the case of a short laser pulse, the effect of photophysical ablation is amply manifested even for a relatively low activation energy ($E \approx 1.5$ eV), provided that the condition $E^* \ll E$ is nevertheless retained in this case (see Fig. 14).

According to Aksenov et al. [104], it is not improbable that the photophysical mechanism is observed in the laser ablation of porous silicon. As shown in that paper, the rate of
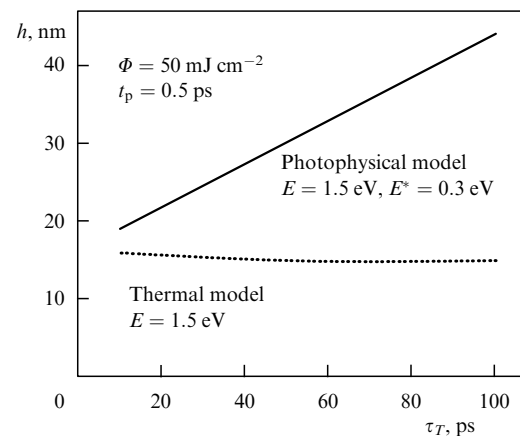
**Figure 14.** Layer thickness of a material removed in one pulse for the thermal and photophysical models [101]. The values of the thermal parameters of the material are typical for specific polymers (polyimide).

ablation of porous silicon by the radiation with a wavelength of 1064 nm was insignificant when employing a pulse with an energy of 400 mJ cm$^{-2}$. Meanwhile, adding a 532-nm synchronous pulse with an energy of only 10 mJ cm$^{-2}$ resulted in a sharp increase of the photoexcitation of porous silicon and in the acceleration of ablation. The authors of Ref. [104] believe to have observed the efficient laser ablation of excited states.

Additional possibilities for the lowering of the activation energy (including that of excited states) are related to the stresses developing in solids heated by a laser [105, 106]. Bulk processes due to photochemical reactions are not ruled out either [107 – 110]. The analysis of nonthermal ablation models is made difficult because detailed experimental data on the dynamics of the process are unavailable. Meanwhile, integral curves can be equally well explained proceeding from different models.

# 6. Gas dynamics of three-dimensional vapor expansion in laser ablation

So far we have considered one-dimensional vapor expansion in the laser evaporation of condensed materials. This consideration corresponds to the initial stage of the process, when the vapor layer thickness is considerably smaller than the focal spot dimension. As the vapor expands, its motion acquires a three-dimensional character. The vapor plume shape and the angular distribution of the vaporized material flow depend on the evaporation mode and the focal spot shape. They in turn determine the thickness profile of the film produced during laser-induced evaporation.

The issue of the angular distribution of expanding laser-ablation products has been comprehensively studied both experimentally and theoretically (see, for instance, Refs [111 – 119]). But almost without exception in the theoretical works the vapor expansion was assumed to be isothermal, which is inconsistent with both the experiment and numerical calculations [118 – 122]. An adiabatic expansion, which is closer to reality, was investigated in paper [116]. However, the analysis made in that work pertains to the special case of an axially symmetric vapor flow, which is not necessarily the case in experiments.

It is pertinent to note that the initial symmetry of a vaporized plume is not 'forgotten' in the course of its expansion. Quite the reverse. As is evident from what follows, the plume shape late in the expansion and the film deposition profile are determined by precisely the initial asymmetry. For instance, the experiments of Refs [113 – 115] and many others show that an elliptic focusing spot results in the production of an elliptically shaped spot of the material deposited on the substrate, the axes of the latter being turned through an angle of 90° (the so-called flip-over effect). It is clear that effects of this kind cannot be explained in the context of an axially symmetric model.

We note that the spatial structure of the vapor (plasma) plume produced at the surface of a solid target under the action of a nanosecond laser pulse was studied in detail as far back as the 1960s. A dense ($n > 10^{21}$ cm$^{-3}$) plume of vaporized material was found (see, for instance, Ref. [118]) to form immediately at the target surface, with its dimension increasing with time. The increase in plume dimensions is primarily related to the evaporation of the target material and slows down abruptly after the pulse termination. Then the apparent boundary of the dense

plume begins to move back to the surface due to the free expansion of outer layers.

We consider now the vapor plume expansion in greater detail. Since the vaporized material density is high, the vapor motion will be described by gas dynamics equations. As shown by Basov et al. [118], when the radiation intensity is high enough the vapor plume is surrounded by a tenuous plasma shell whose outer layer is made up of electrons, and the inner one of ions. Because of its small mass, the plasma shell has almost no effect on the expansion dynamics of the dense core.

The investigation of three-dimensional vapor expansion described below is based on the particular solution of gas dynamics equations, which describes the flow with a uniform deformation [123]. One-dimensional flows of this type (the expansion velocity is proportional to the distance from the center of symmetry) were considered in Ref. [124]. The general three-dimensional case was investigated in Ref. [123]; it was shown that the system of gas dynamics equations may be reduced under specific conditions to a system of ordinary differential equations which describes the motion of a probe particle in a nine-dimensional space. A similar result was later presented in Ref. [125]. In several specific cases, the system of equations obtained in Ref. [123] was integrated by analytical [128] or numerical [116, 126, 127, 129] techniques. A qualitative investigation of this system of equations was performed in Ref. [130].

Particular solutions of the equations of the type under consideration can be obtained for a broad class of initial conditions. The simplest of these solutions have sometimes been employed in the analysis of experimental data on laser-assisted plasma heating and laser ablation [114, 117, 126]. In this case, the temperature in the plume was usually presumed to be coordinate-independent. As noted above (see also Ref. [113]), this formulation of the problem is not quite correct. Since our prime interest here is with the vapor motion after the termination of a laser pulse, the assumption that the vapor flow is isentropic, which was adopted in Ref. [116], seems to be closer to reality and more correct from the physical standpoint. We will adhere to this formulation of the problem.

## 6.1 Dynamics of vapor plume expansion

Let us suppose that the plume formation time (which is close to the laser pulse duration) is far shorter than its expansion time. For this reason, the plume expansion in vacuum can be considered independently of its formation. We consider the focal spot to be elliptic in shape with semiaxes $X_0$ and $Y_0$. The expansion of a vaporized material plume can be modeled on the adiabatic expansion of a three-axial gas ellipsoid whose initial semiaxes are $X_0$, $Y_0$, and $Z_0 \approx c\tau_1$, where $\tau_1$ is the laser pulse duration, and $c$ is the initial velocity of sound in the vaporized material.

The ellipsoid expansion is described by the gas dynamics equations

$$\frac{\partial \rho}{\partial t} + \mathrm{div}\,(\rho \mathbf{v}) = 0 \,,$$

$$\frac{\partial \mathbf{v}}{\partial t} + (\mathbf{v}\nabla)\mathbf{v} + \frac{1}{\rho}\,\nabla p = 0 \,, \qquad (6.1)$$

$$\frac{\partial S}{\partial t} + \mathbf{v}\nabla S = 0 \,.$$

The vaporized material is described by the equation of state of an ideal gas with an adiabatic index $\gamma = c_p/c_v$. The particular solution of Eqns (6.1) of interest to us is of the form

$$r_i(t) = F_{ik}(t)\, r_k(0)\,, \qquad i = x, y, z\,. \tag{6.2}$$

Here $r_i(t)$ are the coordinates of a gaseous particle, with a summation being taken over the recurrent indices. If the ellipsoid rotation is neglected, the $F_{ik}(t)$ matrix takes on a diagonal form

$$F_{ik} = \begin{pmatrix} \dfrac{X(t)}{X_0} & 0 & 0 \\[2ex] 0 & \dfrac{Y(t)}{Y_0} & 0 \\[2ex] 0 & 0 & \dfrac{Z(t)}{Z_0} \end{pmatrix}. \tag{6.3}$$

For adiabatic gas motion of the form (6.2), the system of gas dynamics equations (6.1) can be shown to reduce to a system of ordinary differential equations [130], provided that the gas density and pressure can be represented as follows

$$p(\mathbf{r}, t) = h(t)\, H(\chi)\,, \qquad \rho(\mathbf{r}, t) = f(t)\, \frac{\mathrm{d}H}{\mathrm{d}\chi}\,,$$

$$\chi = g_{ik}\, r_i(0)\, r_k(0)\,, \tag{6.4}$$

$$f(t) = A\, \det^{-1} F_{ik}\,, \qquad h(t) = B\, \det^{-\gamma} F_{ik}\,,$$

where $A$ and $B$ are the constants, and $g_{ik}$ is a constant symmetric matrix.

We rearrange Eqns (6.1) with allowance made for expressions (6.2)–(6.4) and arrive at the system of ordinary differential equations for the matrix elements $X(t)$, $Y(t)$, and $Z(t)$, which is conveniently written as the system of equations of the probe particle motion in classical mechanics:

$$\ddot{X} = -\frac{\partial U}{\partial X}\,, \qquad \ddot{Y} = -\frac{\partial U}{\partial Y}\,, \qquad \ddot{Z} = -\frac{\partial U}{\partial Z}\,, \tag{6.5}$$

$$U = \frac{5\gamma - 3}{\gamma - 1}\, \frac{E}{M}\left(\frac{X_0 Y_0 Z_0}{XYZ}\right)^{\gamma - 1}\,,$$

$$E = (\gamma - 1)\int p(\mathbf{r}, 0)\,\mathrm{d}V\,, \qquad M = \int \rho(\mathbf{r}, t)\,\mathrm{d}V\,.$$

Then we write down the initial conditions for the system of equations (6.5):

$$X(0) = X_0\,, \qquad Y(0) = Y_0\,, \qquad Z(0) = Z_0\,,$$
$$\dot{X}(0) = \dot{Y}(0) = \dot{Z}(0) = 0\,. \tag{6.6}$$

When writing the initial conditions (6.6) we imply that the initial kinetic energy of the vapor is far less than its thermal energy.

In the general case Eqns (6.5) should be solved numerically. Examples of numerical integration of such equations can be found in papers [114, 116, 117, 125–127]. As shown in Ref. [128], for $\gamma = 5/3$ [in terms of the equations of mechanics (6.5) this corresponds to a field potential which is a homogeneous function of coordinates of the degree $-2$] the system of equations (6.5) possesses an additional integral which in many cases permits this system to be integrated in quadratures.

We now turn to the numerical integration of the system of equations (6.5). To do this we select the coordinate axes in

such a way that $X_0 \geqslant Y_0$. In other words, the length of longest semiaxes of the initial gas ellipsoid will be denoted as $X_0$. We introduce the dimensionless variables

$$\xi = \frac{X}{X_0}\,, \qquad \eta = \frac{Y}{X_0}\,, \qquad \zeta = \frac{Z}{X_0}\,, \qquad \tau = \frac{t\beta^{1/2}}{X_0}\,,$$

$$\eta_0 = \frac{Y_0}{X_0}\,, \qquad \zeta_0 = \frac{Z_0}{X_0}\,, \qquad \beta = (5\gamma - 3)\,\frac{E}{M}\,.$$

Then the equations of motion (6.5) and the initial conditions (6.6) may be rearranged to give

$$\xi\ddot{\xi} = \eta\ddot{\eta} = \zeta\ddot{\zeta} = \left(\frac{\eta_0 \zeta_0}{\xi\eta\zeta}\right)^{\gamma - 1}\,,$$

$$\xi(0) = 1\,, \qquad \eta(0) = \eta_0\,, \qquad \zeta(0) = \zeta_0\,, \tag{6.7}$$

$$\dot{\xi}(0) = \dot{\eta}(0) = \dot{\zeta}(0) = 0\,.$$

In the dimensionless variables the energy integral is written as

$$\frac{1}{2}(\dot{\xi}^2 + \dot{\eta}^2 + \dot{\zeta}^2) + \frac{U(\tau)}{\beta} = \varepsilon = \text{const}\,,$$

where $\varepsilon = (\gamma - 1)^{-1}$. In the special case when $\gamma = 5/3$ there occurs an additional integral of the system of equations (6.5):

$$\xi^2 + \eta^2 + \zeta^2 = 3\tau^2 + 1 + \eta_0^2 + \zeta_0^2\,.$$

The sought solution depends on three parameters: $\eta_0$, $\zeta_0$, and $\gamma$. From Eqns (6.7) it immediately follows that the gas plume in its late stage expands through inertia. In this case, the ratios between the lengths of ellipsoid axes for $\tau \to \infty$, which define the plume shape, tend to some limiting values. We can conveniently introduce the ratios $k_\eta(\tau) = \eta(\tau)/\xi(\tau)$ and $k_\zeta(\tau) = \zeta(\tau)/\xi(\tau)$, which characterize the plume shape at a point in time $\tau$. Examples of the dependences $k_\eta(\tau)$ and $k_\zeta(\tau)$ for different values of the parameters $\eta_0$, $\zeta_0$, and $\gamma$, which result from the numerical solution of Eqns (6.5), are presented in Fig. 15.

Figure 15a shows the time evolution of the plume shape for different values of the adiabatic index $\gamma$ and fixed values of $\eta_0$ and $\zeta_0$. Notice that for $\gamma < 5/3$ the ratio between the semiaxes $k_\eta(\tau)$ peaks for a finite value of $\tau$ and approaches the asymptotic value $k_\eta(\infty)$ from above. For $\gamma \geqslant 5/3$, the function $k_\eta(\tau)$ increases monotonically with $\tau$ to attain the limiting value $k_\eta(\infty)$ when $\tau \sim 10^3$. The $k_\zeta(\tau)$ function exhibits a similar behavior (Fig. 15d).

A family of $k_\eta(\tau)$ curves corresponding to different values of $\eta_0$ and fixed values of $\gamma$ and $\zeta_0$ is plotted in Fig. 15b. For $\tau \sim 10$, the $k_\eta(\tau)$ function attains a value $k_\eta = 1$. At this point in time, the expanding plume becomes symmetric about the $z$-axis. Subsequently, the $k_\eta$ function continues to increase, i.e. the plume expands faster in the direction of the stronger initial pressure gradient (in the direction of the short axis of the focal spot). As a result, the spot deposited is found to be as if rotated through an angle of $90°$ relative to the focal spot. This experimentally discovered phenomenon has come to be known as the 'flip-over effect'. Clearly, the same rotation effect should be observable for a focal spot of any shape possessing an $n$th-order axis of rotation $C_n$. In this case, the angle of rotation is $180°/n$. In
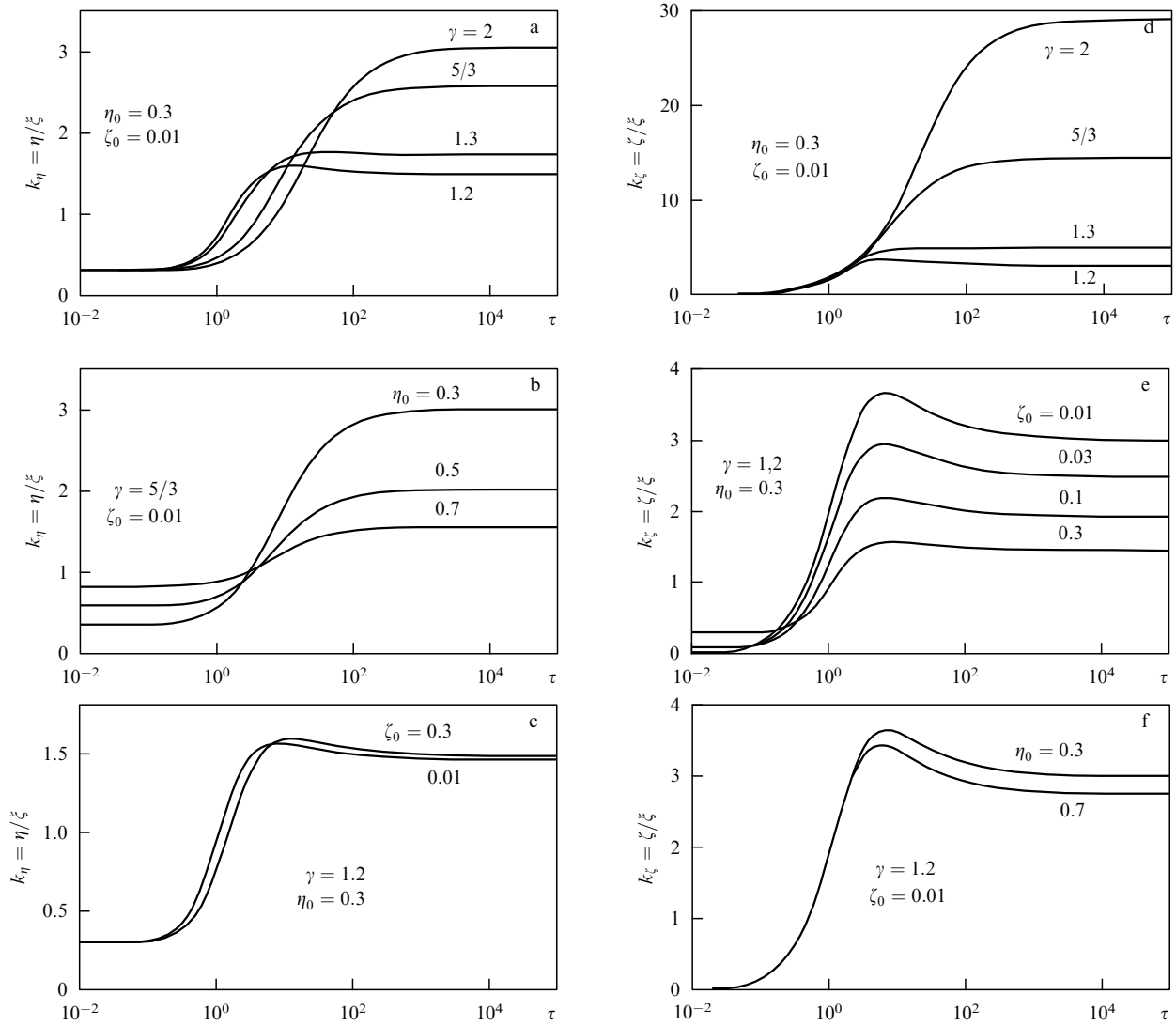
**Figure 15.** Effect of parameters $\gamma$, $\eta_0$, and $\zeta_0$ on the character of plume expansion in the $xy$-plane (a – c) and the $xz$-plane (d – f).

particular, this angle is equal to 90° for a rectangular focal spot (like for an ellipse), 45° for a square, and 60° for an equilateral triangle. Effects of this kind were observed by Kelly and Miotello [132].

The family of curves in Fig. 15c serves to illustrate the effect of the $\zeta_0$ parameter on the character of plume expansion in the $xy$-plane. One can see that this effect is insignificant for the values of $\eta_0$ and $\gamma$ specified above: varying $\zeta_0$ by a factor of 30 causes $k_\eta$ to change by only a few percent. As $\gamma$ increases and $\eta_0$ decreases, this influence becomes more significant. Figure 15e demonstrates a strong dependence of the $k_\zeta(\tau)$ function on the parameter $\zeta_0$, and Fig. 15f a weak dependence of $k_\zeta(\tau)$ on $\eta_0$.

To summarize, it is valid to say that the plume expansion is a superposition of two weakly interacting motions. For a given adiabatic index $\gamma$, the plume expansion in the direction of the $y$-axis is determined by the parameter $\eta_0$, and in the direction of the $z$-axis by the parameter $\zeta_0$. For $\tau \sim 10^2 - 10^3$, both motions become inertial and the ratios between the lengths of ellipsoid axes remain approximately equal to their asymptotic values. These values are given in Ref. [129] for a broad range of parameter values.

## 6.2 Deposited film profile
The simple model considered above furnishes an opportunity to estimate, without conducting complex three-dimensional gas dynamics calculations, the manner in which the focal spot shape influences the spatial structure of vapor flow and the thickness profile of the film produced in the condensation of the vapor on the substrate. All one has to do is to calculate the flux of material at the point of location of the substrate, i.e. for $z = z_s$. This flux is defined as $j = \rho v_z$, where the density and the corresponding velocity component are found from the particular solution of the gas dynamics problem, derived in the previous section.

Integrating the flux $j$ with respect to time from zero to infinity gives the distribution of the deposited mass. For the inertial stage of expansion, such a calculation leads to the formula [129]

$$ h = h_0 \left( 1 + \frac{1}{p} \tan^2 \theta_x + \frac{q^2}{p} \tan^2 \theta_y \right)^{-3/2}. \qquad (6.8) $$

Here, $h_0$ is the peak film thickness at the deposition center, the quantities $p$ and $q$ are defined as $p = 1/k_\zeta(\infty)$ and $q = 1/k_\eta(\infty)$, and the angles $\theta_x = \arctan(x/z_s)$, $\theta_y =$

arctan $(y/z_s)$. For small angles $\theta_x$ and $\theta_y$, the above equation coincides with the commonly used asymptotic formula

$$h(\theta_x, \theta_y) = h_0 \cos^m \theta_x \cos^n \theta_y, \qquad (6.9)$$

where $m = 3/p^2$ and $n = 3q^2/p^2$. As shown by Tyunina et al. [133], formula (6.8) provides an adequate description of the real deposition profile.

### 6.3 Dynamics of a multicomponent plume. Matrix-assisted evaporation

In recent years, considerable study has been given to the technique of evaporation of large molecules from specially prepared matrices — the so-called MALDI technique (Matrix-Assisted Laser Desorption and Ionization). This technique is employed for the quick mass analysis of very heavy biomolecules (up to several hundred thousand daltons) [134, 135]. The idea underlying this technique is simple enough. Large molecules are impossible to vaporize directly using a laser due to their rapid thermal and photochemical decomposition. However, it is possible to prepare a low-concentration solution of the high-molecular substance and then deposit the solution in the form of a solid matrix. For solvents use is made of low-molecular highly volatile organic substances with a molecular mass of the order of a hundred daltons.

The matrix preparation technique has been thoroughly elaborated to date [136]. In the laser evaporation of the matrix, heavy biomolecules are entrained by the low-molecular vapor to find themselves undecomposed in the gas phase. This permits highly sensitive optical methods to be employed for the spectroscopic analysis of an isolated biomolecule, which is important for many applications, for genetic engineering in particular [137].

Omitting the details, it is valid to say that the vapor plume obtained in the matrix evaporation is a mixture of the vapor of heavy and light molecules. Investigating the expansion dynamics of a multicomponent vapor plume is an intricate task. Special solutions of gas dynamics equations nevertheless make it possible to satisfactorily describe some of the characteristics of this vapor and supply an explanation for several qualitative effects, among them the sharpening effect

in the expansion of heavy molecules (the heavy vapor propagates as a thin elongated jet through the light vapor) [138, 139]. The sharpening effect is clearly visible in the photographs of expansion of light and heavy vapor plumes (Fig. 16).

As before, the formation time of the initial vapor plume will be assumed to be far shorter than its expansion time. We also suppose that the heavy vapor (a high-molecular protein) has no effect on the expansion dynamics of the vapor of the light matrix material. In this case, the expansion of the light vapor can be described by taking advantage of the above special solutions of gas dynamics equations. This vapor will be treated as a three-axial ellipsoid. The quantities related to the light vapor will be designated by the subscript 'l'.

In accordance with Eqns (6.5), the motion of the plume boundaries is described by the equations

$$\ddot{X}_1 = -\frac{\partial U}{\partial X_1}, \qquad \ddot{Y}_1 = -\frac{\partial U}{\partial Y_1}, \qquad \ddot{Z}_1 = -\frac{\partial U}{\partial Z_1}, \qquad (6.10)$$

$$U = \frac{5\gamma_1 - 3}{\gamma_1 - 1} \frac{E_1}{M_1} \left( \frac{X_{10} Y_{10} Z_{10}}{X_1 Y_1 Z_1} \right)^{\gamma_1 - 1},$$

in which $X_{10}$, $Y_{10}$, and $Z_{10}$ are the initial coordinates of the plume, and $\gamma_1$ is the adiabatic index for the light vapor. The initial conditions are of the form

$$X_1(0) = Y_1(0) = R_0, \qquad Z_1(0) = Z_{10},$$
$$\dot{X}_1(0) = \dot{Y}_1(0) = 0, \qquad \dot{Z}(0) = v_{z0}. \qquad (6.11)$$

We will consider isentropic solutions with parabolic density and pressure profiles, specifically

$$\rho_1(\mathbf{r}, t) = \frac{2}{\pi^{3/2}} \frac{\Gamma(\alpha + 5/2)}{\Gamma(\alpha + 1)} \frac{M_1}{X_1 Y_1 Z_1} \left[ \psi_1(x, y, z, t) \right]^\alpha, \quad (6.12)$$

$$\psi_1 = 1 - \frac{x^2}{X_1^2} - \frac{y^2}{Y_1^2} - \frac{z^2}{Z_1^2}, \qquad \alpha = \frac{1}{\gamma_1 - 1},$$

where $\Gamma(z)$ is the gamma-function.

The solutions (6.10) and (6.11) are a good approximation to the expansion dynamics of a real plume (see Figs 17a and
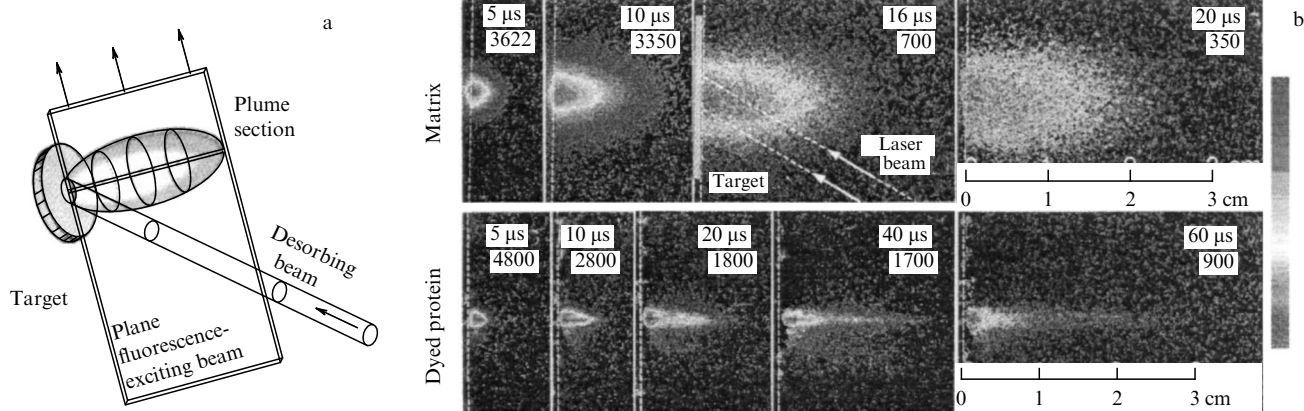


**Figure 16.** (a) Schematic diagram of the experiment and expansion geometry in the matrix-assisted evaporation. A heavy protein marked with dye molecules (a molecular mass of 29062 daltons and a TMR dye with a molecular mass of 444 daltons) was solved in the light material of a 3-HPA matrix (a molecular mass of 139 daltons). The matrix was evaporated under radiation of a KrF excimer laser (an elliptic beam measuring 3.1 mm by 3.6 mm). The laser-induced fluorescence of the substance was initiated with the aid of the second laser with a variable time delay after the vaporizing laser pulse. (b) Top: fluorescence of the matrix material under radiation of an XeCl excimer laser (308 nm), recorded with an ICCD camera at the points in time 5, 10, 16, and 20 μs. Bottom: fluorescence of the dyed protein excited by the second harmonic of an Nd : YAG laser (532 nm) at the points in time 5, 10, 20, 40, and 60 μs. Each photograph was obtained with a separate vaporizing laser pulse [138].
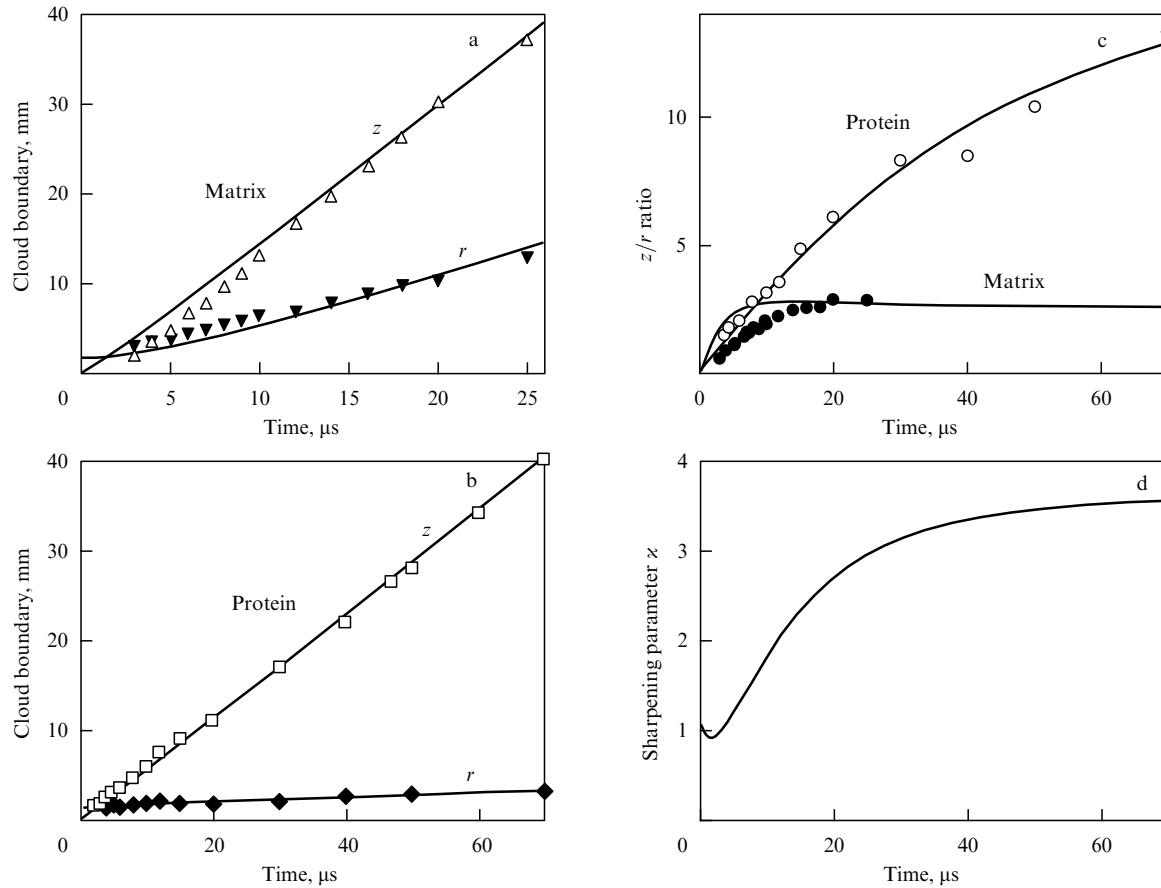
**Figure 17.** Expansion dynamics of the matrix material (a) and the protein (b) in the radial ($r$) direction and normally ($z$) to the surface. (c) Dynamics of $z/r$ asymmetry development in the expansion of the matrix material and the protein. (d) Dynamics of the development of the sharpening effect, i.e. the time variation of the $\varkappa$ parameter. Solid lines represent calculated results and the data points represent measurements.

17b). In the computations it was assumed that $R_0 = 1.8$ mm, which corresponds to the laser beam radius in the experiments carried out by Puretzky et al. [138]. The parameters $Z_{l0}$, $v_{z0}$, and $v_l = \sqrt{E_l/M_l}$ were determined from the best fit by the least square technique. The parameters $v_{z0}$ and $v_l$ are in essence constants rather than adjustable parameters. Their values derived from the experiment were $v_{z0} \approx 6 \times 10^4$ cm s$^{-1}$ and $v_l \approx 3.3 \times 10^4$ cm s$^{-1}$. In principle, the parameter $Z_{l0}$ (the vapor plume thickness at the instant of termination of a laser pulse) can also be found from independent measurements. The $Z_{l0} \approx 100$ μm value determined from the least square fit is in good agreement with the theoretical estimate [116].

Apart from the dynamics of plume boundary motion, which is similar for isothermal and isentropic plumes, of our interest is to verify the applicability of the parabolic spatial profiles inherent in precisely the isentropic solution. The laser-induced fluorescence intensity signal measured in the experiments [138] is proportional to the local density, i.e. the quantity defined by formula (6.12). For a polyatomic gas whose adiabatic index is close to unity [i.e. $1/(\gamma_l - 1) \gg 1$], formula (6.12) can be simplified taking advantage of the well-known relation $(1 - \varepsilon)^{1/\varepsilon} \approx e^{-1}$ for $\varepsilon \ll 1$ to give a Gaussian profile

$$\rho_l \propto \exp\left[-\frac{1}{\gamma_l - 1}\left(\frac{x^2}{X_l^2} + \frac{y^2}{Y_l^2} + \frac{z^2}{Z_l^2}\right)\right]. \qquad (6.13)$$

Figure 18 shows the axial and radial intensity profiles of the emission of the low-molecular vapor plume and their

approximation by formula (6.13). The adiabatic index $\gamma_l$ is easily determined from the experimental diagram plotted in the coordinates: the logarithm of emission intensity as a function of the parameters $z^2$ and $r^2$. The corresponding analysis of measurement results reveals that $\gamma_l \approx 1.1$ at the initial stage of plume expansion. After that the adiabatic index increases with time to attain a value $\gamma_l \approx 1.2$ at the point in time $t = 20$ μs, testifying to the vapor cooling during the plume expansion. Notice that the isothermal solutions [117] are also described by the Gaussian profiles of the type of formula (6.13) when it is formally assumed that $\gamma_l = 3$ in this formula. For a vapor plume obtained by matrix evaporation, these isothermal profiles differ greatly from the experimental ones.

We now turn to the description of the expansion dynamics of heavy vapor. It can be inferred that the expansion is due to collisions with light molecules. (We are reminded that the number density of heavy molecules is very low and the effects stemming from collisions between the heavy molecules can be neglected.)

In the hydrodynamic approximation the expansion dynamics of the heavy vapor is described by the equations

$$\frac{\partial \rho_h}{\partial t} + \operatorname{div}(\rho_h \mathbf{u}) = 0, \qquad (6.14)$$

$$\frac{\partial \mathbf{u}}{\partial t} + (\mathbf{u}\nabla)\mathbf{u} = \beta(\mathbf{v} - \mathbf{u}), \qquad \beta = \frac{m}{M}v_c. \qquad (6.15)$$
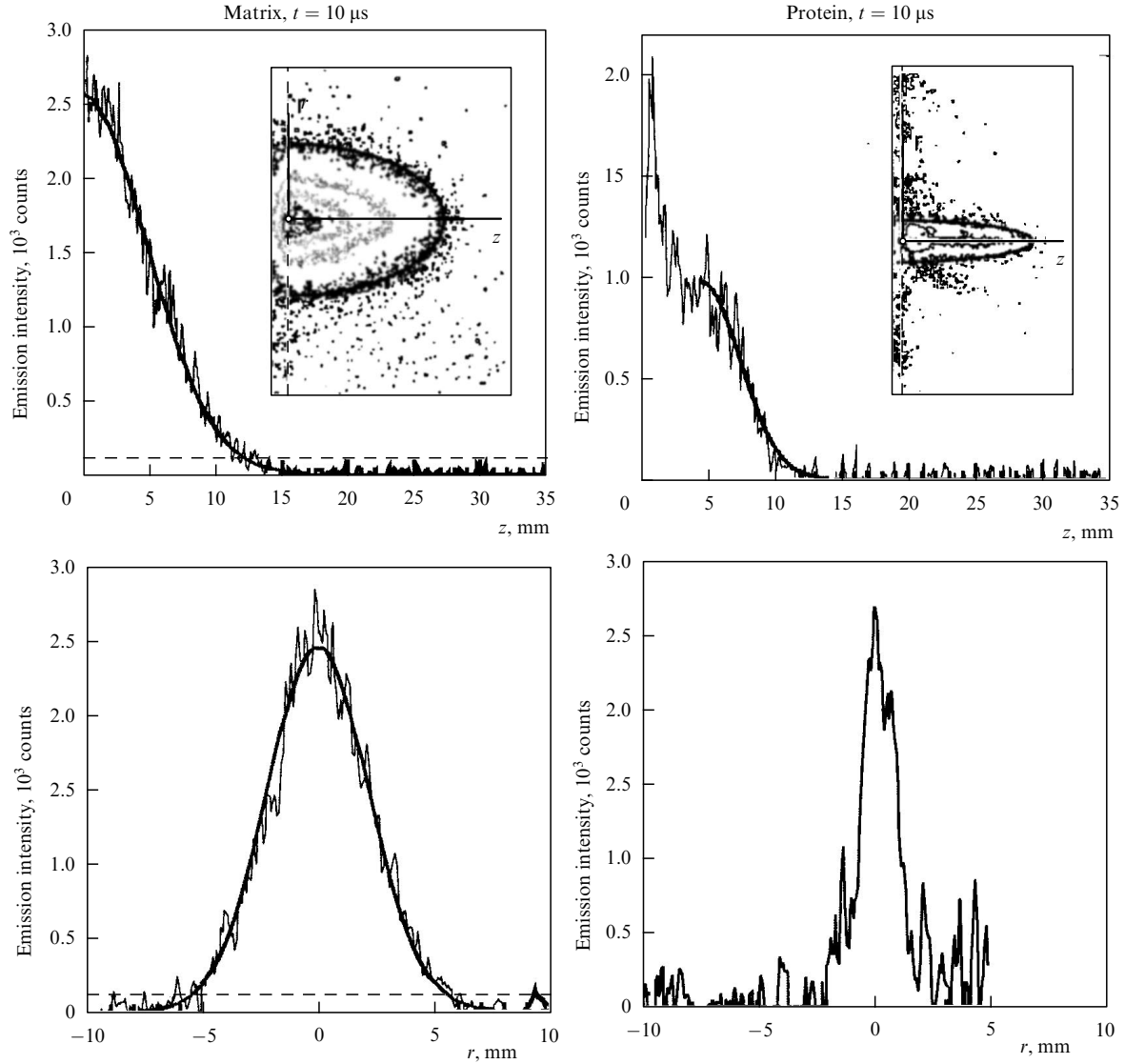
**Figure 18.** Density profiles of the matrix material and the protein in the radial ($r$) direction and normally ($z$) to the surface. The solid lines represent calculated data.

Here, **v** and **u** are the expansion velocities of light and heavy particles, respectively, the subscript 'h' designates the quantities relating to the vapor of heavy particles, $m$ and $M$ are the masses of light and heavy particles, and $v_c$ is the collision frequency. The main simplification of the model is that this quantity is assumed to be constant, so that $\beta = $ const.

We consider the special solution of the problem (6.14), (6.15) under the inference that the velocity distribution of the heavy molecules is a linear function of coordinates and their number density corresponds to a parabolic profile similar to that defined by expression (6.12). In this case, the problem (6.14), (6.15) transforms to a system of ordinary differential equations describing the motion of the boundaries of the heavy plume:

$$\ddot{X}_h = \beta\left(\frac{X_h}{X_l}\dot{X}_l - \dot{X}_h\right),$$

$$\ddot{Y}_h = \beta\left(\frac{Y_h}{Y_l}\dot{Y}_l - \dot{Y}_h\right), \qquad (6.16)$$

$$\ddot{Z}_h = \beta\left(\frac{Z_h}{Z_l}\dot{Z}_l - \dot{Z}_h\right).$$

The system of equations (6.16) is solved with the initial conditions similar to conditions (6.11). The parameters appearing in this system are also determined by means of a least square fit. From the fit it follows that the initial radius of the heavy plume (the protein) is somewhat smaller than the laser beam radius. An interpolation of the experimental data by Puretzky et al. [138] to the point in time $t = 0$ gives $X_{h0} = Y_{h0} = 0.1$ cm $= R_0/1.8$. To avoid the influence of the initial vapor asymmetry on the sharpening effect, we take $Z_{h0} = Z_{l0}/1.8$. In this case, the initial vapor asymmetry $z/r$ is similar for the light and heavy vapors. Two other parameters derived from the fit are $\beta \approx 3 \times 10^4$ s$^{-1}$ and $u_{z0} \approx 5.5 \times 10^4$ cm s$^{-1}$.

Referring to Fig. 17, for the above parameter values the model provides an adequate description of both the light and heavy plume expansion and a correct description of the dynamics of development of the asymmetry in expansion velocities. The time evolution of the relative dimensions $z/r$ of the light and heavy plumes is plotted in Fig. 17c. The experiment and the calculations suggest that the $z/r$ ratio for the light plume becomes practically constant for $t \geqslant 10$ μs, which is testimony to the inertial expansion. Meanwhile, the

expansion of the heavy plume is attended with a change in its asymmetry up to $t \approx 30 - 40 \, \mu s$. According to Eqns (6.16), this corresponds to the characteristic time (of the order of $1/\beta$) of the transient process.

The sharpening effect may be characterized by the parameter

$$\varkappa = \frac{Z_{h}/R_{h}}{Z_{l}/R_{l}}$$

which is the measure of relative 'elongation' of the heavy and light vapor forms. One can see from Figs 16 and 17d that the parameter $\varkappa$ increases during the transient period and then tends to saturate. The experimental dependences $r(t)$ and $z(t)$ in Figs 17a and 17b show that the initial radial expansion velocities of the heavy and light vapors are close to zero, while the normal velocities are nonzero. In this case, to within the experimental error $u_{z0} \approx v_{z0}$, i.e. the initial velocities do not depend on molecular mass. This is consistent with the measurements of Beavis and Chait [140] who found that the heavy molecules which spread during matrix vaporization possess velocities of the order of $10^5$ cm s$^{-1}$ irrespective of their mass.

From the physical standpoint, the result obtained in paper [140] implies that a hydrodynamic flow with a common mass velocity of the order of the velocity of sound sets in early in the expansion of a very dense vapor: $v_{z0} \approx c_{s} \approx 10^5$ cm s$^{-1}$. Such a flow may also originate through the effect of the solid matrix wall — 'the gun effect' [141, 142]. In this case, $v_{z0} \approx \sqrt{c_v \Delta T}$, where $\Delta T \approx 10^3$ K is a typical value of the initial vapor temperature in the laser evaporation from matrices. For typical values of the specific heat (heat capacity) approaching $c_v = 1$ J g$^{-1}$ K$^{-1}$, this leads to a characteristic velocity $v_{z0} \approx 10^5$ cm s$^{-1}$.

The sharpening effect is easily accounted for [138, 139]. As implied by the Euler equation, the driving force for the expansion of light vapor (the matrix) is the pressure gradient in the plume. The plume therefore accelerates more strongly in the $z$-direction which corresponds to the stronger gradient. The vapor density in it drops during expansion to make the molecular mean free path comparable with the plume dimensions, i.e. collisions cease to occur and the vapor expansion passes into the inertial mode [76]. The estimates submitted in papers [138, 139] show that the light vapor attains this mode in a time period of $t_f \sim 10 \, \mu s$. Thereafter the asymmetry $z/r$ of the light plume 'freezes', which is illustrated in Fig. 17c.

The velocity of motion of the heavy vapor changes due to collisions with the light one [the 'force of friction' entering Eqn (6.15) is proportional to the difference of mass velocities]. The collisions between light and heavy particles occur for a longer period of time than the collisions of light particles between themselves, which is due to the greater difference in collision cross sections: $\sigma_h/\sigma_l \approx (M/m)^{2/3}$. In the experimental conditions of Ref. [138] the corresponding cross sections differed by a factor of 40. That is why the change in symmetry of the heavy vapor takes place during a transient period $t_{tr} \sim 1/\beta$ which was approximately five times longer than the time $t_f$ in the context of experiments by Puretzky et al. [138]. The acceleration of the heavy plume diminishes as the overlap of the heavy and light vapors decreases. This is easily seen from Eqns (6.16), where the corresponding overlapping factors appear as multipliers of the velocity components of the light vapor. The effect of acceleration of the heavy vapor

terminates in a time period $t_{tr} \sim 1/\beta$. The attainable final velocities of the inertial heavy-vapor expansion depend both on the initial velocities and the initial plume geometry.

Simple estimates [138, 139] show that, in order for the sharpening effect to occur, two requirements should be fulfilled. First, $\beta t_f < 1$. Second, the initial 'velocity asymmetry' of the expansion (i.e. the ratio between the initial expansion velocities in the $z$- and $r$-directions) should exceed the initial 'geometric asymmetry' (i.e. the radial-to-axial dimension ratio for the initial plume). The second condition is easily satisfied in the laser evaporation of almost all multicomponent substances, whereas the first condition is safely fulfilled only when the heavy and light particles differ greatly in mass. That is why the sharpening effect is strongly pronounced when large biomolecules are evaporated from low-molecular matrices (the heavy vapor in the photographs given in Fig. 16 extends into a thin jet). Analogous, though less pronounced, stoichiometric changes are observed, for instance, in the deposition of high-temperature superconducting ceramics [112] (the sediment at the center is enriched with the heavier component).

## 6.4 Vapor condensation. Formation of nanoclusters

In conclusion we shall consider one more significant effect observed in the expansion of vapor produced by laser-driven material ablation. The case in point is the formation of nanoclusters in the plume of laser ablation products [143 – 158]. This is a readily controllable process which shows promise for many technological applications [151, 159]. We will enlarge on some of the physical properties of this process.

In essence we are dealing with the kinetics of rapid phase transitions of the first order — a problem which has not been adequately studied. A variety of features in the nanocluster production have yet to be elucidated, and several parameters important for understanding the physics of the phenomenon are hard to determine experimentally. Suffice it to say that typical cooling rates of the vapor in its expansion in the plume of laser ablation products amount to $10^{10} - 10^{11}$ K s$^{-1}$. The classical physics of phase transitions has never faced with so strongly nonequilibrium condensation conditions. That is why theoretical modeling remains an important source of information on a number of characteristics of this process.

The first theoretical analysis of condensation dynamics in a rapidly expanding vapor was performed by Yu P Raĭzer in 1960 [160]. He considered the self-consistent problem of vapor condensation during expansion, as applied to the problem of cosmic dust formation. A constituent of the analysis is the classical theory of nucleation, which was developed in Refs [161 – 164]. This theory of dynamic condensation of expanding vapor will be referred to as the Zel'dovich – Raĭzer (ZR) theory. This theory is outlined in detail elsewhere [76].

The ZR theory faces some problems when describing the characteristic condensation time scales, and in this connection it was subjected to criticism in Ref. [153]. Meanwhile, an advantage of the ZR theory is a clear revelation of the physics of the process, and it also accounts correctly for the characteristic scale dimension of the resultant clusters. Not denying the necessity of improving some of the details, we therefore treat the ZR theory as a good underlying model for the condensation. The ZR theory was applied to the nanocluster production in laser ablation in Refs [165 – 168]. Below we consider the basic results of these investigations.

From the theory of first-order phase transitions (see, for instance, Refs [164, 169–171]) it is known that the main driving parameter of condensation is the supercooling parameter

$$\theta = \frac{T_{eq} - T}{T_{eq}} \, , \qquad (6.17)$$

where $T$ is the vapor temperature, and $T_{eq}$ is the equilibrium temperature along the binodal. As the supercooling increases, the $\theta$ parameter approaches the critical value $\theta_c$ corresponding to the spinodal. In the classical nucleation theory the case is considered when the $\theta$ parameter is not very close to $\theta_c$. In this case, the condensation proceeds in two well-defined stages: (i) nucleation (the formation of a critical nucleus), and (ii) the growth of a supercritical nucleus. In the framework of the ZR theory these processes are described as follows.

Let there initially exist a plume of laser ablation products. In order not to overcomplicate the description we suggest that the plume is spherical and has density $\rho(r, t)$ and temperature $T(r, t)$ profiles corresponding to the isentropic model considered in Section 6.1. The plume will also be assumed to be a monoatomic gas, i.e. the adiabatic index $\gamma = 5/3$. In this case, one finds

$$\rho(r,t) = \rho_0 (1 - \xi^2)^{3/2} \Psi^{-3/2}(t), \qquad \rho_0 = \frac{8}{\pi^2} \frac{M}{R_0^3} \, , \quad (6.18)$$

$$T(r,t) = T_0 (1 - \xi^2) \Psi^{-1}(t), \qquad T_0 = \frac{16}{15} \frac{\mu}{R_g} \frac{E}{M} \, , \quad (6.19)$$

where $\xi = r/R(t)$ is the Lagrangian coordinate ($0 \leqslant \xi \leqslant 1$), $R_g$ is the molar gas constant, and $\mu$ is the atomic mass of the vapor.

The plume expansion obeys the law

$$\left( \frac{R}{R_0} \right)^2 \equiv \Psi(t) = 1 + 2 \frac{u_0}{R_0} t + \left[ \left( \frac{u_0}{R_0} \right)^2 + \frac{16}{3} \frac{E}{M R_0^2} \right] t^2 \, . \tag{6.20}$$

Here, $M$ is the total vapor mass, $E$ is the initial internal vapor energy, $R_0$ is the initial plume radius, and $u_0$ is the initial velocity of vapor expansion.

The main supposition required for the subsequent analysis is that the liquid droplets will be thought to be moving together with the vapor. In this case, the condensation may be treated independently for each particle with a fixed Lagrangian coordinate. According to the hypothesis of the ZR theory, for a small degree of condensation it is possible to neglect the effect of this process on the plume expansion. Then, for any coordinate $\xi$ the variation of specific vapor volume can be represented as

$$\frac{1}{V} \frac{dV}{dt} = \frac{3}{2} \frac{1}{\Psi} \frac{d\Psi}{dt} \, . \qquad (6.21)$$

Initially, the vapor expansion proceeds along the Poisson adiabat $pV^\gamma = \text{const}$. During expansion the vapor cools and comes into the saturation (the Poisson adiabat crosses the saturation adiabat defined by the Clausius–Clapeyron equation). The condensation sets in from this point in time. The corresponding temperature is defined as

$$T_c = q \Phi(a) \, ,$$

where $q$ is the heat of vaporization expressed in kelvins, and $\Phi(a)$ is the smaller root of the transcendental equation

$$\Phi^{-3} \exp\left( -\frac{1}{\Phi} \right) = a \equiv \frac{B}{V_0} \left( \frac{q^2}{T_s T_0} \right)^{3/2} \, , \qquad (6.22)$$

in which $T_s = 300$ K is the normalization temperature, $B = R_g T_s / \mu p_s$, and $p_s$ is the preexponential factor in the equation for the saturation vapor pressure. The values of $q$ and $p_s$ for different materials are compiled in handbooks (see lists of references in papers [32, 33]).

The point in time $t_c$ depends on the coordinate $\xi$; the saturation wave travels from the plume periphery to its center. The propagation of the front $r = r_c(t)$ of this wave obeys the equation

$$\frac{r_c}{R} = \sqrt{1 - \frac{T_c}{T_0} \Psi(t)} \, . \qquad (6.23)$$

The condensation comes to a halt due to the effect of 'quenching': particle collisions in a vapor expanding into vacuum terminate at some stage of the process (for more details, see Ref. [76]). Strictly speaking, the kinetic equation should underlie the consideration of the effect of quenching, but various estimates may also be obtained on the basis of the hydrodynamic description [44, 76, 160, 165]. These estimates agree to a numerical factor of the order of unity. For typical parameters of a plume produced in laser ablation, the quenching time is several microseconds long.

During condensation the latent heat of evaporation is released. The vapor temperature is therefore determined by the competition of two effects: the cooling related to the plume expansion, and the heating due to vapor condensation. Following Raĭzer [160], the corresponding equation can be written in the adiabatic approximation proceeding from the local energy balance in the two-phase vapor–liquid system. We now define the degree of vapor condensation $x$ as the ratio between the number of molecules in the liquid and the total number of molecules. Then, the adiabatic approximation leads to the equation

$$(1 + x) \frac{dT}{dt} + (1 - x) \frac{T}{\Psi} \frac{d\Psi}{dt} = \left( \frac{2}{3} q - T \right) \frac{dx}{dt} \, , \qquad (6.24)$$

$$T \bigg|_{t = t_c} = T_c \, .$$

The equation for the equilibrium temperature $T_{eq}(t)$ is also determined from the adiabatic approximation (for more details, see paper [165]). It is of the form

$$V_0 \Psi^{3/2} = \left[ 1 - \frac{2q}{2q - T_{eq}} \left( \frac{T_c - T_{eq}}{T_c} + 3 \frac{T_{eq}}{q} \ln \frac{T_{eq}}{T_c} \right) \right]$$

$$\times B \left( \frac{T_{eq}}{T_s} \right)^{3/2} \exp \frac{q}{T_{eq}} \, . \qquad (6.25)$$

In this case, the degree of equilibrium vapor condensation may be found from the equation

$$x_{eq} = \frac{2q}{2q - T} \left( \frac{T_c - T}{T_c} + 3 \frac{T}{q} \ln \frac{T}{T_c} \right) \, , \qquad (6.26)$$

where $x_{eq}(t) = x_{eq}\big(T = T_{eq}(t)\big)$. One can see from the last equation that in the case of unlimited vapor expansion under nearly equilibrium conditions (i.e. when the cooling is run

sufficiently slow) the vapor should completely condense: $x_{eq}\big|_{T\to 0} \to 1$. In the case of rapid expansion, complete condensation does not occur due to the quenching effect [160].

Let us hypothesize that the clusters for a given Lagrangian coordinate all have the same dimension, i.e. the coalescence [169] does not yet develop, and every cluster contains $g = g(t)$ atoms. Let $v = v(t)$ be the number of nuclei (per atom of the vapor). Then, the degree of vapor condensation is defined as $x(t) = v(t) g(t)$. Accordingly, for the vapor condensation rate we obtain the differential equation

$$\frac{dx}{dt} = g\frac{dv}{dt} + v\frac{dg}{dt}, \qquad x\big|_{t=t_c} = 0. \qquad (6.27)$$

The first term in the last equation describes the variation of the degree of vapor condensation due to the change in the number of nuclei, and the second one due to the variation of the cluster dimension. It now remains to write out the equations for the nucleation rate $dv/dt$ and the nucleus growth rate $dg/dt$. The first equation is determined from the quasi-stationary solution of the kinetic equation and is of the form [165]

$$\frac{dv}{dt} = k_{v0}(1-x)(1-\xi^2)^{3/2}\Psi^{-3/2}\exp\left(-\frac{T_v}{T}\frac{1}{\theta^2}\right), \quad (6.28)$$

$$v\big|_{t=t_c} = 0.$$

Notice that the preexponential factor in this equation is defined to a factor of the order of unity [164]. After Raĭzer we assume this factor to be equal to

$$k_{v0} = 4\frac{\rho_0}{\rho_1}\sqrt{\frac{2\sigma}{\pi m}}. \qquad (6.29)$$

We write the second term in Eqn (6.27) supposing that the nucleus growth proceeds in the kinetic regime, the accomodation coefficient is equal to unity, and the vapor and nucleus temperatures are the same. In this approximation, the corresponding equation governs the mass balance between deposited and vaporized atoms [165]:

$$\frac{dg}{dt} = k_g g^{2/3}\sqrt{T}(1-x)(1-\xi^2)^{3/2}\Psi^{-3/2}$$

$$\times\left\{1 - \exp\left[-\frac{q}{T}(\theta - \alpha g^{-1/3})\right]\right\}, \qquad g\big|_{t=t_c} = g_0. \quad (6.30)$$

Here, the notation was used

$$\alpha = \frac{2\sigma m}{k_B q\rho_1}\left(\frac{4\pi}{3}\frac{\rho_1}{m}\right)^{1/3}, \qquad k_g = \frac{\pi\rho_0}{m}\left(\frac{3}{4\pi}\frac{m}{\rho_1}\right)^{2/3}\sqrt{\frac{8k_B}{\pi m}}, \quad (6.31)$$

where $\sigma$ is the surface tension coefficient, $m$ is the mass of a single atom, and $\rho_1$ is the density of the condensed cluster substance.

The nucleation rate is an extremely sharp function of supercooling and is proportional to

$$\exp\left(-\frac{T_v}{T}\frac{1}{\theta^2}\right),$$

and therefore the critical nuclei are 'injected' into the saturated vapor at the instant of time the supercooling reaches its maximum. The corresponding instant of time $t = t_e$ can be determined from the equation [165]

$$\frac{1}{T_{eq}}\frac{dT_{eq}}{dt} = -\frac{1}{\Psi}\frac{d\Psi}{dt} + \left(\frac{2}{3}\frac{q}{T_p} - 1\right)\left(\frac{\alpha}{\theta_p}\right)^3\frac{dv}{dt}, \qquad (6.32)$$

where $T_{eq}$ is the equilibrium temperature, the parameter $\theta = \theta_p = 1 - T_p(t)/T_{eq}(t)$ and the nucleation rate $dv/dt$ are calculated along the Poisson adiabat $T = T_p$. The critical nucleus dimension in this case is $g_0 = g(t_e) = (\alpha/\theta_{max})^3$.

Notice that the condition $g \gg 1$ is necessary for the macroscopic description of nucleation. For typical parameters of a laser ablation plume (at the instant the laser pulse terminates we have $T_0 = 7000$ K and the specific volume $V_0 = 300$ cm$^3$ g$^{-1}$), the critical nucleus dimension $g_0$ for different substances was[5] 16 (Ge), 18 (Si), and 20 (C) atoms [166]. As the $T_0$ temperature increases, the critical nucleus dimension decreases. In paper [153], for instance, it was assumed that in silicon vapor $g_0 = 7$ atoms.

Therefore, it is valid to say that three characteristic waves propagate through the vapor (from the periphery to the center): the saturation wave, the wave of nucleus 'injection', and the quenching wave. The propagation of these waves was thoroughly considered in Refs [165, 166].

Having determined the point in time $t = t_e$, we conveniently redefine the remaining initial conditions for this point in time:

$$T\big|_{t=t_e} = T_p(t_e), \qquad g_0 = g(t_e) = g_{min},$$

$$v\big|_{t=t_e} = v_0 = \int_{t_c}^{t_e}\frac{dv}{dt}\bigg|_{T=T_p(t)}dt, \qquad x\big|_{t=t_e} = x_0 = g_0 v_0. \quad (6.33)$$

As a result, the vapor condensation problem reduces to a system of four ordinary differential equations for four unknown functions $T(t)$, $x(t)$, $v(t)$, and $g(t)$, with the initial conditions prescribed for the point in time $t = t_e$. This system was numerically integrated using the 'Mathematica' package [38]. Examples of such a solution covering the condensation of silicon and carbon vapors are given in Ref. [166].

A disadvantage of the above-outlined approach is the special parabolic form of the initial pressure and density profiles. In order to analyze arbitrary initial conditions or the condensation during the ablation in an ambient gas, one has to solve numerically the equations of gas dynamics. This problem was recently solved by Kuwata et al. [167], which made it possible to verify the solutions with parabolic initial density and pressure profiles, and also to investigate how the initial distributions affect the dimension distribution function of clusters being produced.

Different parameters which characterize the condensation dynamics in the expansion of substances into vacuum are given in Fig. 19 for rectangular initial pressure and density profiles. Referring to Fig. 19a, it is seen that initially the temperature $T(t)$ follows the Poisson adiabat, approaches the equilibrium temperature $T_{eq}$ at the cluster formation stage, and lastly departs from the equilibrium temperature due to the quenching effect late in the expansion. This behavior is typical for the ZR theory [76, 160].

---

[5] For silicon vapor it was supposed in the calculations [166, 168] that $T_0 = 8000$ K and $V_0 = 200$ cm$^3$ g$^{-1}$.
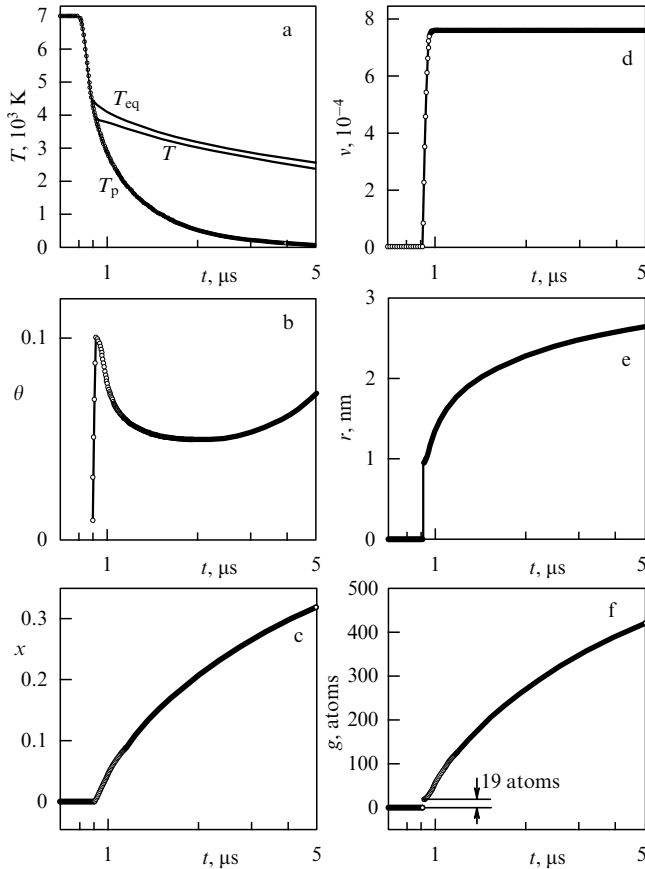
**Figure 19.** Dynamics of germanium vapor condensation, obtained through the numerical solution of the ZR model in combination with the numerical solution of gas dynamics equations [167]. See text for the explanations to the drawing.

The variation of the supercooling parameter $\theta(t)$ (Fig. 19b) also corresponds to the ZR theory. Initially, the supercooling increases to peak at the point in time $t = t_e$, then the supercooling decreases in response to nucleation and the temperature remains close to the equilibrium value for a long period of time. Finally, as the quenching stage is approached, the collision rate in the vapor lowers and the supercooling builds up.

The degree $x$ of condensation in the expanding vapor is lower than the equilibrium one (Fig. 19c). The number of clusters varies almost like a step function; the majority of clusters is produced about the point in time $t = t_e$ (Fig. 19d). The cluster growth takes place from the instant of critical nucleus creation to the instant of quenching. Under typical conditions of plume expansion into vacuum, the quenching sets in at the instant of time the cluster contains several hundred atoms. The dynamics of cluster growth is depicted in Figs 19e and 19f. All the results given in Fig. 19 pertain to the plume center ($\xi = 0$). The nucleation dynamics for any Lagrangian coordinate is calculated in a similar way.

With the knowledge of the $g(\xi)$ and $v(\xi)$ distributions, it is possible to find the cluster dimension distribution. The number of clusters produced over the interval $d\xi$ is

$$dN = 4\pi \frac{\rho_0 R_0^3}{m} (1 - \xi^2)^{3/2} v(\xi)\, \xi^2\, d\xi\,, \qquad (6.34)$$

and the cluster dimension variation is defined as

$$dr = \frac{dr}{d\xi}\, d\xi\,.$$

The distribution function sought is given by the formula

$$F(r) = -\frac{dN}{dr} = -\frac{32}{\pi} \frac{M}{m} \frac{v(\xi)\xi^2(1 - \xi^2)^{3/2}}{dr/d\xi}\,. \qquad (6.35)$$

Here $dr/d\xi < 0$, and therefore the function $F(r)$ is positive. The distribution function thus defined has a usual significance: $F(r)\, dr$ is the probability that a cluster will have dimensions in the range between $r$ and $r + dr$. Dividing $F(r)$ by the total number of clusters produced, it is possible to normalize the distribution function:

$$\int_0^\infty F(r)\, dr = N = \frac{32}{\pi} \frac{M}{m} \int_0^1 (1 - \xi^2)^{3/2}\, v(\xi)\, \xi^2\, d\xi\,. \qquad (6.36)$$

The dimension distribution function for silicon nanoclusters, determined experimentally by Marine et al. [151], is plotted in Fig. 20a. The results of the solution with parabolic initial distributions found in Ref. [166] for three materials are shown in Fig. 20b. For parabolic initial conditions, the resultant distribution functions take a characteristic triangular form. The typical dimension of the clusters produced is about 2 (Ge), 3 (Si), and 4 (C) nm. The characteristic width of the distribution [6] is $\Delta d_c \approx 0.6 - 0.8$ nm.

Figure 20c presents the solution of the corresponding problem for rectangular initial density and pressure profiles [167]. One can see from this figure that the distribution function for the resultant nanoclusters is significantly affected by the initial density and pressure distribution profiles in the plume of vaporized material. For rectangular distributions, the average cluster dimension and the distribution width are larger than for parabolic profiles.

Although the ZR theory does not contain adjustable parameters, the cluster dimensions arrived at are in good agreement with experimental data. No other *ab initio* models allowing a correct description of resultant nanocluster dimensions have come to our notice.

However the problem springs up with the time scale of the process. In Ref. [145], the time-resolved mass spectroscopy was employed to show that the smallest silicon clusters are produced over the $150 - 200$-ns range and contain $18 - 41$ atoms, i.e. they exceed the critical dimension (16 atoms for typical conditions of laser ablation), testifying to the onset of condensation. This was also confirmed by the fact that the clusters measuring about 1.5 nm were deposited on the surface due to laser ablation studied in Ref. [145], which is in reasonable agreement with the calculated data in Fig. 20: the clusters of critical dimension are produced somewhere after 53 ns.

---

[6] Note that the silicon cluster distribution with a sharp peak, given in Ref. [165], resulted from the insufficiently high accuracy of numerical calculations. Because of its moderate accuracy, the code found a parasitic root for one Lagrangian point, which corresponds to a lower dimension, in lieu of the true one. In the course of cubic interpolation of the function $r(\xi)$ point by point, a region originated with a low magnitude of $dr/d\xi$, which gave birth to the parasitic peak. The correct form of $f(r)$ for silicon clusters was found later in Ref. [166].
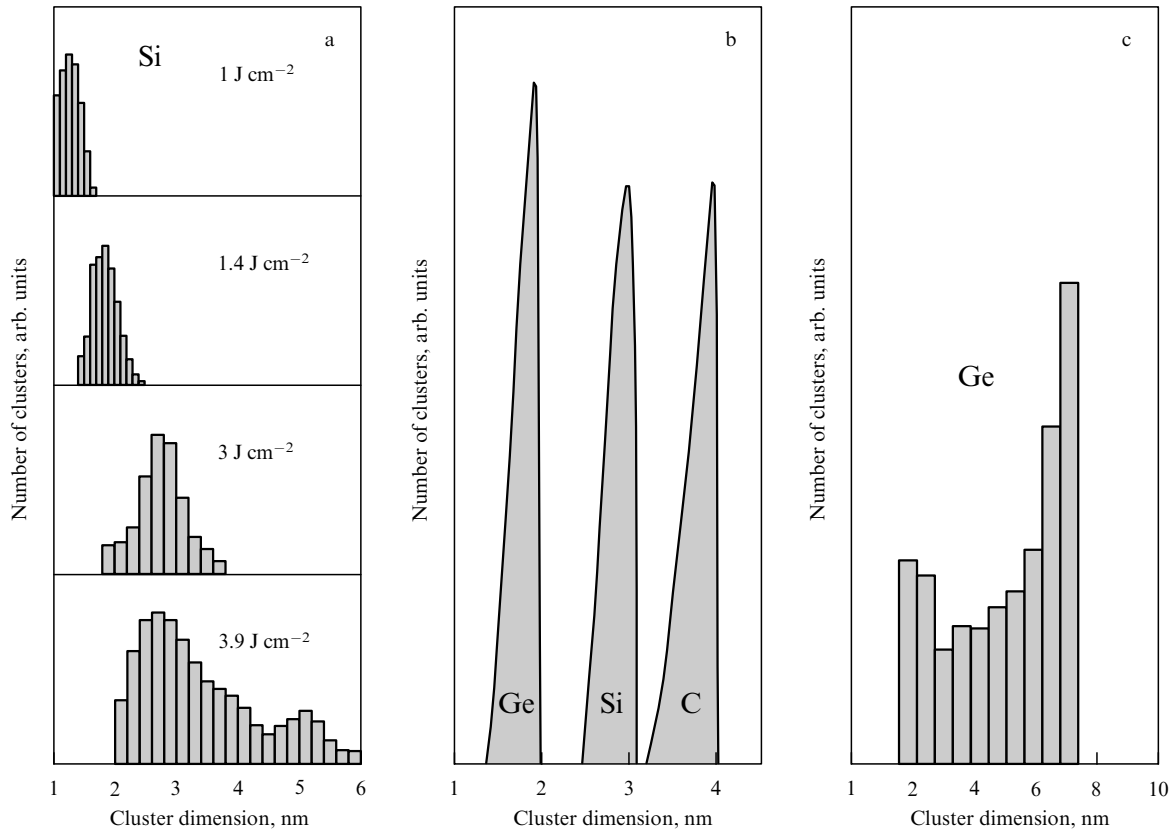
**Figure 20.** (a) Experimentally derived dimension distribution function for silicon nanoclusters in the ablation of silicon in an atmosphere of helium (4 Torr) for different pulse energy densities [151]. (b) Nanocluster dimension distribution function (expansion into vacuum) for three materials, which was derived through the numerical solution for parabolic initial density and pressure profiles [166]. (c) Dimension distribution function for germanium nanoclusters (expansion into vacuum), which was derived through the numerical solution for rectangular initial density and pressure profiles [167].

Meanwhile, the experimental investigation of cluster production dynamics employing time-resolved photoluminescence reveals that clusters are produced only after a long time delay. This latter depends on the pressure and the type of a buffer gas and amounts to $\Delta t \approx 200 - 400$ µs (ablation in an atmosphere of He at a pressure of 10 Torr) and $\Delta t \approx 3$ ms (Ar at a pressure of 1 Torr) [152]. These values are two-three orders of magnitude greater than the time found in Refs [165, 166].

The Rayleigh scattering technique gives similar values for cluster production times [152]. This situation is not quite trivial: the possibility of detecting a cluster by the Rayleigh scattering technique depends on the photodetector sensitivity. For a sensitivity level of the order of one scattered photon per cluster this dimension is about 2.0 nm [173, 174]. The time delay in the Rayleigh scattering may therefore be attributed to the detection ability of the technique.

In Refs [173, 174], the delay in the occurrence of the photoluminescence signal was ascribed to the time required for cluster cooling. The point is that the cluster temperature at the instant of 'quenching' is higher than the melting temperature, i.e. the clusters are liquid droplets. This statement is consistent with the experiment by Le et al. [175]. We are reminded that the melting temperature falls sharply with decreasing cluster dimension [176 – 178]. Meanwhile, an intense luminescence signal is observed from solid nanoclusters [179 – 181].

In the atmosphere of a buffer gas, the cluster cooling is related to the cooling rate of a 'fire ball' (as to the production

of a fire ball in laser ablation, see Ref. [182]). The corresponding cooling time of the clusters depends on their dimension and is defined by the formula [173, 174]

$$t_c(r_c) = \frac{1}{3} \frac{R_0^2}{\chi} \bar{p} \ln \frac{T_0}{T_\infty} \left\{ \Gamma \left[ -\frac{2}{3}, \bar{p} \ln \left( \frac{T_{m0}}{T_\infty} \left( 1 - \frac{r_v}{2r_c} \right) \right) \right] \right.$$

$$\left. - \Gamma \left[ -\frac{2}{3}, \bar{p} \ln \frac{T_0}{T_\infty} \right] \right\} . \tag{6.37}$$

Here, $R_0$ is the initial dimension of the fire ball, the parameter $\bar{p} = 1 + n$ characterizes the temperature dependence of the heat conduction coefficient:

$$\varkappa(T) = \varkappa_\infty \left( \frac{T}{T_\infty} \right)^n ,$$

$$\chi = \frac{\varkappa_\infty}{c_p \rho_\infty}$$

is the thermal diffusivity at room temperature, $T_0$ is the initial cluster temperature, $\Gamma(a, z)$ is the incomplete gamma-function:

$$\Gamma(a, z) = \int_z^\infty t^{a-1} \exp(-t) \, dt ,$$

and the parameters $T_{m0}$ and $r_v$ characterize the dependence of the melting temperature $T_m$ of the cluster on its

dimension [176]:

$$T_{\mathrm{m}} = T_{\mathrm{m0}}\left(1 - \frac{r_v}{2r_{\mathrm{c}}}\right). \qquad (6.38)$$

The time required for cluster cooling, found in Refs [173, 174], is in good agreement with the time of the onset of photoluminescence. One can therefore assume that clusters are produced early in the process (in a time of the order of several microseconds), but remain 'invisible' for a long time when observed by the Rayleigh scattering and photoluminescence techniques. In Ref. [158], an attempt was made to detect the 'invisible' clusters taking advantage of their decomposition by an additional laser pulse and the analysis of decomposed products by the laser-induced fluorescence technique. However, the cluster production time determined in this way turned out to be about the same as the time found in Ref. [152] previously. That is why the problem of correct determination of nucleation time scale calls for additional investigation. It is not improbable that nonisothermic nucleation effects manifest themselves in the case involved (i.e. one of the assumptions underlying the ZR theory is violated). As shown in Ref. [171], a delay occurs in the formation of a nucleus in the event of nonisothermic nucleation, when the gas and nucleus temperatures are different. In this case, the corresponding nucleus production time may rise by two-three orders of magnitude.

We also note that the production of nuclei in the expansion into vacuum is hard to study experimentally, because this requires vacuum chambers of relatively large size (theoretical estimates yield a value of the order of several meters). In vacuum chambers of a conventional size (tens of centimeters), attempts to observe the effects of nucleation in the expansion into vacuum do not meet with success. Several authors therefore believe that the clusters are not produced in the expansion into vacuum at all. This is not true: cosmic dust is produced in precisely matter expansion into vacuum (see references in paper [168]).

In the majority of experiments, ablation is effected in the atmosphere of an ambient buffer gas, which are rather hard to simulate. The expansion of material into an ambient gas is attended by many phenomena, such as the production of shock waves (external and internal), the development of Rayleigh – Taylor instabilities, resulting in the mixing of ablated material and the ambient gas, etc. In this case, one has to solve gas dynamics equations.

## 7. Conclusions

In the foregoing we considered several thermal and gas dynamics problems related to laser ablation. This review does not pretend to be exhaustive. As already noted, laser ablation has been the subject of several thousand publications, and it is unrealistic to cover all those works in a single review. In the selection of material our main concern was with the theoretical models that enable the derivation of quantitative results allowing a direct comparison with experiments.

Although laser ablation is an extremely intricate process, many aspects of this process are reasonably clear from the physical standpoint and allow a rather close quantitative description, which we endeavored to demonstrate in this review. As a rule, the models employed in the theory of laser ablation are reliant on complex nonlinear systems of partial differential equations whose solution calls for the use of numerical methods. This circumstance hampers the inter-

pretation of experimental results. Meanwhile, it is possible to obtain a reasonably complete description of laser ablation by invoking reduced models that involve the solution of systems of nonlinear ordinary differential equations. The reduction can be performed by taking advantage of the moments method or special solutions of the partial differential equations, the solutions possessing specific symmetry. These models prove to be expedient for the quantitative analysis of experimental results and allow a better understanding of the physics of the phenomenon.

While on the subject of laser ablation mechanisms, it is pertinent to note that some of them (the thermal model, the gas dynamics model, and the two-temperature model) have been solidly borne out in experiments. The possibility for the realization of other mechanisms, the photophysical one for instance, is still the subject of theoretical and experimental research.

Material ablation is attended by a wide variety of accompanying effects (vapor condensation, dispersion of the liquid phase, etc.) many of which are of technological interest (for example, thin film deposition, nanocluster production, etc.). The reduced models prove to be advantageous for the optimization of the corresponding technological processes.

Naturally, many phenomena are impossible to describe with recourse to simple dynamic models which reduce to ordinary differential equations. However, here too, the reduced models are beneficial, because they allow a clearer formulation of the physical problem.

## References

1. *Laser Ablation for Materials Synthesis* (MRS Symp. Proc., Vol. 191, Eds D C Paine, J C Bravman) (Pittsburgh, Pa.: Materials Res. Soc., 1990)
2. *Laser Ablation: Mechanisms and Applications* (Lecture Notes in Physics, Vol. 389, Eds J C Miller, R F Haglund, Jr.) (Berlin: Springer-Verlag, 1991)
3. *Laser Ablation of Electronic Materials: Basic Mechanisms and Applications* (Proc. European Materials Res., Vol. 4, Eds E Fogarassy, S Lazare) (Amsterdam: North-Holland, 1992)
4. *Laser Ablation: Principles and Applications* (Springer Series in Mater. Sci., Vol. 28, Ed. J C Miller) (Berlin: Springer-Verlag, 1994)
5. *Laser Ablation* (Proc. European Materials Res., Vol. 55, Eds E Fogarassy, D Geohegan, M Stuke) (Amsterdam: Elsevier, 1996)
6. *Laser Ablation: Proc. Fourth Intern. Conf. on Laser Ablation, COLA-IV* (Eds R Russo et al.) (Amsterdam: North-Holland, 1998)
7. *High-Power Laser Ablation* (Proc. SPIE, Vol. 3343, Ed. C R Phipps) (Bellingham, Wash.: SPIE, 1998); *High-Power Laser Ablation* (Proc. SPIE, Vol. 3885, Ed. C R Phipps) (Bellingham, Wash.: SPIE, 2000); *High-Power Laser Ablation* (Proc. SPIE, Vol. 4065, Ed. C R Phipps) (Bellingham, Wash.: SPIE, 2000); *High-Power Laser Ablation* (Proc. SPIE, Vol. 4760, Ed. C R Phipps) (Bellingham, Wash.: SPIE, 2002)
8. Srinivassan R, in Ref. [4] p. 107
9. *Sovetskiĭ Entsiklopedicheskiĭ Slovar'* (Soviet Encyclopedic Dictionary) (Ed. A M Prokhorov) (Moscow: Sov. Entsiklopediya, 1989)
10. Bäuerle D *Laser Processing and Chemistry* 3rd ed. (Berlin: Springer-Verlag, 2000)
11. Novozhilov V V *Dokl. Akad. Nauk SSSR* **270** 831 (1983)
12. Sobol E N *Phase Transformations and Ablation in Laser-Treated Solids* (New York: Wiley, 1995)

13. Bäuerle D et al., in Ref. [3] p. 39
14. Bäuerle D et al., in *Excimer Lasers* (NATO ASI Series, Ser. E, Vol. 265, Ed. L D Laude) (Dordrecht: Kluwer Academic Publ., 1994) p. 39
15. El'yashevich M A et al. "Razrushenie metallov pod deĭstviem izlucheniya opticheskogo kvantovogo generatora" (Breakdown of metals exposed to laser radiation) Report No. KÉ-14 (Minsk: Physics Institute, Belarussian SSR Academy of Sciences, 1963)
16. Anisimov S I et al. *Deĭstvie Izlucheniya Bol'shoĭ Moshchnosti na Metally* (Action of High-Power Radiation on Metals) (Eds A M Bonch-Bruevich, M A El'yashevich) (Moscow: Nauka, 1970); *Action of High-Power Radiation on Metals* (Springfield, V.A.: National Technical Information Service, 1971)
17. Ready J F *Effects of High-Power Laser Radiation* (New York: Academic Press, 1971)
18. Anisimov S I et al. *Zh. Tekh. Fiz.* **36** 1273 (1966)
19. Anisimov S I *Teplofiz. Vys. Temp.* **6** 110 (1968)
20. Lyubov B Ya, Sobol' E N, in *Deĭstvie Kontsentrirovannykh Potokov Energii na Materialy* (Action of Concentrated Energy Fluxes on Materials) (Ed. N N Rykalin) (Moscow: Nauka, 1985) p. 226
21. Lyubov B Ya, Sobol' E N *Inzh.-Fiz. Zh.* **45** 670 (1983) [*J. Eng. Phys. Thermophys.* **45** 670 (1983)]
22. Preuss S, Demchuk A, Stuke M *Appl. Phys. A* **61** 33 (1995)
23. Krueger J, Kautek W *Appl. Surf. Sci.* **96 – 98** 430 (1996)
24. Rosenfeld A, Campbell E E B *Appl. Surf. Sci.* **96 – 98** 439 (1996)
25. Cavalleri A et al. *Appl. Phys. Lett.* **72** 2385 (1998)
26. Haglund R F (Jr.), in *Laser Ablation and Desorption* (Experimental Methods in the Physical Sciences, Vol. 30, Eds J C Miller, R F Haglund (Jr.)) (San Diego: Academic Press, 1998) p. 15
27. Gray D E (Ed.) *American Institute of Physics Handbook* 3rd ed. (New York: McGraw-Hill, 1972)
28. Kuper S, Brannon J, Brannon K *Appl. Phys. A* **56** 43 (1993)
29. Luk'yanchuk B et al., in *Excimer Lasers* (NATO ASI Series, Ser. E, Vol. 265, Ed. L D Laude) (Dordrecht: Kluwer Academic Publ., 1994) p. 59
30. Arnold N, Luk'yanchuk B, Bityurin N *Appl. Surf. Sci.* **127 – 129** 184 (1998)
31. Brunco D P et al. *J. Appl. Phys.* **72** 4344 (1992)
32. Arnold N et al. *Laser Phys.* **8** 47 (1998)
33. Arnold N et al. *Proc. SPIE* **3343** 484 (1998)
34. Vorob'ev Yu V *Metod Momentov v Prikladnoĭ Matematike* (Moments Method in Applied Mathematics) (Moscow: Fizmatgiz, 1958) [Translated into English (New York: Gordon & Breach Sci. Publ., 1962)]
35. Samarskiĭ A A et al. *Rezhimy s Obostreniem v Zadachakh dlya Kvazilineĭnykh Parabolicheskikh Uravneniĭ* (Regimes with Sharpening in Problems for Quasilinear Parabolic Equations) (Moscow: Nauka, 1987) [Translated into English: *Blow-up in Quasilinear Parabolic Equations* (Berlin: De Guyter, 1995)]
36. Zwillinger D *Handbook of Differential Equations* (Boston: Academic Press, 1989)
37. Kirchhoff G *Vorlesungen über die Theorie der Wärme* (1949)
38. Wolfram S *The Mathematica Book* 4th ed. (Champaign, IL: Wolfram Media, 1999)
39. Goetz T, Stuke M *Appl. Phys. A* **64** 539 (1997)
40. Andronov A A, Vitt A A, Khaĭkin S E *Teoriya Kolebaniĭ* (Vibration Theory) 3rd ed. (Moscow: Nauka, 1981) [Translated into English: *Theory of Oscillators* (New York: Dover, 1987)]
41. Zel'dovich Ya B et al. *Matematicheskaya Teoriya Goreniya i Vzryva* (The Mathematical Theory of Combustion and Explosions) (Moscow: Nauka, 1980) [Translated into English (New York: Consultants Bureau, 1985)]
42. Barenblatt G I *Podobie, Avtomodel'nost', Promezhutochnaya Asimptotika* 2nd ed. (Similarity, Self-Similarity, Intermediate Asymptotics) (Leningrad: Gidrometeoizdat, 1982) [Translated into English: *Scaling, Self-Similarity, and Intermediate Asymptotics* (Cambridge: Cambridge Univ. Press, 1996)]
43. Frank-Kamenetskiĭ D A *Diffuziya i Teploperedacha v Khimicheskoĭ Kinetike* 2nd ed. (Diffusion and Heat Transfer in Chemical Kinetics) (Moscow: Nauka, 1967) [Translated into English (New York: Plenum Press, 1969)]
44. Anisimov S I, Khokhlov V A *Instabilities in Laser – Matter Interaction* (Boca Raton, Fla.: CRC Press, 1995)
45. Anisimov S I, Inogamov N A, Oparin A M *Izv. Ross. Akad. Nauk Ser. Mekh. Zhidk. Gazov* (6) 149 (1999); *Zh. Tekh. Fiz.* **36** 1273 (1966)
46. Anisimov S I, Kapeliovich B L, Perel'man T L *Zh. Eksp. Teor. Fiz.* **66** 776 (1974) [*Sov. Phys. JETP* **39** 375 (1974)]
47. Fujimoto J G et al. *Phys. Rev. Lett.* **53** 1837 (1984)
48. Wang X Y et al. *Phys. Rev. B* **50** 8016 (1994)
49. Sun C-K et al. *Phys. Rev. B* **50** 15337 (1994)
50. Groeneveld R H M, Sprik R, Lagendijk A *Phys. Rev. B* **51** 11433 (1995)
51. Hohlfeld J et al. *Appl. Phys. B* **64** 387 (1997)
52. Falkovsky L A, Mishchenko E G *Zh. Eksp. Teor. Fiz.* **115** 149 (1999) [*JETP* **88** 84 (1999)]
53. Anisimov S I, Rethfeld B *Izv. Ross. Akad. Nauk Ser. Fiz.* **61** 1642 (1997)
54. Gudde J et al. *Appl. Surf. Sci.* **127 – 129** 40 (1998)
55. Wellershoff S-S et al. *Appl. Phys. A* **69** (Suppl.) S99 (1999)
56. Luk'yanchuk B S, Anisimov S I, Lu Y F *Proc. SPIE* **4423** 141 (2001)
57. Rethfeld B et al. *Appl. Phys. A* **69** (Suppl.) S109 (1999)
58. Anisimov S I, Makshantsev B I, Barsukov A V *Opt. Acoust. Rev.* **1** 251 (1991)
59. Batanov V A et al. *Zh. Eksp. Teor. Fiz.* **63** 586 (1972) [*Sov. Phys. JETP* **36** 336 (1973)]
60. Anisimov S I, Gal'burt V A, Fisher V I *Pis'ma Zh. Tekh. Fiz.* **1** 321 (1975) [*Sov. Tech. Phys. Lett.* **1** 153 (1975)]
61. Kikoin I K, Senchenkov A P *Fiz. Met. Metalloved.* **24** 843 (1967)
62. Kikoin I K et al. *Zh. Eksp. Teor. Fiz.* **49** 129 (1965) [*Sov. Phys. JETP* **22** 90 (1966)]
63. Hensel F, Franck E U *Rev. Mod. Phys.* **40** 697 (1968)
64. Korshunov Yu S et al. *Teplofiz. Vys. Temp.* **8** 1288 (1970)
65. Alekseev V A et al. *Pis'ma Zh. Eksp. Teor. Fiz.* **12** 207 (1970) [*JETP Lett.* **12** 131 (1970)]
66. Franck E U, Hensel F *Phys. Rev.* **147** 109 (1966)
67. Alekseev V A, Andreev A A, Prokhorenko V Ya *Usp. Fiz. Nauk* **106** 393 (1972) [*Sov. Phys. Usp.* **15** 174 (1972)]
68. Al'tshuler L V *Usp. Fiz. Nauk* **85** 197 (1965) [*Sov. Phys. Usp.* **8** 52 (1965)]
69. Trunin R F (Ed.) *Svoĭstva Kondensirovannykh Veshchestv pri Vysokikh Davleniyakh i Temperaturakh* (Properties of Condensed Materials at High Pressures and Temperatures) (Sarov: VNIIÉF, 1992)
70. Shaner J W, Gathers G R, UCRL Report 79586 (Livermore, 1977)
71. Bushman A V, Lomonosov I V, Fortov V E *Uravneniya Sostoyaniya Metallov pri Vysokikh Plotnostyakh Energii* (Equations of State of Metals at High Energy Densities) (Chernogolovka, 1992)
72. Bennet B I et al., LANL Report LA-7130 (1978)
73. More R M et al. *Phys. Fluids* **31** 3059 (1988)
74. Bushman A V, Fortov V E *Usp. Fiz. Nauk* **140** 177 (1983) [*Sov. Phys. Usp.* **26** 465 (1983)]
75. Anisimov S I et al. *Zh. Tekh. Fiz.* **49** 512 (1979) [*Sov. Phys. Tech. Phys.* **24** 295 (1979)]
76. Zel'dovich Ya B, Raĭzer Yu P *Fizika Udarnykh Voln i Vysokotemperaturnykh Gidrodinamicheskikh Yavleniĭ* (Physics of Shock Waves and High-Temperature Hydrodynamic Phenomena) (Moscow: Nauka, 1966) [Translated into English (New York: Academic Press, 1966, 1967)]
77. Landau L D, Lifshitz E M *Statisticheskaya Fizika* Pt. 1 (Statistical Physics) (Moscow: Nauka, 1995) [Translated into English (Oxford: Pergamon Press, 1980)]
78. Fortov V E, Dremin A N, Leont'ev A A *Teplofiz. Vys. Temp.* **13** 1072 (1975)
79. Smirnov B M *Dokl. Akad. Nauk SSSR* **195** 75 (1970)
80. Varel H et al. *Appl. Phys. A* **65** 367 (1997)
81. Kautek W et al. "Bio-medical applications of sub-picosecond laser ablation", in *5th Intern. Conf. on Laser Ablation* (Book of Abstracts) (Goettingen, July 19 – 23, 1999) p. 63
82. Kaganov M I, Lifshitz I M, Tanatarov L V *Zh. Eksp. Teor. Fiz.* **31** 242 (1956) [*Sov. Phys. JETP* **4** 173 (1957)]
83. Anisimov S I, Benderskiĭ V A, Farkash D *Usp. Fiz. Nauk* **122** 185 (1977) [*Sov. Phys. Usp.* **20** 467 (1977)]
84. Kantorovich I I *Pis'ma Zh. Tekh. Fiz.* **3** 230 (1977)
85. Girardeau-Montaut J P, Girardeau-Montaut C *Phys. Rev. B* **51** 13560 (1995)
86. Agranat M B, Anisimov S I, Makshantsev B I *Fiz. Tverd. Tela* (Leningrad) **29** 3433 (1987)

87. Agranat M B, Anisimov S I, Makshantsev B I *Appl. Phys. B* **47** 289 (1988)
88. Agranat M B, Anisimov S I, Makshantsev B I *Appl. Phys. B* **55** 451 (1992)
89. Anisimov S I, Prokhorov A M, Fortov V E *Usp. Fiz. Nauk* **142** 395 (1984) [*Sov. Phys. Usp.* **27** 181 (1984)]
90. Von der Linde D, Sokolowski-Tinten K, Bialkowski J *Appl. Surf. Sci.* **109 – 110** 1 (1996)
91. Sokolowski-Tinten K et al. *Proc. SPIE* **3343** 46 (1998)
92. Sokolowski-Tinten K et al. *Phys. Rev. Lett.* **81** 224 (1998)
93. Inogamov N A et al. *Pis'ma Zh. Eksp. Teor. Fiz.* **69** 284 (1999) [*JETP Lett.* **69** 310 (1999)]
94. Inogamov N A, Anisimov S I, Rethfeld B *Zh. Eksp. Teor. Fiz.* **115** 2091 (1999) [*JETP* **88** 1143 (1999)]
95. Anisimov S I et al. *Appl. Phys. A* **69** 617 (1999)
96. Landau L D, Lifshitz E M *Gidrodinamika* (Fluid Mechanics) (Moscow: Nauka, 1988) [Translated into English (Oxford: Pergamon Press, 1987)]
97. Luk'yanchuk B et al. *Appl. Phys. A* **57** 367 (1993)
98. Luk'yanchuk B et al. *Appl. Phys. A* **57** 449 (1993)
99. Luk'yanchuk B et al. *Appl. Phys. A* **62** 397 (1996)
100. Luk'yanchuk B et al. *Nucl. Instrum. Methods Phys. Res. B* **122** 347 (1997)
101. Luk'yanchuk B et al. *Proc. SPIE* **3343** 58 (1998)
102. Plotnikov V G *Dokl. Akad. Nauk SSSR* **301** 376 (1988)
103. Frisoli J K, Hefetz Y, Deutsch T F *Appl. Phys. B* **52** 168 (1991)
104. Aksenov V P et al. *Proc. SPIE* **4423** 70 (2001)
105. Bityurin N et al. *Proc. SPIE* **2802** 103 (1996)
106. Luk'yanchuk B et al. *Appl. Surf. Sci.* **108** 120 (1996)
107. Himmelbauer M et al. *Proc. SPIE* **3093** 220 (1997)
108. Bityurin N et al. *Appl. Surf. Sci.* **127 – 129** 164 (1998)
109. Arnold N, Bityurin N *Appl. Phys. A* **68** 615 (1999)
110. Malyshev A Y, Bityurin N M *Proc. SPIE* **4423** 218 (2001)
111. Aksakhalyan A D et al. *Zh. Tekh. Fiz.* **58** 1885 (1988)
112. Venkatesan T et al. *Appl. Phys. Lett.* **52** 1193 (1998)
113. Afonso C N et al. *Appl. Sci.* **46** 249 (1990)
114. Kools J C S et al. *J. Appl. Phys.* **71** 4547 (1992)
115. Miotello A et al. *Appl. Phys. Lett.* **61** 2784 (1992)
116. Anisimov S I, Bäuerle D, Luk'yanchuk B S *Phys. Rev. B* **48** 12076 (1993)
117. Singh R K, Narayan J *Phys. Rev. B* **41** 8843 (1990)
118. Basov N G et al. *Zh. Eksp. Teor. Fiz.* **51** 969 (1966) [*Sov. Phys. JETP* **24** 614 (1967)]
119. Hansen T N, Schou J, Lunney J G *Appl. Phys. A* **69** S601 (1999)
120. Aksakhalyan A D et al., Preprint IPF AN SSSR (Gor'kiĭ: IPF AN SSSR, 1981)
121. Geohegan D B *Thin Solid Films* **220** 138 (1992)
122. Matzen M K, Morse R L *Phys. Fluids* **22** 654 (1979)
123. Ovsyannikov L V *Dokl. Akad. Nauk SSSR* **111** 47 (1956)
124. Sedov L I *Dokl. Akad. Nauk SSSR* **90** 735 (1953)
125. Dyson F J *J. Math. Mech.* **18** 91 (1968)
126. Dawson J M, Kaw P, Green B *Phys. Fluids* **12** 875 (1969)
127. Nemchinov I V *Prikl. Mat. Mekh.* **29** 134 (1965)
128. Anisimov S I, Lysikov Yu I *Prikl. Mat. Mekh.* **34** 926 (1970)
129. Anisimov S I, Luk'yanchuk B S, Luches A *Zh. Eksp. Teor. Fiz.* **108** 240 (1995) [*JETP* **81** 129 (1995)]
130. Bogoyavlenskiĭ O I *Metody Kachestvennoĭ Teorii Dinamicheskikh Sistem v Astrofizike i Gazovoĭ Dinamike* (Methods in the Qualitative Theory of Dynamical Systems in Astrophysics and Gas Dynamics) (Moscow: Nauka, 1980) Ch. 7 [Translated into English (Berlin: Springer-Verlag, 1985)]
131. Ovsyannikov L V *Lektsii po Osnovam Gazovoĭ Dinamiki* (Lectures on the Foundations of Gas Dynamics) (Moscow: Nauka, 1981)
132. Kelly R, Miotello A *Nucl. Instrum. Methods Phys. Res. B* **91** 82 (1994)
133. Tyunina M et al. *Appl. Surf. Sci.* **96 – 98** 831 (1996)
134. Karas M, Hillenkamp F *Anal. Chem.* **60** 2299 (1988)
135. Berkenkamp S, Kirpekar F, Hillenkamp F *Science* **281** 260 (1998)
136. Vertes A, Gijbels R, Adams F *Laser Ionization Mass Analysis* (New York: Wiley, 1993)
137. Fu D J et al. *Nature Biotechnol.* **16** 381 (1998)
138. Puretzky A A et al. *Phys. Rev. Lett.* **83** 444 (1999)
139. Luk'yanchuk B S et al. *Proc. SPIE* **4070** 166 (2000)
140. Beavis R C, Chait B T *Chem. Phys. Lett.* **181** 479 (1991)
141. Stanyukovich K P *Unsteady Motion of Continuous Media* (New York: Pergamon Press, 1960)
142. Branen B, Casey K G, Kelly R *Nucl. Instrum. Methods Phys. Res. B* **58** 463 (1991)
143. Werwa E et al. *Appl. Phys. Lett.* **64** 1821 (1994)
144. Marine W et al., in *Advanced Laser Processing of Materials*: *Fundamentals and Applications* (MRS Symp. Proc., Vol. 397, Eds R Singh et al.) (Pittsburgh, Pa.: Materials Res. Soc., 1996) p. 365
145. Movtchan A et al. *Appl. Surf. Sci.* **96 – 98** 251 (1996)
146. Yamada Y et al. *Jpn. J. Appl. Phys. Pt. 1* **35** 1361 (1996)
147. Makimura T, Kunii Y, Murakami K *Jpn. J. Appl. Phys. Pt. 1* **35** 4780 (1996)
148. Li S, Silvers S J, El-Shall M S *J. Phys. Chem. B* **101** 1794 (1996)
149. Serna R, Afonso C N *Appl. Phys. Lett.* **69** 1541 (1996)
150. Muramoto J et al. *Jpn. J. Appl. Phys. Pt. 2* **36** L563 (1997)
151. Marine W, Luk'yanchuk B, Sentis M *Le Vide Sci. Tech. Appl.* **288** 440 (1998)
152. Geohegan D B et al. *Appl. Phys. Lett.* **72** 2987 (1998); **73** 371 (1998)
153. Wood R F et al. *Appl. Surf. Sci.* **127 – 129** 151 (1998)
154. Muramoto J et al. *Appl. Surf. Sci.* **127 – 129** 373 (1998)
155. Yoshida T et al. *Appl. Phys. Lett.* **68** 4780 (1999)
156. Lowndress D H et al. *J. Mater. Res.* **14** 359 (1999)
157. Makimura T, Mizuta T, Murakami K *Appl. Phys. Lett.* **76** 1401 (2000)
158. Muramoto J et al. *Appl. Phys. Lett.* **77** 2334 (2000)
159. Marine W et al. *Appl. Surf. Sci.* **154 – 155** 345 (2000)
160. Raĭzer Yu P *Zh. Eksp. Teor. Fiz.* **37** 1741 (1959) [*Sov. Phys. JETP* **10** 1226 (1960)]
161. von Becker R, Döring W *Ann. Phys.* (Leipzig) **24** 719 (1935)
162. Kramers H A *Physica* **7** 284 (1940)
163. Zel'dovich Ya B *Zh. Eksp. Teor. Fiz.* **12** 525 (1942)
164. Frenkel' Ya I, in *Sobranie Izbrannykh Trudov* (Collection Works) Vol. 3 *Kineticheskaya Teoriya Zhidkosteĭ* (Kinetic Theory of Liquids) (Moscow-Leningrad: Izd. AN SSSR, 1959) [Translated into English: *Kinetic Theory of Liquids* (Oxford: Clarendon Press, 1946)]
165. Luk'yanchuk B, Marine W, Anisimov S I *Laser Phys.* **8** 291 (1998)
166. Luk'yanchuk B et al. *Proc. SPIE* **3618** 434 (1999)
167. Kuwata M, Luk'yanchuk B, Yabe T *Proc. SPIE* **4065** 441 (2000)
168. Luk'yanchuk B S et al. *Proc. SPIE* **4070** 154 (2000)
169. Lifshitz E M, Pitaevskiĭ L P *Fizicheskaya Kinetika* (Physical Kinetics) (Moscow: Nauka, 1979) [Translated into English (Oxford: Pergamon Press, 1981)]
170. Gunton J D, San Miguel M, Sahni P S, in *Phase Transitions and Critical Phenomena* Vol. 8 (Eds C Domb, J L Lebowitz) (New York: Academic Press, 1983) p. 267
171. Bashkirov A G *Nonequilibrium Statistical Mechanics of Heterogeneous Fluid Systems* (Boca Raton, FL: CRC Press, 1995)
172. *Fizicheskie Velichiny*. Spravochnik (Handbook of Physical Quantities) (Eds I S Grigoriev, E Z Meĭlikhov) (Moscow: Energoatomizdat, 1991) [Translated into English (Boca Raton: CRC Press, 1996)]
173. Luk'yanchuk B S, Marine W *Appl. Surf. Sci.* **154 – 155** 314 (2000)
174. Luk'yanchuk B S, Marine W *Proc. SPIE* **3885** 182 (2000)
175. Le H C et al. *Appl. Surf. Sci.* **96 – 98** 164 (1995)
176. Wautelet M *J. Phys. D* **24** 343 (1991)
177. Smirnov B M *Usp. Fiz. Nauk* **164** 1165 (1994) [*Phys. Usp.* **37** 1079 (1994)]
178. Goldstein A N *Appl. Phys. A* **62** 37 (1996)
179. Rosenbauer M et al. *Phys. Rev. B* **51** 10539 (1995)
180. Kanemitsu Y *Phys. Rep.* **263** 1 (1995)
181. Umezu I et al. *J. Appl. Phys.* **84** 6448 (1998)
182. Prokhorov A M et al. *Vzaimodeĭstvie Lazernogo Izlucheniya s Metallami* (Interaction of Laser Radiation with Metals) (Moscow: Nauka, 1988)
183. Afanas'ev Yu V, Krokhin O N *Zh. Eksp. Teor. Fiz.* **52** 966 (1967) [*Sov. Phys. JETP* **25** 639 (1967)]
184. Afanas'ev Yu V, Krokhin O N *Tr. Fiz. Inst. Akad. Nauk. SSSR* **52** 118 (1970)
185. Afanasiev Yu V et al. *J. Russ. Laser Res.* **21** 505 (2000)
186. Afanasiev Yu V et al. *J. Russ. Laser Res.* **20** 489 (1999)
187. Afanasiev Yu V et al. *J. Russ. Laser Res.* **20** 189 (1999)
188. Afanasiev Yu V et al. *J. Russ. Laser Res.* **20** 89 (1999)